Diss. ETH Nr. 16355

Experimental Investigation
of
Film Cooling Flow Structure

ABHANDLUNG
zur Erlangung des Titels

DOKTOR DER WISSENSCHAFTEN
der
EIDGENÖSSISCHEN TECHNISCHEN HOCHSCHULE ZÜRICH

vorgelegt von
STEFAN BERNSDORF

Dipl.-Ing. ETH, MSc UCT
geboren am 25.5.1972
in Erlangen, Deutschland

Angenommen auf Antrag von
Prof. Dr. R.S. Abhari, Referent
Prof. Dr. T. Roesgen, Korreferent
Dr. M.G. Rose, Korreferent

Zürich, 2005

Seite Leer /
Blank leaf

ACKNOWLEDGEMENTS

Human beings, who are almost unique in having the ability to learn from the experience of others, are also remarkable for their apparent disinclination to do so...

Douglas Adams: *Last Chance to See*

TABLE OF CONTENTS

ABSTRACT

This document reports on a new experimental facility, the data taken and the scientific findings obtained. The facility is a closed loop, flat plate wind tunnel simulating the film cooling row flow field on the pressure side of a turbine blade. Engine representative non-dimensionals are achieved, providing a faithful model at larger scale. Heating the free stream air and strongly cooling the coolant gives the required density ratio between coolant and free-stream. Injection of coolant is done both in a steady and a pulsating fashion, thus simulating unsteady potential flow interaction between coolant and main flow. The three dimensional velocities are recorded using non-intrusive PIV, seeding is provided for both air streams. Two different cylindrical hole geometries are studied, with different streamwise angles. The flow parameters are varied over a typical range to simulate pressure side film cooling.

It is found that a low amplitude pulsation of the injectant can be described as quasi steady with very good accuracy. The quasi steady postulate has limited validity for a high amplitude of pulsation due to periodic lift-off and re-attachment of the cooling jet. The complex behaviour of the boundary layer in the vicinity of the cooling hole is investigated and linked to the entrainment of low momentum fluid into the kidney vortex pair. It is shown that the incoming flat plate boundary layer is thinned by the entrainment of the coolant jets, which is expected to increase the mean heat transfer coefficient. The cooling concentration is introduced as a new parameter to describe the mixing between coolant and main flow with the potential to support the numerical prediction of the temperature field in a gas turbine. It is shown that the decay of the rate of mixing and the circulation are driven by flow phenomena of the same order of strength, implying a generally slow dissipation of the jet. The shear layers surrounding the jet dominate the decay of the rate of mixing while the decay of the circulation is dominated by the growth of the end wall boundary layer.

ZUSAMMENFASSUNG

Die vorliegende Arbeit berichtet über eine neue experimentelle Anlage, die gemessenen Daten und die wissenschaftlichen Erkenntnisse die hieraus gewonnen wurden. Der geschlossene Windkanal mit einer ebenen Messtrecke simuliert das Strömungsfeld von Filmkühlung auf der Druckseite einer Turbinenschaufel unter Einhaltung von Maschinen-repräsentativen Kennzahlen. Das Dichteverhältnis wird durch Heizen der Hauptströmung und starkes Kühlen der Sekundärströmung erreicht. Die Sekundärströmung kann sowohl stationär als auch pulsierend eingeblasen werden, was die Modellierung die instationären Potentialeffekte erlaubt. PIV wird zur räumlichen Geschwindigkeitsmessung verwendet, wobei beide Strömungen geseedet werden. Die Strömungszustände werden über einen typischen Bereich variiert.

Es wird gezeigt, dass die pulsierende Einblasung mit kleinen Amplituden mit hoher Genauigkeit als quasi-stationär beschrieben werden kann. Für große Amplituden ist das nur noch mit Einschränkung möglich, da es hier zu periodischen Ablösungen des Kühljets kommt. Das komplexe Verhalten der Grenzschicht in der Umgebung des Filmkühlungsloches wird in Verbindung mit der Einbringung von langsamer Strömung in die Jetmitte untersucht. Es wird gezeigt dass diese Einbringung mit der Verminderung der Grenzschichtdicke gekoppelt ist, was wahrscheinlich eine Erhöhung des Wärmeübergangskoeffizienten zur Folge hat. Der Parameter "Cooling Concentration" wird eingeführt um das Mischungsverhalten zu beschreiben. Dieser Parameter hat das Potential die numerische Modellierung des Temperaturfeldes in einer Gasturbine wesentlich zu unterstützen. Es wird außerdem gezeigt, dass die Abnahme der Mischungsstärke und der Wirbelstärke von Strömungsphänomen gleicher Grössenordnung geprägt sind. Diese impliziert, dass der Kühljet langsam vernichtet wird. Die Abnahme der Mischungsstärke ist von der Scherströmung zwischen Jet und Hauptströmung getrieben, während die die Abnahme der Wirbelstärke vom Wachstum der Wandgrenzschicht getrieben wird.

1. INTRODUCTION

1.1 Motivation

High-efficiency thermal power plants and aircraft jet engines attract considerable research interest. There are a couple of long term reasons for that interest, namely the increasing awareness of the green house effect and the looming shortage of fossil fuels. However, in the short term, there are good economic reasons to improve efficiency in both power plants and transportation. A significant selection would include the increasing prices of fuel, the strong competition of the airlines and the fact that both power generation and aircraft propulsion fuel costs are a major factor in running costs.

One of the most powerful means of achieving higher efficiency in gas turbines is by raising the turbine inlet temperature. The turbine blade and nozzle guide vane materials limit the temperature at the turbine inlet. A lot of effort has been put into the research of materials for turbine blades to allow higher temperatures, resulting in modern materials with thermal barrier coatings that can withstand temperatures in excess of 1150°C.

Active cooling of the exposed components is necessary to increase the temperature further. The most critical component is the turbine blades as they experience not only extreme temperatures but also substantial mechanical forces. Centrifugal forces in combination with various forces are induced by the flow and the rotating system. The latest sophisticated cooling schemes combine internal cooling of the blade with the so-called film cooling. A typical high pressure film cooled turbine blade is shown in Fig. 1.1. The cooling holes on the leading edge and on the pressure side are visible.
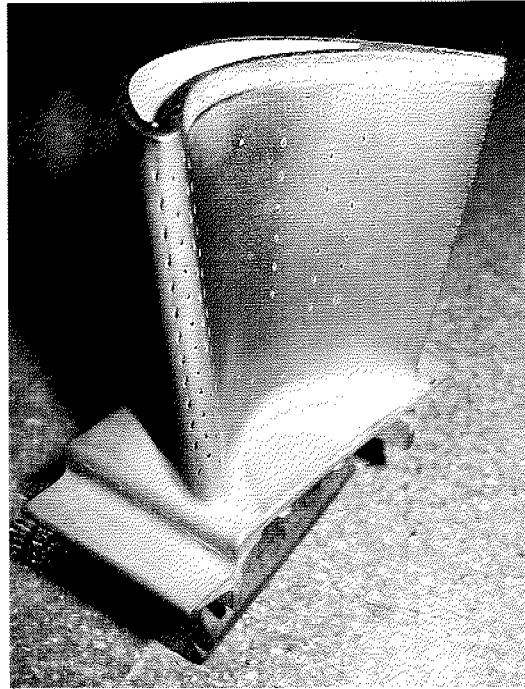
Figure 1.1: film cooled turbine blade

Here coolant air from the compressor is injected into the hot mainstream through discrete holes in the blades. Such cooling is adopted in the high heat flux region of the vane and blade where large thermal stress will be generated if only internal convective cooling is used. The principle of film cooling is sketched in Fig. 1.2. This inlet guide vane is supplied with cooling air from top and bottom. The air is first used internally for impingement cooling and then ejected through numerous cooling holes. Their number, shape and arrangement is subject of intensive development for each new blade, as the performance of the cooling strongly depends on them. Furthermore, the amount of cooling air used is of great importance. The amount of available compressed air in the engine cycle is reduced by bigger cooling amounts. Additionally, the cooling effect can be weakened by jets that emerge so fast from their holes that they penetrate the main flow and mix there.

This modern technology allows temperatures of up to 2000K at combustor exit and 1900K on the turbine blade. Film cooling generates significant amounts of loss, due to disturbed boundary layers and thermodynamic mixing. Better cooling will allow the use of less coolant and give higher efficiency.
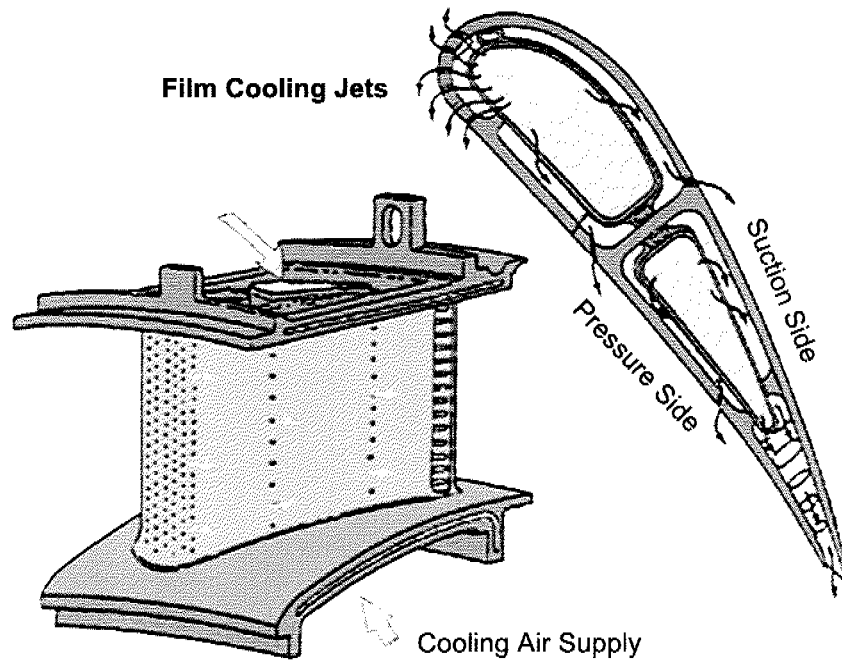
Figure 1.2: principle of film cooling

The main interest in the improvement of the film cooling, next to the reason of increase of efficiency, is the better prediction of the lifetime of a turbine blade. This results directly in a significant reduction of engine cost and is therefore a strong argument for the industry to engage in film cooling research.

1.2 Previous Research

The basic research in film cooling curiously started a long time before film cooling was actually applied or jet engines even were invented. Jet in crossflow as a basic fluid-dynamics problem attracted the interest of numerous researchers. The best known of them is probably Reynolds [94], who studied the behaviour of vortex rings in the late 1870s, a topic closely related to the modelling of jets in crossflow. Abramovich was one of the leading figures in this field in the beginning of the 1960s. His work is well documented in his "Theory of Turbulent Jets" [4].

The invention of film cooling is often attributed to K. Wieghardt [108] a German scientist who applied this technique to de-icing of aircraft wings by blowing

warm air over them. Research for film cooling of turbine components started in the late 1950s with the introduction of air-cooled turbines around 1960 [65]. Initially only internal cooling was applied. Film cooled blades were found in service from the late 60s, first in military engines and later also in commercial flight. Film cooling of stationary gas turbines was applied only much later.

Since the mid 1970s the number of publications related to film cooling grew enormously. It is hardly possibly to give a complete overview over all the innovative and challenging research that has been conducted since then. It also has to be considered that this field is of considerable interest for military application, resulting in often fragmented and delayed release of new insights to the public.

The field of film cooling research can be divided into two, the experimental work on the one side and the numerical simulation and modelling on the other. Extensive research and development has been conducted in modelling and simulation of film cooling. The literature regarding the modelling and simulation has been summarized by Kercher [64] and most recently by Burdet [19]. The following summary of the previous experimental research covers the key findings from the work related to flow structure, blowing and momentum flux ratio, density ratio, single hole geometry and shape, and the unsteady interaction between main flow and cooling jet.

It is notable that very little published data on detailed flow structure related to film cooling is available. The literature mainly focuses on film cooling effectiveness and heat transfer coefficient, mostly time averaged with very few exceptions.

• Flow Structure

A study of the fluid mechanics associated with a jet issuing into a main stream was made by Andreopoulus and Rodi [7]. Triple hot wire probes were used to measure all three velocity components. Once emerged, the jet was bent over abruptly by the cross stream and two longitudinal counter rotating vortices formed, causing the jet cross section to appear kidney shaped. The highest turbulence and shear stress levels occurred at locations from two to four diameters downstream of the hole, and were coincident with the maximum mean velocity gradients.

Pietrzyk et.al. [90] did velocity measurements with LDA in high density ratio film cooling environments. They showed that the largest region of high turbulence is coincident with shear layers on the windward side of the exiting jet and above the wake region that forms behind the jet.

4

• Influence of Blowing and Momentum Flux Ratios

Pederson et.al. [89] showed in a comprehensive study in the late 70s of film cooling wall effectiveness that the velocity ratio between jet and main flow is relevant to the film effectiveness achieved. As the velocity ratio increases the film cooling wall effectiveness increases to a maximum, then rapidly decreases. This maximum occurs around 0.5 and indicates that for higher values of the velocity ratio the jet separates from the wall, allowing the mainstream to flow underneath. The effectiveness is low directly downstream of the hole for conditions where the jet has separated from the wall. Later works discarded of the velocity ratio as descriptive parameter and used mainly blowing and momentum flux ratio.

Wilfert and Fottner [109] did measurements on the suction side in a turbine blade cascade. The state that at low blowing ratios a cooling jet behaves very much like a normal obstacle and the mixing mainly takes place in the boundary layer. With increasing blowing ratio the jet penetrates deeper into the mainflow. They detected not only the kidney vortex pair but also the individual horseshoe vortex around each jet and found that its position is strongly dependent on the blowing ratio and influences the aerodynamic mixing.

Yuen et.al. [111], [112] showed in their experiment with a single round hole on a flat plate that the highest film cooling effectiveness in the near hole region is achieved with a blowing ratio smaller than 0.5, whilst for regions downstream of the immediate region the maximum effectiveness at the blowing ratio of 0.5 and a momentum flux ratio of 0.3. This is attributed to the required additional momentum to transport the jet further downstream. They also demonstrated that the blowing ratio had little influence on the heat transfer except for the immediate and near field regions, where the heat transfer increased by about 25% as the blowing ratio was increased from 0.33 to 2.

• Influence of Density Ratio

Goldstein et.al. [44] did experiments on a flat plate with a single array of film cooling holes to investigate the effect of the density ratio. They state that the use of a relatively dense coolant, as is found in many applications, requires a significantly higher blowing ratio to cause jet separation from the surface than when the density ratio is at unity. Camci [20] did experiments on the suction side of a film cooled turbine blade in a short duration facility. He showed that an increase in density ratio while keeping the blowing ratio constant lowered the heat transfer coefficient. This effect was found to be more pronounced for high blowing ratios.

These findings suggest that the momentum flux ratio is a more appropriate parameter to describe film cooling than blowing ratio.

• Influence of Hole Geometry and Shape

Yuen et.al. [111], [112] performed measurements on a flat plate with various streamwise injection angles and blowing ratios. They concluded that a smaller injection angle results in a higher adiabatic film cooling effectiveness and an increase in heat transfer coefficient. The effect on both parameters however, was found to be moderate.

Gritsch et.al. [48],[49] studied detailed measurements of the flat plate film cooling effectiveness and heat transfer coefficients downstream of a single film cooling hole. They reported that compared to the cylindrical hole, the two types of expanded holes in their study (the fan shaped hole and the laid back fan shaped hole) show significantly improved thermal protection of the surface downstream of the injection, particularly at high blowing ratios.

Teng et.al. [105], [106] studied the effect of film hole shape on turbine blade film cooling performance under unsteady wake flow conditions. They used the same unsteady wake simulation facility as Du et.al. [26]. They found that both fan shaped and laid back fan shaped holes have much lower heat transfer coefficients right after the film hole exit when compared with cylindrical holes under the same conditions. In general fan shaped holes provide better film cooling effectiveness than laid back fan shaped holes and consequently much better film cooling effectiveness than cylindrical holes

• Influence of Potential Flow Interaction, Pulsation and Shock Waves

It is well known that downstream blades are affected by unsteady wakes shed by upstream vane trailing edges. Rigby et.al. [95] used a rotating wheel wake generator with cylindrical bars to model inlet guide vane wakes and shock waves under transonic flow conditions. The test blade was film cooled on both the suction and the pressure side. The main effect was a reduction in effectiveness caused by enhanced film mixing, and the shock passing effect was found to produce large fluctuations in the heat transfer rate.

Ou et.al. [88] and Mehendale et.al. [84] again used the rotating wheel wake generator to simulate the effect of unsteady wake on downstream stationary blade film cooling performance. Du et.al. [26] used a transient liquid crystal technique to measure the detailed heat transfer coefficients and film cooling effectiveness distributions on the same configuration. They concluded that heat transfer coefficients for a film cooled blade are much higher compared to a blade without film cooling. Unsteady wakes only slightly enhance heat transfer coefficients but significantly reduce film cooling effectiveness compared to a film cooled blade without unsteady wakes.

6

Several studies have investigated film cooling performance on a turbine blade in an actual rotating turbine environment. Dring et.al. [25] studied film cooling performance on a large scale model of a high pressure turbine first stage. The suction surface film effectiveness was found to correlate well with the flat plate data, while the pressure surface film effectiveness was significantly reduced. Takeishi et.al. [102] also measured film cooling effectiveness for a rotating blade with a realistic cooling geometry. The results of Dring [25] were corroborated, as the pressure surface film effectiveness was found to decrease relative to cascade tests due to the concave curvature and radial flow.

Abhari and Epstein [2] used a short duration turbine test facility to again study a film cooled rotating blade in a turbine stage environment. In these experiments, unsteady shock passing was present in addition to wake passing as unsteady effects. The suction surface showed a 12% decrease in heat transfer while the pressure surface had a 5% increase relative to cascade tests. The unsteady effects were attributed to coolant flow rate changes caused primarily by shock passing pressure fluctuations.

Abhari [1] showed that the unsteady stator-rotor interaction results in the pulsation of the coolant injection flow out of the film holes with large-scale fluctuations. He predicted time averaged magnitudes of unsteady surface heat flux on the pressure surface which are 230% greater than steady state predictions. This is attributed the combination of pulsating coolant flow and the interaction of the coolant with this unsteady external flow, which is shown to lower the local pressure side adiabatic film effectiveness by as much as 64% when compared to the steady case.

Bons et.el. [15] simulated the unsteady film cooling flow by sinusoidal pulsation of the injected coolant with a audio speaker. They measured velocity and temperature profiles as well as the adiabatic film effectiveness and the heat transfer. The observed effect of the coolant flow oscillation was to decrease effectiveness in the streamwise direction, while having little or no influence on effectiveness in the lateral direction. The rate of decrease of streamwise effectiveness is found to be a strong function of blowing rate, frequency and amplitude of the fluctuations.

Flow visualization results in the experiments of Ligrani et.al. [72], [73], [74] show two distinct coolant flow regimes: quasi steady and non-quasi steady. According to these authors, magnitudes of the coolant Strouhal number less than 1-2 correspond to quasi steady behaviour, and magnitudes greater than 1-2 correspond to non-quasi steady behaviour, regardless of the blowing ratio. Quasi steady film distributions are the same as the steady distribution which would exist at the same instantaneous flow condition. With the non-quasi steady film behaviour, mul-

tiple pulsations are imposed on the coolant over the time period required for it to pass through the film hole. As a result, portions of the film oscillate in ways different from adjacent portions, which gives a wavy appearance at each instant in time [72]. In many cases, non-quasi steady film distributions lead to more important alterations to film effectiveness values and flow structure than when quasi steady behaviour is present [73], [74].

1.3 Research Objectives

A new experimental facility has been constructed at ETH Zurich. The concept of the test rig here presented was to create a facility where steady and unsteady film cooling can be quantified regarding both the flow and thermal properties. This led to a continuously running closed-loop wind tunnel, as detailed flow measurements are not feasible in a transient facility. Measurement techniques decided on in the early concept phase were particle image velocimetry PIV for flow measurements and double sided thin film heat flux gauges for surface heat flux measurement. Probe measurements with fast and slow temperature and pressure sensors were another desired feature.

As designed, a large range of independent flow parameters can be adjusted in this unique facility. Geometrical, flow and thermal conditions all cover the typical conditions of a turbine pressure side to great extent. The exchangeable cooling hole geometry is scaled up, while relative dimensions like spacing and hole length are preserved. This work presents the results of 2 geometrical cases with a single array of 7 holes of constant diameter, length and spacing with a variation in the streamwise angle between 30° and 50°.

The governing flow conditions are Mach number M, density ratio DR, blowing ratio BR and momentum flux ratio IR and the reduced frequency f_r. Additionally, the momentum thickness θ has a significant influence on the film cooling behaviour. All parameters match real engine conditions.

In general, the test rig offers a number of new capabilities if compared to existing test facilities. The possibility of measuring detailed 3D flow structure in the near hole region of a film cooling hole in combination with pulsating coolant injection is unique. The detail and quality of the data obtained surpasses previously published data. Additionally, the capability of detecting the location and concentration of the cooling fluid is novel.

The research project conducted has a number of major goals. Initially, the need for high quality flow data to calibrate a novel film cooling model has to be satisfied. This model has recently been implemented into the LSM-internal flow solver MULTI3 [18], [19].

The objective to gain a better understanding of the physics of film cooling and the influence of the numerous flow parameters requires detailed analysis of the measured data. The dependency of the flow and vortical structure on blowing ratio, momentum flux ratio, streamwise injection angle and pulsating coolant injection must be investigated. The kind of unsteady interaction between cooling jet and main flow must be determined. The concentration of the cooling fluid in the flow domain must be quantified with a new approach of analysis. The observed flow phenomena must be linked to common knowledge of thermal effects of film cooling.

The potential benefits of this research are manifold. The conduction of basic experiments as this one results in an available database on the one side and in better understanding of the physics involved on the other side. The better understanding is the first step for the creation of new models that are implemented in CFD. These again can be validated with the measured data.

The physical insights gained also have the potential to support new creative design ideas in film cooling, which will eventually lead to better cooling designs. The innovation, implementation and improvement of models in CFD also will lead to better film cooling systems.

1.4 Thesis Outline

The introduction in Chapter 1 first addresses the motivation underlying this research project followed by an outline of the research objectives.

A major task of this project is the build up of the research facility. Chapter 2 starts with an overview about existing experimental film cooling research facilities to put the new test rig and its capabilities into context. The focus in the following sections is on the design, the engineering and the system integration of the closed loop flat plate wind tunnel. The instrumentation technique and the rig control units are summarized and the accuracy of the measured parameters is evaluated.

The velocity measurement system and its application is reported in Chapter 3.

The set-up of the system, the calibration, the data acquisition and data processing are explained and discussed. The measurement accuracy for the applied setting is specified.

The film cooling flow structure is assessed and reported in Chapter 4. The flow conditions present are defined and specified as well as the derivatives and jet trajectory. The pulsating injection of coolant is investigated regarding its behaviour in a quasi steady fashion. The focus shifts to the vortical structure in the next section, followed by an assessment of the entrainment of low momentum fluid into the core of the jet and the associated thinning of the boundary layer.

The spatially resolved concentration of coolant and the rate of mixing is investigated in Chapter 5. The conservation equation of the coolant concentration is utilized to discuss the relevant factors influencing the distribution of the diffusion coefficient.

This work is concluded in the last Chapter 6 with the key findings of this thesis. The contribution to the modelling of film cooling is pointed out. The knowledge gained regarding the near hole film cooling flow structure and mixing is summarized. The last section proposes future work.

2. Experimental Facility

2.1 Film Cooling Facilities Worldwide

An overview about the research facilities that contributed significantly to the film cooling literature is given in the following section. Emphasis is on unsteady film cooling facilities. They are briefly described together with their respective capabilities. An illustration of the major differences between facilities is given in Fig. 2.1 to condense the vast number of possibilities.
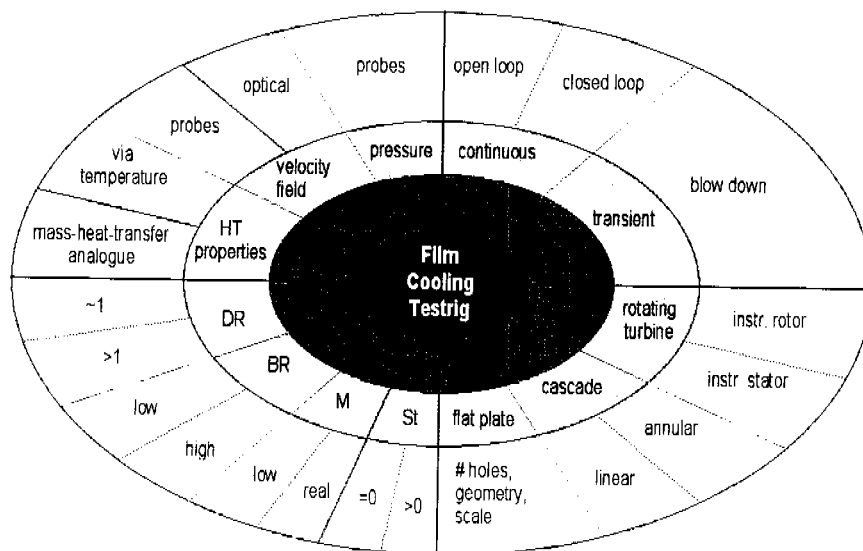

Figure 2.1: major aspects of existing film cooling test facilities

The figure above illustrates the four major factors driving the appearance, capability, shape and cost of a film cooling test rig.

There are two different types of wind tunnel, the continuously running and the blow down facility. The continuously running one requires relatively powerful engines to drive the main flow, while a blow down facility can do with smallish compressors and pumps. Adjustment of the different temperature levels in the blow down facility is relatively easy, but the transient temperature changes during the measurement phase have to be studied, quantified and accounted for. Setting of the temperature levels in a continuously running facility requires more sophisticated insulation, active continuous heating and cooling and respective control. In particular, solid body heat conduction has to be prevented. Two general set-ups of test rigs are used for film cooling research. The transient technique utilises a blow-down facility, as done by numerous investigators like Abhari, Abhari et al., Dunn, Eads, Giang, Guenette et al. and Teekaram et al. [1,2,3,28,31,41,50,103]. The obvious advantage for heat transfer measurements is the possibility to adjust temperatures of both solids and fluids without having to take serious measures to counter wall conduction errors in the short duration of measurement. Furthermore, surface heat flux measurements are tremendously facilitated, as a single time resolved temperature allows the assessment of the heat flux. Steady test facilities, as used by Goldstein et al., Ligrani et al., and Pietrzyk et al. [45,68,69,90], allow for longer measurement times, as is necessary for some measurement techniques involving lasers or a mass - heat transfer analogy.

There are three general types of test section. The most simplified version of reality is the flat plate. Here experiments are conducted with a single hole, single arrays of holes or multiple arrays of holes. Additional effects like acceleration, shock interaction, pulsating main- or coolant flow can be introduced. Closer to the real conditions are the experiments in a cascade of blades. Further distinction can be done between linear and annular cascades. Flat plate and cascades are used in combination with both, transient and continuous wind tunnels. Rotating test rigs, usually a scaled down single turbine stage, are generally operated in combination with a blow down facility. Different types of test sections are used. The geometrically simple form of a flat plate with one or more film holes often offers a sufficient approximation of the reality for many research interests (e.g. Cho et al. [23], Forth et al. [38], Giang [41]). Linear cascades of airfoils with film holes are utilized on a more complex level (e.g. Popp et al. [91], Smith et al. [100]) and also research with full-scale rotating rigs is conducted (e.g. Dunn [28], Dunn et al. [29]).

It soon became clear that the density ratio between main and coolant flow plays a significant role in film cooling. Different ways of modelling are used, namely cryogenic cooling in combination with air as coolant and the use of a foreign gas without the need of drastic cooling.

Steady flow regimes for both main and coolant flow are widely used to study film cooling. Giang [41] points out, that the efficiency of the cooling depends strongly on the mixing process between coolant flow and main flow, which in turn depends on other conditions. Studies have been done to investigate the possible factors that could influence the cooling performance. For instance, Goldstein et al. [44] investigated the geometrical effects of the cooling holes; Forth et al. [38] studied the effects of density and temperature ratios between the primary and secondary flows; Bons et al. [16] studied free-stream turbulence effects.

A wide variety of measurement techniques have been used in film cooling research. A general distinction has to be made between flow measurements and heat transfer measurements, as well as between steady and time resolved measurement capability.

Non-invasive techniques like PIV (e.g. Gogineni [42]) have become an attractive tool for flow measurements in recent years, as these techniques have become established and commercially available. The classic flow measurement methods utilizing pitot-static probes and hot wires (e.g. Rockwell [96]) have the advantage of simplicity, high accuracy and easily quantifiable errors. Therefore they are still widely used as supportive or sole flow measurement system. Non-quantitative techniques like shadowgraph (e.g. Smith et al. [100], Ligrani et al. [69]) or different types of flow visualisation are also utilized, as the flow field is next to heat transfer information often of secondary interest to the researchers.

Heat transfer measurements have been conducted with liquid crystals (e.g. Ekkad et al. [33], Honami et al. [58]) infrared cameras (e.g. Ligrani et al. [69]) and with thin film gauges (e.g. Abhari et al. [2,3], Dunn et al. [28,29], Epstein et al. [35], Guenette et al. [50]).

Liquid crystals give a reasonable time-resolution and information on the entire covered surface. Two of the bigger problems of this technique are that optical access is necessary, and that the sensitivity of the crystals only extents over a small temperature range. Utilisation of an infrared camera again requires optical access. Data of the entire surface can be measured at once. Calibration poses some difficulties here. Thin film gauges give highly time resolved data at discrete locations. No optical access is required, but the influence of the gauges on the heat flux, through creation of a thermal discontinuity, must be considered.

Naphthalene sublimation is used in mass transfer-analogues heat flux measurement (e.g. Cho et al. [23], Goldstein et al. [43]). Time averaged surface data of the convective component of the heat transfer is obtained without wall conduction and radiation errors. The drawback is the change of the surface shape over time, even though minute, and with that an influence on the mass transfer.

The following table lists the wind tunnels worldwide, that were used for contribution to film cooling research. It is meant to provide a comprehensive overview.

Table 2.1: film cooling facilities worldwide

Location	Ref.	Windtunnel	Test section	Flow	Meas. tech.
Gas Turbine Lab, OSU	[41]	blow down pulsating cooling iso-T surface	flat plate	M: <0.6 BR: 0.23-1 f: <480Hz	TFG - surface heat flux
Gas Turbine Lab, MIT Boston	[1], [2], [3], [35], [50]	blowdown foreign gas (Ar-Fr12) injection	scaled (ø 0.5m) single stage turbine	full scale engine properties	TFG - surface heat flux
LSM, ETH Zurich	[14]	closed loop, pulsating cooling, iso - T surface	flat plate	M: 0.1 - 0.64 DR: 1 - 1.8 BR: 0.5 - 3 IR: 0.1 - 5 f: 0 - 1kHz	PIV - flow field;
Naval Post-graduate school, Monterey	[68], [70], [76], [77], [78], [79], [80], [75]	open loop, pulsating main flow via shutter, constant heat flux surface	flat plate	Re: 1100-3700 BR: 0.5-1.3 DR: 1-1.5 f: 1-2Hz	hotwire probe,5-hole probe - flow; liquid crystals - surface heat flux,
Isentropic Light Piston Windtunnel, Oxford	[38], [103]	blow down, foreign gas (CO2) injection, iso -T surface	flat plate	M: 0.5 BR: 0.15-1 DR: 1-1.67	steady, TFG for surface heat flux
Cold Heat Transfer Tunnel CHTT, Oxford	[97], [98]	blow down foreign gas injection	annular cascade, 140% engine scale	engine repr. M	transient full surface liquid crystals
Calspan Buffalo, NY	[30], [28]	blow down	full scale single stage turbine	full scale, corrected speed	TFG - surface heat flux
Takasago Research & Development Center	[13]	open loop, foreign gas injection	linear cascade, scaled up	low speed ~40m/s	mass-heat transfer using CO_2 gas-chromatography

14

Table 2.1: film cooling facilities worldwide

Location	Ref.	Windtunnel	Test section	Flow	Meas. tech.
Takasago Research & Development Center	[13]	open loop, foreign gas injection	scaled down (ø~0.56m) single stage turbine	M: 0.6-1	mass-heat transfer using CO_2 gas-chromatography
HPHT, Karlsruhe	[69], [40]	open loop shock wave generator for main flow	flat plate	M: 0.8-1.12 DR: <1.6 BR: 0.5-2	IR-camera - surface heat flux, LDV - flow-field
Rotor Wake Heat Transfer Rig, NASA Lewis, Cleveland	[[54]	open loop, rotating pins to simulate wake	annular cascade	M: 0.27 BR: 0.5-1 Strouhal: 0.167-0.6	TFG - surface heat transfer
Virginia Tech, Blacksburg	[91], [100]	blow down, shock wave generator for main flow	linear cascade	T_m/T_c ~2 (varying) typical M	Kulites - surface static pressure, surface heat flux senors
Seoul National University	[32], [66], [62]	open loop with DS shutters to pulsate main flow	flat plate	U: ~10m/s BR: 0.5-2 ∂^*: 0.1D f: 0-36Hz	Liquid Chrystals - surface heat transfer
US Air Force Wright Laboratory, Dayton	[16]	open loop pulsation of coolant flow via speaker	flat plate	low speed u: 16m/s BR: 0.6-2 f: 0-20Hz	hot wire - flow, thermo-couple-T-field & surface heat flux
University of Texas, Austin	[90], [37]	closed loop low speed, turbulence generator	linear cascade	U: ~5.8-20m/s DR: 1.1-1.6 BR: 0.2-1.5 IR: 0.05-1.2 Tu: 0.5%-20%	IR - surface heat flux LDV - flow
Institut für Strahltriebwerke, UniBW München	[37], [40], [55], [17], [17]	continous high speed wind tunnel, iso-heat flux surface	linear cascade	M: 0.2-1.05 Tu: 0.-7.5% BR: 0.5-2.0	3D hot wire - flow, Liquid chrystals - surface heat flux

Table 2.1: film cooling facilities worldwide

Location	Ref.	Windtunnel	Test section	Flow	Meas. tech.
Heat Transfer Lab, University of Minnesota	[44], [45]	open loop, heated coolant, use of foreign gas	flat plate	U: 22-54m/s DR: 1-3.5 BR: 0.2-2.2 IR: 0.02-8 ∂^*: ~0.15d	Naphtalene Sublimation - adiabitic effectiveness, hot wire - flow
Ishikawa-jima-Harima Heavy Industries	[51]	open loop	flat plate	U: 22-54m/s DR: 1-2 BR: 0.5-2 IR: 0.02-8 δ^*: ~0.15d	thermocouples film cooling effectiveness
Imperial College, London	[111], [112]	open loop low speed, adiabatic / constant heat flux surface	flat plate	U: ~13m/s DR: ~1 BR: 0.3-2	Liquid Chrystals - surface heat transfer / effectiveness
VKI light piston tunnel, von Karman Institute	[81], [9]	blow down	flat plate, linear cascade	M: >0.6 BR: 0.5-4 Tu: 5.2%	TFG - surface heat flux

2.2 Facility Overview

The new film cooling test rig, as shown in Fig. 2.2, is based on a former supersonic calibration facility. It consists of a closed loop wind tunnel driving the main flow and a cooling injection from the in-house shop air system. The core part of the rig is the test section, where the injection and the measurements take place. The flow conditions are continuously monitored and recorded by a custom made data acquisition system. The rig is designed to be operated with different measurement techniques. At present a stereoscopic PIV system is implemented.

The rig's operating range is given in Table 2.2 together with the respective typical range in real pressure side film cooling.

Table 2.2: capabilities of new test facility

	pressure side film cooling	capabilities new test rig
density ratio DR	1.0 - 1.8	1.0 - 1.6
blowing ratio BR	0.8 - 4.0	0.5 - 3.0
momentum ratio IR	0.9 - 2.0	0.1 - 5.0
free stream Mach number M	0.3 - 0.8	0.1 - 0.6
reduced frequency f_r	1 - 3	DC - 2.5

test section

▶ main flow
▶ coolant flow
▷ shop air
▶ seeding flow
▷ boundary layer suction
■ heater, steam driven
▨ cooler, water driven
■ cryogenic cooler
▨ dryer
⌐¬ aerosol generator
◉ radial compressor
◎ pulsator
⊸Ⓜ electrical motor
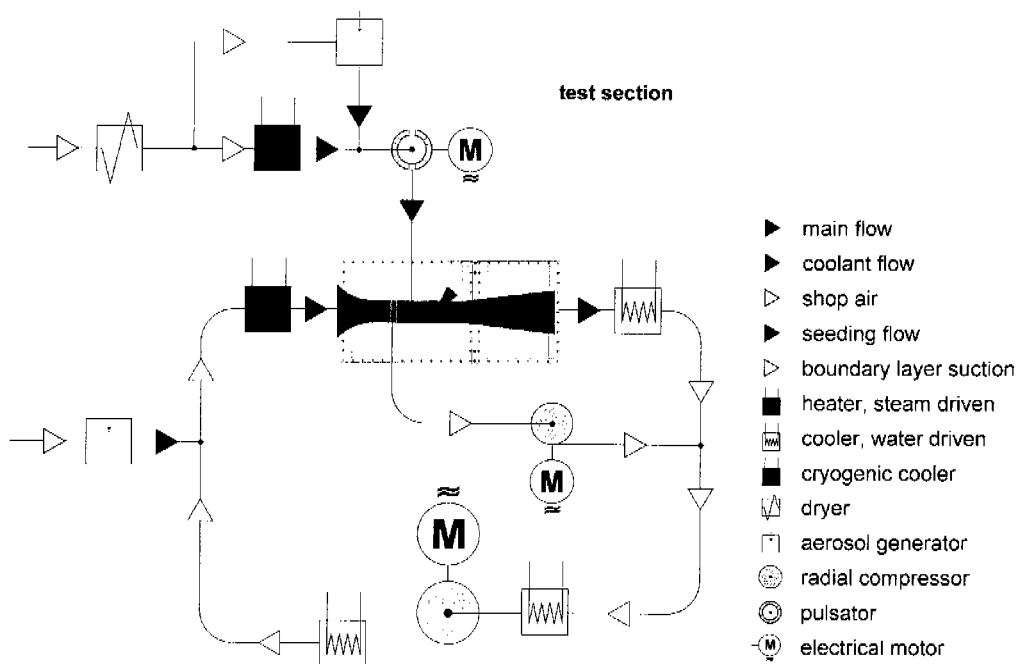
Figure 2.2: schematic of test rig

2.3 Main Flow

A centrifugal compressor with impeller diameter of 297mm, driven by a 470kW electrical motor, creates the main flow in the experimental closed loop facility, as shown in Fig. 2.2. The impeller is taken from an ABB VTC 254 turbo charger. The gearbox and periphery are custom made for the application. The pressure level in the system is self-adjusting by a small blow out valve. The resulting pressure in the test section is around the ambient pressure. Temperature is controlled with a water-

17

cooled heat exchanger downstream of the compressor, while a second cooler is installed just upstream of the impeller intake for its protection against overheating. That configuration allows a temperature range from 18°C to 40°C in the free stream.

The rotational speed of the impeller determines the pressure ratio and with that the resulting mass flow rate in the system. At its maximum speed of 30'000rpm the compressor can deliver up to 4kg/s. At present, the maximum mass-flow rate required is at about 1.5kg/s, for a free stream Mach number of $M=0.5$.

A steam-air heat exchanger is installed upstream of the test section to raise the main flow temperature up to 120°C, as illustrated in Fig. 2.2. This 180kW heat exchanger with an heat exchanger area of 84m^2 is fed by 7bar saturated steam from the house heating system. The heater is controlled with a feedback control loop. The heat is extracted from the main flow downstream of the test section by a water-cooled heat exchanger with an exchanger area of 142m^2. The pipe work containing the main flow is suspended from the ceiling to allow thermal expansion of the steel piping. Additionally, a compensator replaces a section of the pipe to allow angular and lateral displacement of the pipe without causing damage. The hot section of the test rig, between the steam heater and the water cooler, is wrapped in 30mm thermal insulation sheets and the test section is thermally decoupled from the environment by ceramic insulators.

The boundary layer thickness of the main flow is controlled by a suction arrangement (see Fig. 2.2 & Fig. 2.6). A centrifugal blower drives the boundary layer suction, extracting through 327 discrete holes of 1.2mm diameter stacked in 11 arrays over an area of 60x180mm^2. The extracted air is fed back into the loop far downstream of the cooler. The blower, a Meidinger Witt S-FVR4001, is driven by a 4kW electrical motor. The maximum capacity of the suction is about 50g/s and is adjusted with a hand valve.

Oil aerosol is blown from the seeding generator into the main flow upstream of the steam heater during PIV measurements. More information about the seeding generator is found in Chapter 3.3.1.2.

2.4 Cooling Flow

The secondary flow is delivered by the shop air system with a maximum of 75g/s. First a drier lowers the dew point of the air to −70°C. Two cylinders filled with water absorbing solid particles are alternately drying the air and recuperating inside that drier. Next in line is a fast acting self-controlling pressure control valve,

followed by a mass flow measurement section. Downstream is a single cycle cooler, capable of reducing the temperature down to –63°C at cooler exit. The 12m piping connecting the cooler and the primary wind tunnel is wrapped in 40mm insulation. A seeding generator containing 5 arrays of Laskin nozzles adds an oil aerosol 1.5m upstream of the injection location.

2.4.1 Cooling Plant

The cooling plant consists of 2 parts, namely the dryer and the cooler. The dryer is a heat-less regenerating adsorption dryer, Ultrapac MSD-300 manufactured by Deltatherm Hirmer GmbH. The drying of the air is done by the water molecules being physically bound to the large inner surface of the desiccant. The air is alternately dried in one of the two adsobers while the other one is being regenerated. This ensures continuous operation. Regeneration of the moisture laden desiccant is achieved with a partial flow of the dried air. This partial flow enters the adsorber and flows out into the atmosphere.

The cryogenic water cooled re-cooler, RKH DE-H1 manufactured by Deltatherm Hirmer GmbH, contains a cooling loop and closed cryogenic loop. The heat extracted from the air is dumped via the cryogenic loop into the cooling water. The liquid cryogenic medium is evaporated in the air-heat exchanger. Afterwards it is compressed and successively liquified in the water cooler. The medium is then fed back to the evaporator, thus closing the loop. The air temperature is controlled with a feed-back control loop that keeps the compressor running as long as the set temperature is not reached.

2.4.2 Pulsator

A constant low temperature air stream is converted into a pulsating flow with pressure fluctuations of up to 1000Hz. This type of device is not commercially available. Therefore, a pulsator was designed, manufactured and implemented in house [82]. The design is based on the experience made at the OSU with a similar project [41]. A cut through the final design is shown in Fig. 2.3.

Cold air is fed through two air inlets into a plenum between the rotor and the casing. The rotor has axial inlet holes and six slots on its circumference. The casing has one slot which serves as the air outlet. Six times per rotation of the rotor, the slots are aligned and air can exit. A flow straightener is placed in the exit plenum to achieve uniform flow through the different holes of the cooling hole array. The sensors monitoring the flow conditions are placed slightly further downstream in the plenum. They are described in detail in Chapter 2.6.
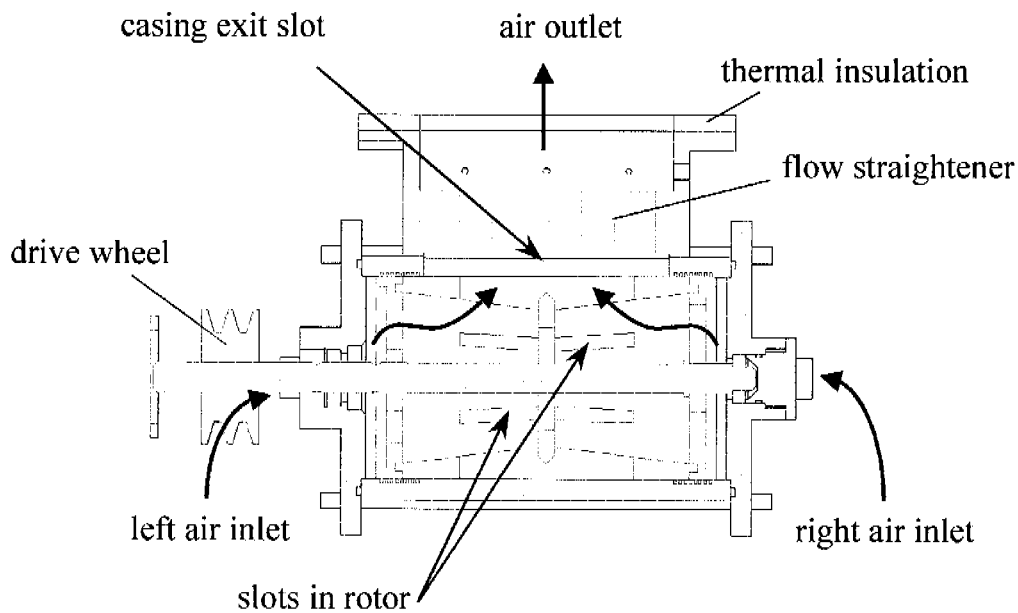
Figure 2.3: sketch of the pulsator

The rotor is supported by two ball bearings, one on each side of the rotor body. Three seals are used to suppress air leakage where the shaft penetrates the casing. The gap between the rotor and the casing is designed to be as small as possible. A gap of 0.05mm at ambient temperature is achieved. An increase of this radial clearance would reduce the strength of the air pulsation by leakage. A labyrinth seal is cut into the casing to further reduce leakage.

Thermal insulation is required as the air can reach temperatures as low as 220K. Therefore, the pulsator is mounted on a wooden plate, the connection to the test section contains a ceramic spacer, and the entire device is wrapped in a 30mm flexible insulator.

A 3kW electrical motor, manufactured by Danfoss, drives the pulsator via a V-belt. The motor speed is continuously variable, thus adjusting the pulsation frequency. The relative accuracy of adjusting the frequency with the speed-control is stated by the manufacturer as 2%.

The pulsator is equipped with a safety system that automatically cuts the power to the electrical motor when a predefined vibration level is exceeded. This is necessary, as the various Eigenmodes could not be predicted with sufficient accuracy.

The considerations leading to the final design require mentioning. The initial step in the design process of the pulsator is the analysis of the original design from

Ohio State University [41] and the improvement of its deficiencies. The research project at OSU was performed with a short time blow down facility. The test runs lasted for only a few seconds. The frequency of the pulsation was within a range of 100Hz to 500Hz. Considering the operational conditions at the continuously running ETH-test rig, transient heat transfer, thermal expansion and contraction and heating-up of the ball bearings are of higher importance.

The OSU pulsator features a straight cylinder with 6 slots on the circumference as rotor. After operation, the rotor and the casing showed tracks of abrasion that are associated with radial rotor deformation during high rotational speed. This was supported by the observation of scraping noises during operation. Furthermore, undesired leakage flow was observed with the rotor in closed position.

The next step is the design of a rotor with a quantified and minimal deflection. The inner contour of the rotor is thickened with a closed ring in the centre to take up the tangential stress. The material for the rotor is picked to be a low temperature high tensile aluminium alloy (7075/AlZnMgCu1.5), often used in aeroplane manufacturing.

Now a finite element analysis is performed with ANSYS to quantify the deflection. The result is illustrated in Fig. 2.4. A maximal deflection of 11.5μm at the maximum design speed is determined. This level of deflection ensures a safe operation at all rotational speeds, as is later confirmed during operation.
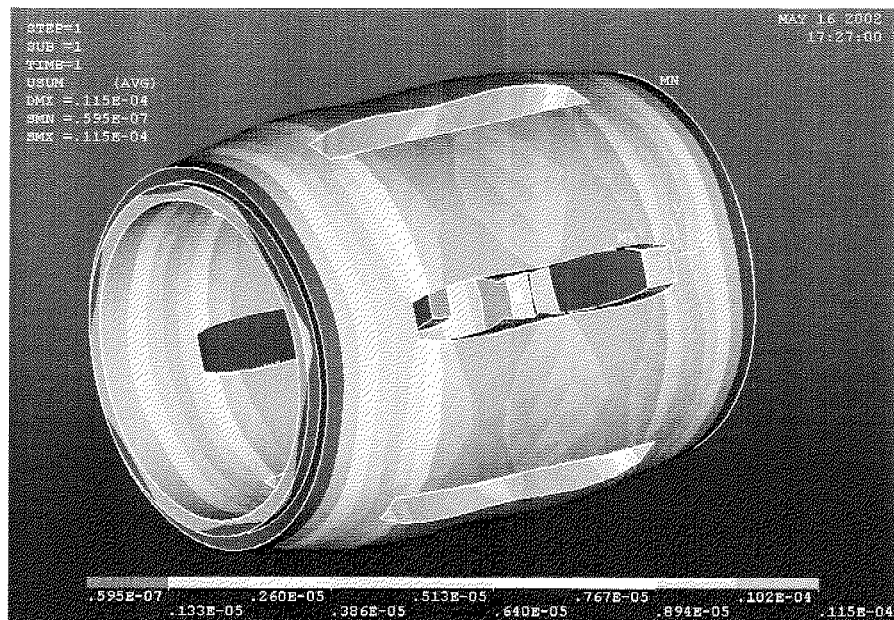
Figure 2.4: deflection of rotor at maximum design speed

The maximum von-Mieses stress is found to be on the outer side of the supporting ring (see Fig. 2.5). The level of 70.1N/mm² is an order of magnitude below the tensile strength of 570N/mm² of the material.
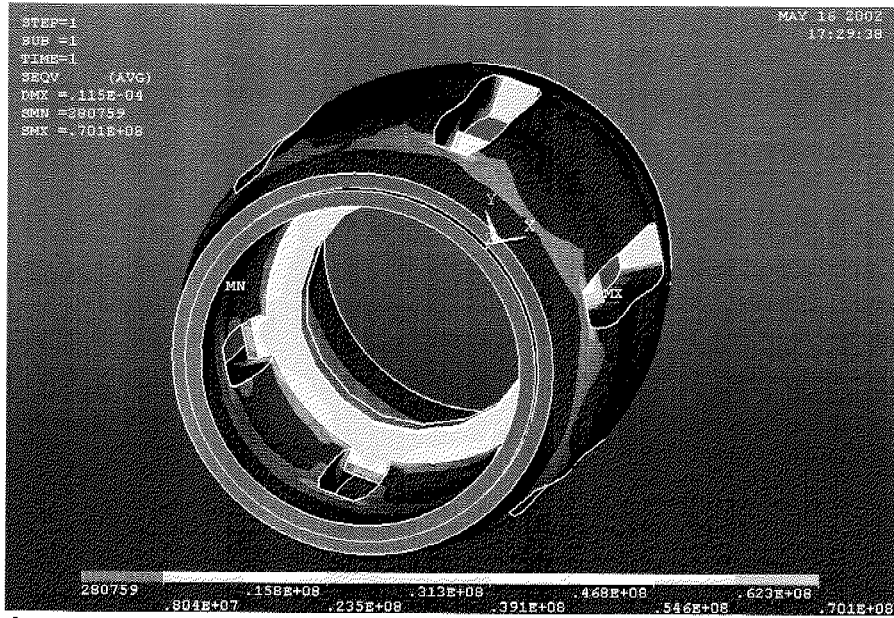
Figure 2.5: stress in rotor at maximum design speed

The analysis of eigen-frequencies of the rotor with the software DesignSpace showed two frequencies within the operating frequency range of the pulsator. The first eigenmode is a rotational mode between rotor body and shaft at 549Hz. However, the damping of the slightly elastic V-belt drive has not been considered in the analysis. No measures are taken prior the first test run, as the effect of the V-belt is expected to be positive.

The second eigen-frequency is a bending mode of the shaft at 845Hz. Again, no measures are taken prior to testing, as the drive belt with its radial force on the shaft is not taken into account in the analysis. This additional force is expected to raise the frequency.

Operation shows a couple of additional eigenmodes, where vibration levels exceed the set limit of the security system. The respective frequencies are dependent not only on the rotational speed but also on the mass flow rate of air and its temperature. However, with sufficiently fast acceleration of the pulsator all eigenmodes can be avoided.

2.5 Test Section

The core part of the experimental facility is the test section. A sketch is shown in Fig. 2.6. The test section is built up of a vertical frame of 40x80mm^2 steel bars that is closed with 25mm steel plates in front and back. The flow path inside the frame is constrained by aluminium and glass elements. A 3D nozzle accelerates the main flow coming from the settling chamber. The location of the boundary layer suction holes, just upstream of the cooling holes, is indicated in Fig. 2.6. Further downstream of the injection site is a 2D diffuser to recover some of the dynamic pressure. The cross-section at injection site is 40x181mm^2. The arc of main interest is the injection site of cooling flow in a range from 5 hole diameters d upstream to $35d$ downstream of the origin of coordinates (see Fig. 2.8).

(1) main flow   (4) 2D diffuser   (7) window for optical access off cameras

(2) boundary layer suction   (5) 3D nozzle

(3) film cooling holes   (8) window for light sheet access
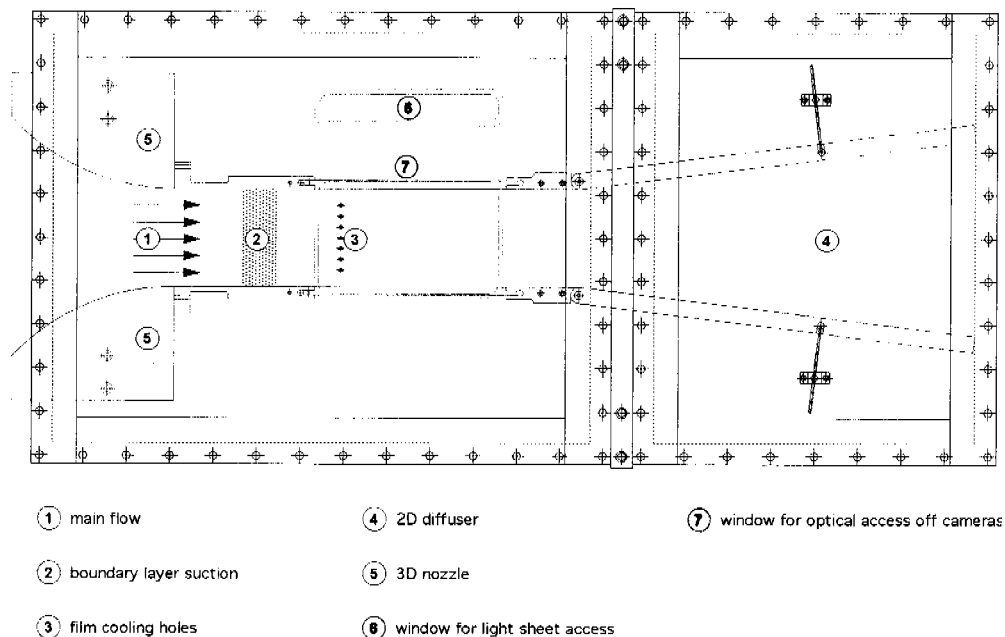
Figure 2.6: sketch of test section

Glass walls (15mm) on three sides provide optical access. The top and the bottom wall allow access of the light sheet. The laser sheet for PIV measurements is introduced to the system from the front, via the top window and a 45° mirror (see also Fig. 2.7). The front window allows the optical access of the two cameras.
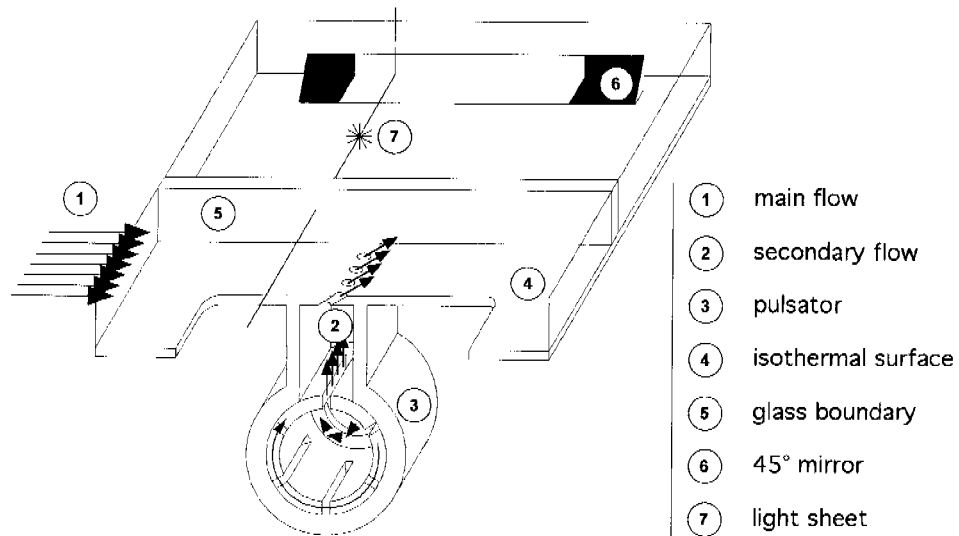
Figure 2.7: injection of cooling

(1)	main flow
(2)	secondary flow
(3)	pulsator
(4)	isothermal surface
(5)	glass boundary
(6)	45° mirror
(7)	light sheet

The figure above illustrates the connection between pulsator and test section, the injection of cooling into the main flow as well as the path of the light sheet inside the test section.

The definition of the coordinate system and of the relevant geometrical parameters is illustrated in Fig. 2.8.
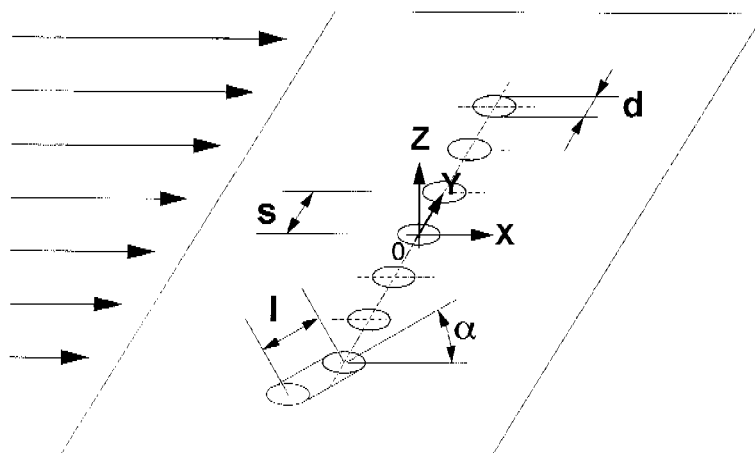
Figure 2.8: definition of coordinates and dimensions

The origin of the coordinate system, as used in all results presented, is in the centre

24

of the middle hole, irrespective of geometry. The two different geometries investigated are defined in Table 2.3.

Table 2.3: definition of geometry

geometry	d [mm]	# holes	s /d	l/d	α
1	5	7	4	2.8	30°
2	5	7	4	2.8	50°

2.6 System Behaviour

The relevant physical parameters of the wind tunnel have to be quantified. The tool applied to that task is extensive instrumentation in combination with an on-line monitoring system. Furthermore a couple of measurements are performed prior to the PIV measurements to complete the description of the flow conditions.

The system monitoring includes both the instrumentation of the test rig and the data acquisition and processing. A total number of 38 different parameters is measured to ensure knowledge and control over the flow conditions present in the test section. Their respective specification, purpose, location and accuracy is described in the following Section 2.6.1.

These monitored parameter are acquired with a PC. Some of them are shown on-line, together with the relevant derivatives, namely the main flow Mach number M, the blowing ratio BR, the density ratio DR, the momentum ratio IR and the reduced frequency f_r. This on-line system enables the fast and accurate adjustment of the desired conditions. The measured parameters as well as the most interesting derivatives are recorded in log files at regular 20s intervals. The respective system is introduced in detail in Section 2.6.2. Two sets of measurements are performed prior to the PIV measurement campaign as discussed in Section 2.6.2.6. For one, the time resolved pulsation of the cooling flow as a function of pulsation frequency and mean blowing ratio is quantified once, stored and correlated with the resulting flow filed at a later stage. Also, the main flow boundary layer is quantified with a 3 hole probe as a function of boundary layer suction setting and Mach number.

Section 2.6.3. gives an error analysis of the recorded data.

2.6.1 Instrumentation

There is a number of different measurement systems involved in the system monitoring of the facility.

The pressure is measured with a 16 channel differential pressure scanning mod-

ule PSI 9016. Flexible PVC tubes with an inner diameter of 1.5mm connect the pressure taps with the pressure scanning module. The measurement range of the channels differs according to the expected pressure range. Most channels are measured relative to atmospheric pressure. The channels are scanned simultaneously and the respective digital signals are transferred to the acquisition software via Ethernet. The location of the pressure taps is sketched in Fig. 2.9.

1	upstream orifice plate
2	downstream orifice plate
3	seeding injection
4	settling chamber
5	upstream BL-suction
6	upsteam cooling holes
7	downstream cooling holes
8	pressure loss cooler
9	plenum BL-suction
10	cooling before cooler
11	cooling after pulsator
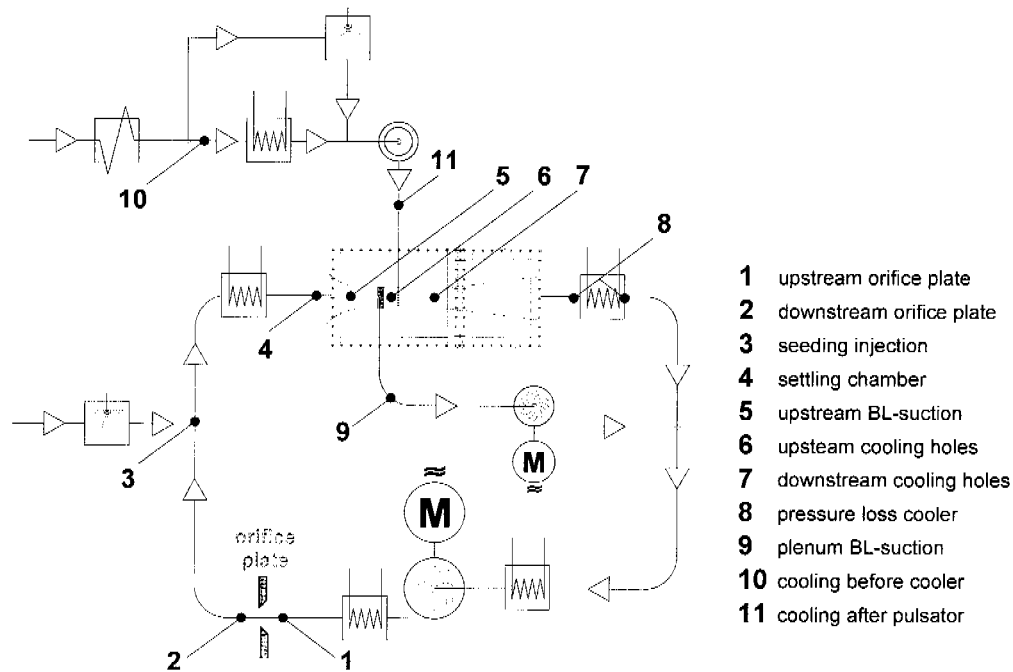
Figure 2.9: location of pressure taps

The pressure difference across the orifice plate is measured at the points 1 and 2. This information allows the derivation of the main flow mass flow rate, together with the respective temperature.

The pressure at point 3 gives the static pressure at the location of injection of main flow seeding. The pressure in the settling chamber (point 4) is averaged around the circumference of the tube with several taps, that are connected.

Points 5, 6 and 7 each have two pressure taps, both at the top and the bottom flow boundary. The two pressures are recorded separately to enable the detection of non-uniformities in the main flow. The respective pressure is averaged between the top and the bottom tap in the system monitoring software only. Point 5 is located upstream of the boundary layer suction, point 6 between boundary layer suction and cooling injection and point 7 is located at the downstream end of the test sec-

tion, upstream of the boundary layer suction.

Point 8 measures the differential pressure over the cooler inlet and outlet. This information helps detect blockage of the cooler to prevent breakage. The pressure in the plenum of the boundary layer suction is measured with tap 9. The pressure of the cooling flow upstream of the cryogenic cooler is measured at point 10 and the pressure in the plenum between pulsator and cooling holes is measured at location 11. The atmospheric pressure is continuously measured with a second pressure scanning module PSI-9016. This data is imported into the acquisition software via Ethernet.

The pressure sensitive modules are calibrated and sealed by the manufacturer PSI. The respective accuracies, summarized in the following Table 2.4 are stated by PSI as the accuracy relative to the full-scale output FSO. Pressure modules with different FSO are used.

Table 2.4: accuracy of pressure measurement points

point	FSO [psi]	FSO accuracy [%]	deviation [Pa]
1	15	±0.05	52.5
2	15	±0.05	52.5
3	15	±0.05	52.5
4	15	±0.05	52.5
5	5	±0.05	17.5
6	5	±0.05	17.5
7	5	±0.05	17.5
8	5	±0.05	17.5
9	5	±0.05	17.5
10	45	±0.05	157.5
11	45	±0.05	157.5
ambient	15	±0.05	52.5

The temperature is measured at several locations throughout the facility with resistance thermometers. Four thin film Pt100 thermometers are used in the test section to measure the temperature with little disturbance of the flow. They are manufactured by JUMO, type PF1.2150, with a design range from -80°C to 140°C. The sensors, that measure in the flow are Pt100 by RTK, type 1102-4 with a design range from -80°C to 400°C. The respective analogue signal is relayed to a 32 channel A/D data acquisition card in the PC via a system of external JUMO amplifiers. The location of the temperature sensors is sketched in Fig. 2.10.
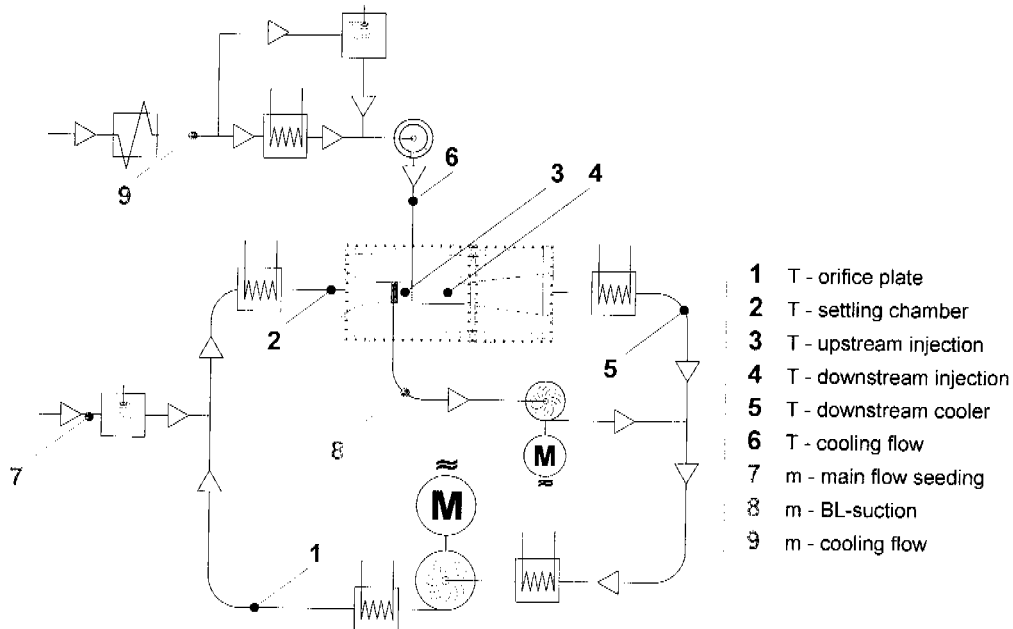
Figure 2.10: location of T- and m-sensors

1	T - orifice plate
2	T - settling chamber
3	T - upstream injection
4	T - downstream injection
5	T - downstream cooler
6	T - cooling flow
7	m - main flow seeding
8	m - BL-suction
9	m - cooling flow

The measurement chain from sensor to signal recorded in the PC is calibrated with a 2-point calibration at 0°C in ice water and an elevated temperature of 80°C that is measured with a reference mercury thermometer. The accuracy for the sensors is summarized in the following Table 2.5

Table 2.5: accuracy of temperature sensors

point	accuracy class	FS [K]	deviation [K]
1	B	310	0.5
2	B	400	0.9
3	A	400	0.4
4	A	400	0.4
5	B	310	0.5
6	A	300	0.25

The mass flow rate of the cooling, the main flow seeding and the boundary layer suction are each measured with a mass flow measurement device ECOFLOW, manufactured by Esters Electronik. The working principle utilizes the mass flow dependency of convective heat transfer. A Pt100 sensor is kept at a constant tem-

perature difference relative to the flow. A second sensor monitors the flow temperature. The electrical energy to maintain that temperature difference is therefore directly related to the mass flow rate.

Their respective location is shown in Fig. 2.10. The sensors are calibrated by the manufacturer. The stated accuracy of each device is given in the following Table 2.6. The analog signal is transmitted to the 32 channel A/D data acquisition card in the PC.

Table 2.6: accuracy of mass flow measurement devices

point	FSO [g/s]	FSO accuracy [%]	Deviation [g/s]
7	18	±2.5	0.45
8	72	±2.5	1.8
9	72	±2.5	1.8

The drive shaft of the pulsator features a pol-wheel with 6 slots. This allows the measurement of the rotational speed of the pulsator with an inductive trigger sensor. The trigger signal is converted to a frequency in the connected data transformer. The positive slope of the signal is triggering the PIV flow measurements as described in Chapter 3.8.

Additional data is acquired from the controller of the compressor. Static pressure and temperature are each acquired for the location at compressor entry, at compressor exit and after the cooler. Furthermore, the rotational speed of the compressor is recorded. This analogue data is also read into the PC via the 32 channel AD data acquisition card in the PC. The unknown accuracy of the 20 year old, undocumented measurement chain does not pose a problem, as this set of 7 parameters has the sole purpose of controlling the safe and repeatable operation of the compressor.

2.6.2 System Data Acquisition and Processing

The complex LabView code GEM_master handles the acquisition, processing, monitoring and storing of the 50 channels of slow system data. The raw signal is read in and processed with their respective calibration parameters. The calibration of a parameter i uses a standard linear method:

$$parameter_i = gain_i * signal_i - offset_i$$

Where the $signal_i$ is the raw data related to the $parameter_i$. The calibration constants $offset_i$ and $gain_i$ are determined with a 2 point calibration.

The flow condition in the test section is derived from those parameters. A complete description is achieved with the main flow Mach number M, the density ratio DR, the blowing ratio BR, the reduced frequency f_r, the momentum thickness θ, the shape factor H and the time resolved pressure pulsation in the plenum between pulsator and cooling holes. As mentioned in the previous section, the boundary layer and the pressure pulsation are quantified prior to the PIV measurements.

The geometrical reference location, where the above parameters are defined is the origin of the coordinate system, in the centre of the middle cooling hole. This definition is of importance for the values that have to be interpolated between upstream and downstream data.

2.6.2.1 Mach Number

The main flow Mach number is derived from the main flow mass flow rate $\dot{m}_m$ the main flow density ρ_m, the flow cross section A_m and the main flow total temperature T_t:

$$M = \frac{u_m}{a} = \frac{\dot{m}_m}{A \cdot \rho_m} \frac{1}{\sqrt{\kappa R T_{t,m}}}$$

It is important to note, that this Mach number is an average value over the entire cross section of the flow area. The flow cross section is known, κ and R are physical constants. The total temperature is assumed to be the measured temperature measured in the low velocity region in the settling chamber, downstream of the heater (see also Fig. 2.10). The density ρ_m is defined with the ideal gas law as:

$$\rho_m = \frac{p_m}{R T_m}$$

where the main flow static pressure p_m is interpolated between the pressure taps at location 6 and 7 at the up- and the downstream end of the test section (see Fig. 2.9) and the main flow temperature T_m is interpolated between the thin film sensors at location 3 and 4 (see Fig. 2.10).

The main flow mass flow rate at the reference location is the mass flow rate measured at the orifice plate plus the mass flow added with the main flow seeding minus the mass flow extracted with the boundary layer suction:

$$\dot{m}_m = \dot{m}_{orifice} + \dot{m}_{seed} - \dot{m}_{BL-suction}$$

The mass flow rate at the standardized orifice plate derives from the measured pressure difference over the orifice plate and the temperature. The static pressure drop across the orifice directly relates to the mass flow. The calculation procedure employed is according to the DIN Taschenbuch 229 [10].
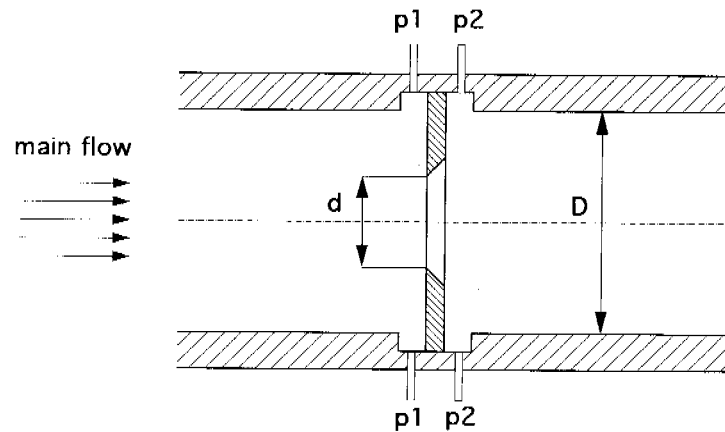
Figure 2.11: sketch of orifice plate

The orifice plate has an outer diameter of D=0.25m and an inner diameter of d=0.17m. The orifice is a standardised according to the norm EN ISO 5167-1: 1995. The static pressure is measured in the corner at 4 locations around the circumference each. The mass flow calculates as:

$$\dot{m} = c_d \cdot \varepsilon \cdot \frac{\pi}{4} d^2 \sqrt{2\rho \cdot \Delta p}$$

The expansion coefficient is defined as:

$$\varepsilon = 1 - \left(0.41 + 0.35 \cdot \beta^4\right) \cdot \frac{\Delta p}{\kappa \cdot p_1}$$

with the diameter ratio:

$$\beta = \frac{d}{D}$$

The discharge coefficient is defined by the Stolz equation as:

$$c_d = 0.5959 + 0.0312 \cdot \beta^{2.1} - 0.184 \cdot \beta^8 + 0.0029 \cdot \beta^{2.5} \left(\frac{10^6}{\mathrm{Re}_D}\right)^{0.75}$$

and the Reynolds number is here defined as:

$$\mathrm{Re}_D = \frac{u \cdot D}{\nu} = \frac{4\dot{m}}{\pi \cdot D \cdot \rho \cdot \nu}$$

An iterative calculation is necessary. A mass flow is assumed, inserted into the equation for the Reynolds number and the mass flow is calculated.

2.6.2.2 Density Ratio

The density ratio DR is defined with the density of the main flow ρ_m and the density of the cooling flow ρ_c as:

$$DR = \frac{\rho_c}{\rho_m}$$

The main flow density is defined in the previous section. The cooling flow density is defined by the same formula with the pressure being the main flow static pressure p_m. The static temperature is estimated iteratively. The measured temperature in the plenum between pulsator and cooling holes is assumed to be the total temperature, which is close to reality as the velocity is low. An initial mean coolant velocity is derived from the cooling mass flow rate $\dot{m}_c$ the cooling density ρ_c derived from the total temperature, and the total cooling hole cross section A_c as follows:

$$u_c = \frac{\dot{m}_c}{A_c \cdot \rho_c}$$

Then an approximate coolant static temperature in the jet is calculated by subtracting the kinetic energy $u_c^2/2c_p$ from the measured total temperature. This value is used to compute an amended coolant density. Now the coolant velocity is re-calculated. This process is converging within 3 to 5 steps to an accuracy 2 orders of magnitude better than the accuracy of the measured values.

2.6.2.3 Blowing Ratio

The blowing ratio BR is defined with the density of both the main and cooling flow ρ_m and ρ_c, and the velocities of both involved flows u_m and u_c as follows:

$$BR = \frac{u_c \rho_c}{u_m \rho_m}$$

Both involved densities are known from the previous sections, as is the coolant velocity. The main flow velocity is derived from the main mass flow rate, the flow cross section and the main flow density.

2.6.2.4 Momentum Ratio

The momentum ratio IR is defined with the density of both the main and cooling

flow ρ_m and ρ_c, and the velocities of both involved flows u_m and u_c as follows:

$$IR = \frac{u_c^2 \rho_c}{u_m^2 \rho_m}$$

The involved parameters are already known from the previous sections.

2.6.2.5 Reduced Frequency

The reduced frequency f_r is defined, similar to the Strouhal number St, with the pulsating frequency f, the distance from the beginning of the boundary layer to the centre of the hole L and the main flow velocity u_m as follows:

$$f_r = \frac{f \cdot L}{u_m}$$

The pulsation frequency is defined as the frequency displayed by the data transformer of the respective sensor. Its relative accuracy is stated by the manufacturer as 0.1%.

2.6.2.6 Boundary Layer

The main flow boundary layer is quantified prior to the PIV measurements intrusively with a pneumatic probe, which would prohibit the usage of laser light in the test section. The 3-hole cobra head probe is calibrated in a free jet facility. A set of non-dimensional calibration factors is derived from the flow data and the sensor signals:

$$K_\varphi = \frac{p_2 - p_3}{p_1 - \dfrac{p_2 + p_3}{2}}$$

$$K_t = \frac{p_o - p_1}{p_1 - \dfrac{p_2 + p_3}{2}}$$

$$K_s = \frac{p_o - p_s}{p_1 - \dfrac{p_2 + p_3}{2}}$$

and

$$\varphi = \sum_{i=0}^{n} k_{i\varphi} \cdot K_{\varphi}^{i}$$

$$K_{t} = \sum_{i=0}^{n} k_{it} \cdot \varphi^{i}$$

$$K_{s} = \sum_{i=0}^{n} k_{is} \cdot \varphi^{i}$$

with p_1, p_2 and p_3 being the pressure data from the centre and the two side holes of the probe; p_o being the calibration total pressure; p_s being the calibration static pressure; the polynomial order $n=8$; the polynomial coefficients k_{ij}, k_{it} and k_{is} determined with a least square approximation. The Mach number is derived from static and total pressure:

$$M = \sqrt{\frac{2}{\kappa - 1}\left(\left(\frac{p_t}{p_s}\right)^{\frac{\kappa-1}{\kappa}} - 1\right)}$$

The standard deviation for the flow angle, total and static pressure and the Mach number is calculated and given in the following Table 2.7.

Table 2.7: accuracy of calibration of 3-hole probe

	deviation	unit
φ	0.08	°
P_{static}	0.60	% of dynamic head
P_{total}	0.34	% of dynamic head
M	0.47	% of M

The two common parameters used to define a boundary layer are the displacement thickness δ^* and the momentum thickness θ, defined as:

$$\delta^* = \int \left(1 - \frac{U}{U_f}\right) dz$$

$$\theta = \int \frac{U}{U_f}\left(1 - \frac{U}{U_f}\right) dz$$

with the freestream velocity U_f and the velocity U at the position z above the surface at $z=0$. The shape factor H, defined as the quotient of δ^* and θ describes the

state of the boundary layer.

One value for each parameter describes the shape and state of the boundary layer for all performed experiments as they are all conducted with a similar Mach number and the maximum available boundary layer suction. The respective values are presented in Table 2.8, non-dimensionalized with the hole diameter d.

Table 2.8: boundary layer condition

displacement thickness δ^*/d	0.12
momentum thickness θ/d	0.05
shape factor H	2.31

The result of the boundary layer measurement was compared to well accepted theoretical considerations, for additional confirmation of the quality of the new wind tunnel. A turbulent boundary layer can be approximated according to Nikuradse [87]. The velocity distribution in the turbulent boundary layer of a smooth pipe is given by:

$$\frac{u}{U} = \left(\frac{r}{R}\right)^{\frac{1}{n}}$$

with the peak velocity U, the local velocity u at the location r and the pipe radius R. The exponent n depends on the Reynolds number, and is in the range from 6 to 10. Prandtl [92] assumed that the boundary layer on a flat plate develops essentially similar to the one inside a pipe. With that the velocity distribution can be written as:

$$\frac{u}{U_f} = \left(\frac{z}{\delta}\right)^{\frac{1}{7}}$$

the well-known 1/7 power-law with the free-stream velocity U_f and the boundary layer thickness δ.

The results are investigated regarding their dependency on Mach number and level of boundary layer suction. The shape of the profile is fairly independent of both parameters, as can be seen in Fig. 2.12. The measured data collapses towards the theoretical curve, despite the assumption of an infinite flat plate and a fully developed boundary layer. The latter assumption is not entirely true, as can be seen by the value of the shape factor.
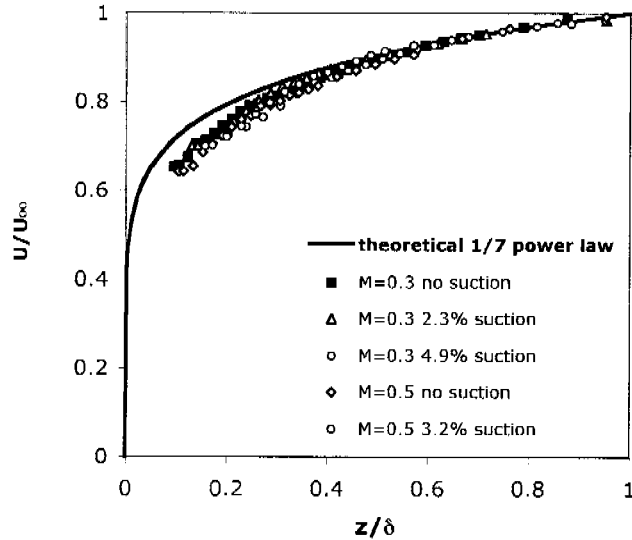
Figure 2.12: boundary layer shape

The thickness of the boundary layer is in the desired order of magnitude only when the boundary layer suction is running with its maximum capacity. Comparing the profiles at locations off the centre axis $Y=0$ showed rather symmetrical behaviour, again confirming the acceptable main flow quality.

2.6.2.7 Pressure Pulsation

The pulsator exit plenum contains a differential fast response pressure sensor manufactured by Endevco 8520A-20 with a pressure range of 20psi. The resulting signal is acquired by a fast PC card with a sampling rate of 100kHz and is analysed with a custom Labview module. The signal of the inductive trigger mounted on the pulsator shaft is recorded simultaneously. This procedure of quantifying the pulsation as a function of frequency and time averaged blowing ratio is performed once. This data set is later correlated with the unsteady flow data.

The pressure sensor is calibrated with a 2 point calibration for its static pressure signal with the signal from the pressure taps in the pulsator plenum. The respective accuracy of the pressure sensor is stated by the manufacturer, and given in the following Table 2.9

Table 2.9: accuracy of fast pressure transducer

point	FSO [psi]	FSO accuracy [%]	Deviation [Pa]
1	20	±0.1	140

The pressure pulsation is converted to pulsating blowing ratio $\tilde{BR}$ with the assumption that the plenum is large compared to the flow area through the cooling holes. This implies that the measured pulsating pressure is the total pressure. Furthermore, an isentropic assumption is made regarding the discharge coefficient c_d of the cooling holes. With that the discharge coefficient is $c_d = 1$. Now the Mach number through the cooling hole can be calculated, as the static pressure in the test section is known:

$$M = \sqrt{\frac{2}{\kappa - 1}\left(\left(\frac{p_t}{p_s}\right)^{\frac{\kappa-1}{\kappa}} - 1\right)}$$

The density of both flows and the speed of sound is known as well, and $\tilde{BR}$ can be calculated.

The results are summarized in the following Table 2.10. The phase shift is presented as difference between the peak of the positive slope of the trigger signal and the nearest peak of the blowing ratio as percentage of one pulsation cycle. A positive value corresponds to the blowing ratio peaking before the trigger signal and vice versa. The amplitude is both presented as absolute values and relative to the mean blowing ratio.

Table 2.10:summary of pulsation behaviour

		phase-shift	abs. amplitude $\tilde{BR}$		rel. amplitude $\tilde{BR}/BR_{mean}$	
f_r [/]	BR_{mean}	[%]	min [/]	max [/]	min [%]	max [%]
0.38	1	+12	-0.73	0.52	-73	+52
	2	+12	-0.79	0.50	-39	+25
1.88	1	-11.5	-0.20	0.17	-20	+17
	2	-11.5	-0.18	0.16	-9	8

The results show, that the shape of blowing ratio pulsation is strongly dependent on the pulsation frequency, but not on the mean blowing ratio. The following two figures 2.13 and 2.14 illustrate that clearly. The change of blowing ratio around the mean value over a period of pulsation is compared for similar blowing ratios.
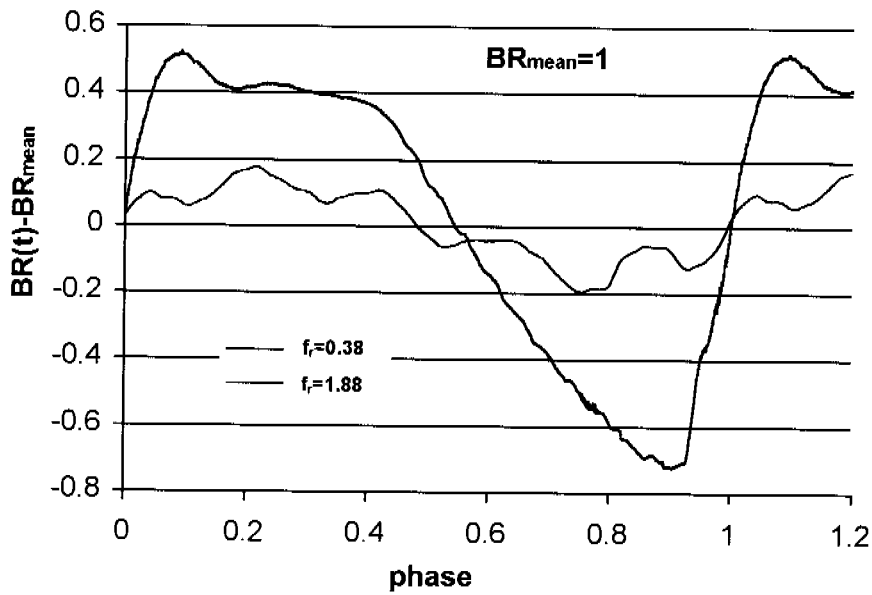
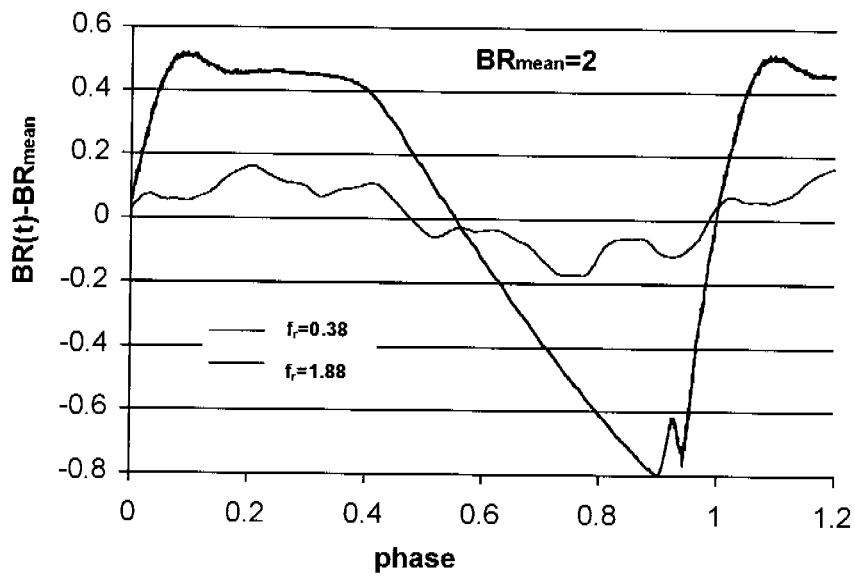**Figure 2.13:** variation of blowing ratio for a mean value of *BR=1*

Figure 2.14: variation of blowing ratio for a mean value of *BR=2*

It is visible, that the absolute amplitude of the unsteady blowing ratio is almost unaffected by the mean blowing ratio, but is a strong function of the pulsation fre-

quency. However, the amplitude relative to the mean level of blowing ratio differs by a factor of 2 between $BR=1$ and $BR=2$.

The general shape of the blowing ratio variation strongly depends on the two frequencies analysed. A smooth change is observed for $f_r=0.38$ with exception of a single peak just after the beginning of the positive slope for the higher mean blowing ratio. The shape is not symmetrical around the mean value. The positive part peaks to a level of $\tilde{BR}=0.5$ and then rests on a plateau, altogether for around 60% of the phase. The negative part has a more triangular shape, last for about 40% and bottoms to a level of $\tilde{BR}=-0.7$.

The case of $f_r=1.88$ shows triple peaks both on the positive and the negative slope. The peaks are probably associated with shock waves reflecting in the plenum of the pulsator. The shape is symmetrical around the mean value, the positive and the negative part of the variation last both for about 50% of the phase. The respective peaks are a bit less than $\tilde{BR}=\pm 0.2$

Another important aspect is the relation between the behaviour of the blowing ratio and the trigger signal. The analysis showed, that the mean value of blowing ratio has no influence on the shift between those unsteady events. Therefore, the following two figures show the relation of blowing ratio and trigger signal for a sample mean blowing ratio of $BR_{mean}=1$.
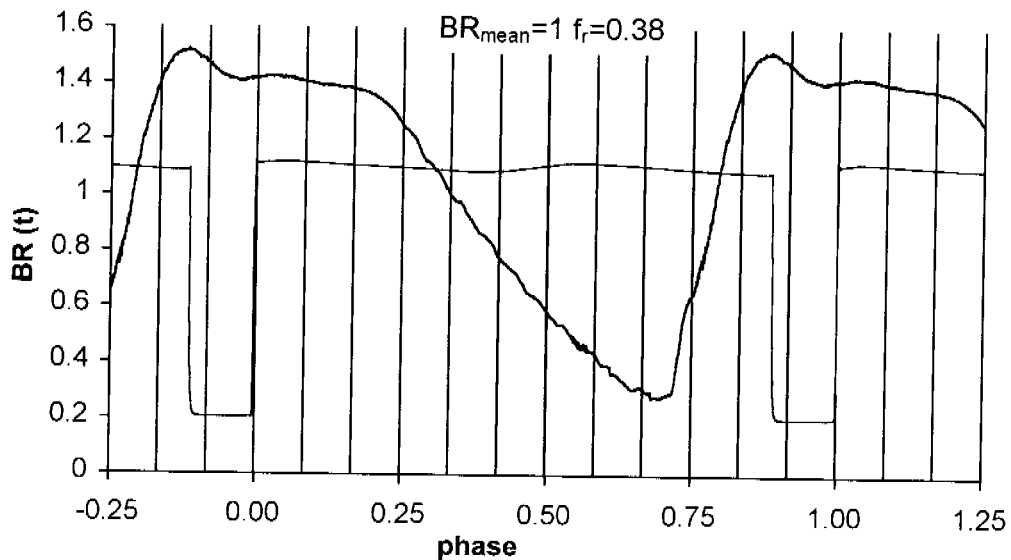

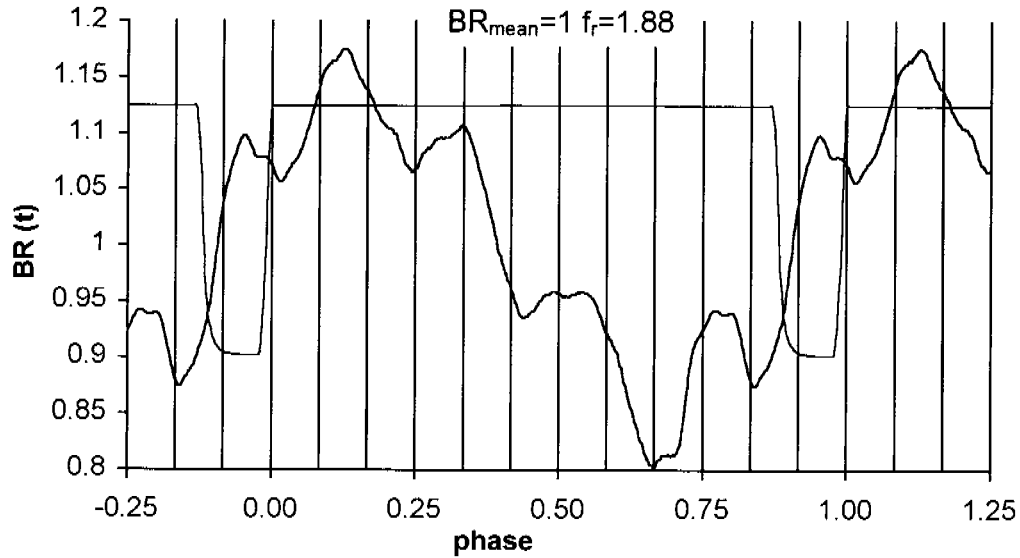**Figure 2.15:** relation between trigger and blowing ratio signal at $f_r=0.38$

Figure 2.16: relation between trigger and blowing ratio signal at f_r=1.88

The slot appears to open on the phase of 0.72 for both frequencies. The closing of the slot can be seen for the f_r=0.38 case at the phase of 0.87. The pressure continues to increase at f_r=1.88 after this phase position, probably due to continued shock activity.

2.6.3 Error Analysis

This section gives an error analysis of the measured parameters defined and described in the previous sections. The accuracy of the measurement devices is mentioned in detail in the respective sections. The error propagation of the systematic error of a result

$$R = X_1^a X_2^b X_3^c \ldots$$

is evaluated according to [60] as:

$$\frac{\partial R}{R} = \sqrt{\left(a\frac{\partial X_1}{X}\right)^2 + \left(b\frac{\partial X_2}{X}\right)^2 + \left(c\frac{\partial X_3}{X}\right)^2 + \ldots}$$

The respective accuracies of the directly measured values relevant to this error analysis are summarized in the following Table 2.11.

Table 2.11: uncertainties of measured values

parameter	typical value	deviation	relative accuracy [%]
$d_{orifice}$ [mm]	170	0.01	0.006
$D_{orifice}$ [mm]	250	0.01	0.004
$d_{cooling\ hole}$ [mm]	5	0.01	0.20
$z_{traverse}$ [mm]	1	0.1	0.1
A_m [mm^2]	7240	0.1	0.00014
A_c[mm^2]	137.4	0.0005	0.0004
$\Delta p_{orifice}$ [Pa]	104500	105	0.10
$p_{US\ -orifice}$ [Pa]	104500	52.5	0.05
p_m [Pa]	96400	52.5	0.05
p_c [Pa]	104500	157.5	0.15
$p_{c,tot}$ [Pa]	104500	140	0.13
T_m [K]	297	0.9	0.30
T_c [K]	220	0.25	0.11
m_c [g/s]	45	1.13	2.5
$m_{seeding}$ [g/s]	3	0.08	2.5
$m_{BL-suction}$ [g/s]	51	1.28	2.5
f [Hz]	42	0.05	0.12

The uncertainty of the derivatives is calculated from the data above according to the formula introduced above. In most cases it is a straightforward application of the involved equations. The uncertainty of the density ratio DR is given as an example:

$$\frac{\partial DR}{DR} = \sqrt{\left(\frac{\partial \rho_c}{\rho_c}\right)^2 + \left(\frac{\partial \rho_m}{\rho_m}\right)^2}$$

from the definition of the density ratio:

$$DR = \frac{\rho_c}{\rho_m}$$

with the uncertainty of the respective density:

$$\frac{\partial \rho}{\rho} = \sqrt{\left(\frac{\partial p}{p}\right)^2 + \left(\frac{\partial T}{T}\right)^2}$$

In case of the error analysis of the main flow mass flow rate establishing the uncertainty of the uncertainty proves slightly more complicated. The uncertainty of the

41

iteratively determined mass flow rate at the orifice plate is given in [10]:

$$\frac{\partial \dot{m}_{or}}{\dot{m}_{or}} = \sqrt{\left(\frac{\partial c_d}{c_d}\right)^2 + \left(\frac{\partial \varepsilon}{\varepsilon}\right)^2 + 4\frac{1}{\sqrt{1-\beta^4}}\left(\beta^8\left(\frac{\partial D_{or}}{D_{or}}\right)^2 + \left(\frac{\partial d_{or}}{d_{or}}\right)^2\right) + \left(\frac{\partial \Delta p_{or}}{2\Delta p_{or}}\right)^2 + \left(\frac{\partial \rho_m}{2\rho_m}\right)^2}$$

The separate coefficients can be easily determined with their respective definition given in Section 2.6.2.1. The total main flow mass flow rate assembles as:

$$\frac{\partial \dot{m}_m}{\dot{m}_m} = \frac{\left(\partial \dot{m}_{or} + \partial \dot{m}_{seed} + \partial \dot{m}_{BLsuc}\right)}{\left(\dot{m}_{or} + \dot{m}_{seed} - \dot{m}_{BLsuc}\right)}$$

To summarize, the uncertainty of all the relevant parameters is listed in Table 2.12.

Table 2.12: relative uncertainties of film cooling parameters

parameter	relative uncertainty [%]
M	0.52
DR	0.26
BR	2.60
IR	5.00
f_r	0.54
BR_	0.57
δ^*/d	1.02
θ/d	1.55

3. VELOCITY MEASUREMENT

The requirement to measure the velocity field in the near hole region of a film cooling hole included some additional aims. High accuracy and little disturbance of the flow by the measurement technique were desired. The ability to measure all 3 velocity components at each measured point inside a volume of measurement points phase resolved was an aim with high priority.

Several fundamentally different measurement techniques fulfil these requirements to different degrees. The choice was made to apply stereoscopic particle image velocimetry (3D PIV). A commercial measurement system was acquired and installed in the experimental facility. The working principle, the technical details and the theoretical background involved are all presented in the following sections.

3.1 Basic Principles of PIV

Particle Image Velocimetry PIV is a measurement technique for obtaining instantaneous whole field velocities. It is based on the fundamental definition of speed as the quotient of distance and time. The property actually measured is the distance travelled by particles in the flow within a known time interval. These particles are added to the flow and known as seeding. The seeding particles are chosen such, that they follow the flow (see Section 3.3.3). An area of the flow field is illuminated by a light-sheet in order to detect their movement. The light-sheet, which is generated by a laser and a system of optical components, is pulsed to produce an effect, that freezes the movement of the seeding particles. The time between the light pulses is the denominator in the equation above. To detect the position of the illuminated seeding particles for 2D PIV, one CCD-camera (Charge Coupled Device) is positioned at right angles to the light-sheet, and particle positions will appear as

light specks on a dark background in each camera frame. The pulsing light-sheet and the camera are synchronised so that particle positions at the instant of light pulse number 1 are registered in frame 1 of the camera, and particle positions from pulse number 2 are in frame 2.

The camera images are divided into rectangular regions called interrogation areas, and for each of these interrogation areas the image from the first and the second pulse of the light-sheet are correlated to produces an average particle displacement vector. Doing this for all interrogation regions produce a vector map of average particle displacements. Dividing with the known time between the two images captured, the displacement vectors are converted into a map of velocity vectors. To speed up the calculation of correlations, FFT-processing is used. All spatial information is sampled at the same time and there is a finite statistical probability there will be some regions where there is really no meaningful input. Therefore, it is necessary to subsequently validate the vector map. Validation algorithms are applied to the raw vector maps to detect and remove the erroneous vectors.

3D-PIV is based on stereo vision, the same fundamental principle as human eye-sight. As with 2D measurements, stereo-PIV measures displacements rather than actual velocities, and the two cameras look at the flow field from different angles. For each vector in the vector map, 3 true displacements $(\Delta X, \Delta Y, \Delta Z)$ are extracted from a pair of 2-dimensional displacements $(\Delta x, \Delta y)$ as seen from the left and right camera respectively. Basically, it is a question of solving 4 equations with 3 unknowns in a least squares manner.

Performing the 3D evaluation requires a numerical model describing how objects in 3-dimensional space are mapped onto the 2-dimensional image recorded by each of the cameras. Images of a calibration target are recorded, which contain calibration markers the true position of which are known. Comparing the known marker positions with the positions of their respective images on each camera image, model parameters are calculated.

The actual stereo-measurements start with conventional 2D-PIV processing of camera images recorded simultaneously with the left and right cameras. This produces two 2-dimensional vector maps representing the instantaneous flow field as seen from the left and right camera respectively. Using the camera calibrations these two 2D vector maps are combined to produce a single 3D vector map. Due to perspective distortion each camera covers a trapezoidal region of the light sheet, and their respective fields of view will only partly overlap each other.

For each flow condition and position Z above the surface a number of 30 double-frames is recorded with each camera to record an average of the instantaneous flow field. When measuring pulsating cooling the pulsation cycle is divided into 12

44

equal parts. The required reference trigger signal is the signal of the inductive sensor mounted on the pulsator, described in Chapter 2.6.1.

3.2 PIV System

The PIV System can be separated in several functional units, which are

- Illumination system

- Cameras

- Seeding system

- Traversing Unit

- System Unit

- PC

- PIV-Software

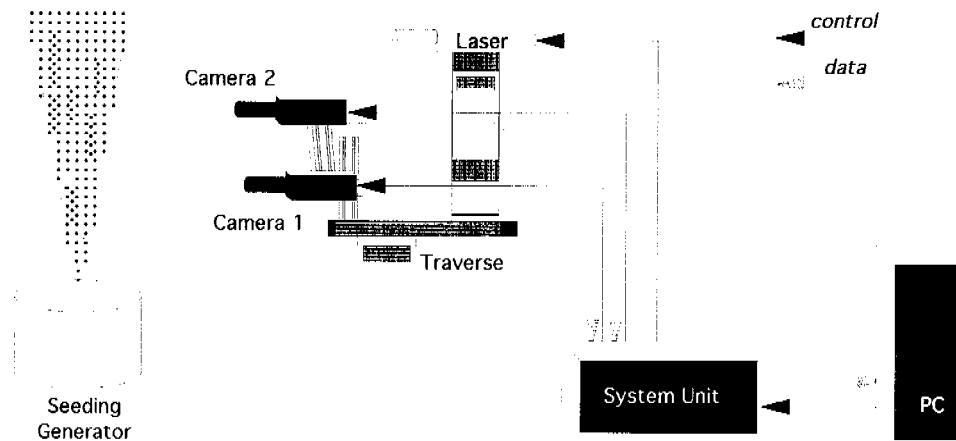Their connection and dependency is illustrated in Fig. 3.1, while their respective specifications and usage are described in detail in the following subsections.

Figure 3.1: PIV system overview

3.2.1 Illumination System

A pulsed Nd:YAG laser system is chosen as only this type of laser delivers sufficient energy to illuminate micron particles in a high speed airflow. The laser SOLO 120 is manufactured by New Wave Research Co. Ltd. Although the power is low with 120mJ per pulse, an equivalent energy of 12MW is emitted with each pulse with duration of 10ns.

The temporal range of pulse separations of this type of pulsed lasers is limited to 15Hz. The limitation in the range of pulse separations is overcome by using a double cavity Nd:YAG laser system. Two laser cavities are inserted into a housing which contains optics to combine the beam path. Each laser is operated in single Q-switch mode and electronics control the time interval between the emission of laser light from each laser. Using this method the range of pulse separations extends from 300ns to 300ms. Communication lines between the pulsed laser and the synchronisation unit in the system unit are required for user control of the data acquisition process (Fig. 3.1). Either the laser can run in a free-run mode where the laser informs the rest of the system that it is ready to emit laser light. Alternatively, the synchronisation unit instructs the laser cavities when to fire their flash lamps and when to allow their Q-switches to emit laser radiation.

Nd:YAG lasers emit light with a wavelength of 1064nm which is in the infrared. For PIV purposes, this wavelength is not very useful since most cameras are not sensitive to it. Generally cameras are more sensitive to the blue-green spectrum. Furthermore, there are many practical difficulties when attempting to align a beam path you cannot see, particularly when the laser power is a classified hazard. Therefore, for PIV, Q-switched YAG lasers are frequency-doubled. The wavelength of the laser pulse is halved to 532nm by a device called a second harmonic generator. Harmonic generators are not efficient and so there is a need to dump the residual infrared before allowing the pulsing beam to leave the laser. This is done by an optical component called a harmonic separator.

To achieve stable operation meeting the manufacturer's specifications, the YAG-laser must be operated at or near its design frequency. One of the reasons for this is the laser output is strongly dependent on cavity temperature, which will rise with increasing pulse frequency. Furthermore, it takes a while to reach thermal equilibrium and so the laser needs a warm-up period before starting the measurements.

The Nd:YAG-laser used does not have a Gaussian energy distribution. The energy distribution of pulsed lasers cannot be predicted very well, and two identical lasers will probably not have identical energy distributions. There will even be slight differences in the energy distribution of two consecutive pulses from the same laser.

46

3.2.2 Cameras

The purpose of the camera is to capture the initial and final positions of seeding particles in the flow field. The camera is placed at an angle to the light sheet. Seeding particles scatter light from the first pulse of the light sheet and the camera detects this scattered light, ideally as a bright signal on a dark background. Thus, the camera image map has sampled the initial positions of the seeding particles. The light sheet is switched off and the seeding particles are transported by the movement of the flow field. The second pulse of the light-sheet is fired and the seeding particles scatter light which is imaged onto the camera detector so the final positions of the seeding particles are sampled.

The CCD cameras provide an instantaneous digital signal of the image map of seeding particle positions. A CCD camera comprises an array of detectors called pixels. Each pixel is a MOS capacitor, being charged by converting incident photons of light into electrons, like in a photo diode. The cells are isolated from each other by potential wells, created by the doping of the silicon chip and by applying voltage to a grid of transparent metallic electrodes deposited on the CCD surface. Light falling on a pixel is thus converted into an electronic charge. The charge falling on the individual pixels is transformed to a voltage during read-out of the CCD chip and the value of the voltage is seen as a grey scale distribution on the PIV image map. Ideally, images should have a high charge i.e. appear white and the background noise level of the CCD chip should be low i.e. appear dark.

Cameras used for PIV have a progressive-scan-interline CCD chip that comprises both light-sensitive cells and an equal number of storage cells. The latter are not exposed to light. The first laser pulse is timed to expose the first frame, which is transferred from the light-sensitive cells to the storage cells immediately after the laser pulse. The second laser pulse is then fired to expose the second frame. The storage cells now contain the first frame and the light sensitive cells the second. These two frames are then transferred sequentially to the output shift-register. The storage cells are physically located adjacent to the light sensitive cells on the surface of the CCD-chip.

The number of vectors in the vector map is dependent upon the number of pixels the CCD camera and the size of the interrogation area used. The array of totally independent vectors is:

$$N_{vectors} = \frac{N_{pixels-CCDrow}}{N_{int}} \cdot \frac{N_{pixels-CCDcolumn}}{N_{int}}$$

where N_{int} is the side of the interrogation area in pixels. In practice, the number of independent vectors is greater. It is highly probable that if a particle has an image

near the outer edge of interrogation area its pair may be in the neighbouring interrogation area. That is, the particle images do not contribute to the calculation of a velocity vector. Therefore, successive interrogation areas are overlapped to optimize the use of the information in the image map. By overlapping interrogation areas the use of the available information is maximized. With 50% overlapping of interrogation areas the number of vectors obtained is:

$$N_{vectors} = \frac{N_{pixels-CCDrow}}{0.5 \cdot N_{int}} \cdot \frac{N_{pixels-CCDcolumn}}{0.5 \cdot N_{int}}$$

The choice of N_{int} is constrained by the conflicting constraints imposed by velocity dynamic range and spatial resolution considerations. Generally, an interrogation area side-length of 32 pixels provides a good compromise.

The dimensions of the interrogation area affect the upper limit of the velocity dynamic range, which is determined by the maximum spacing between successive particle images that can be measured. The displacement vector d_{max} corresponding to the maximum velocity vector in a flow field v_{max}, the time between successive pictures t and the object:image scaling factor S is:

$$d_{max} = v_{max} \frac{t}{S}$$

This displacement vector can only be measured if its magnitude is less than the dimension of the interrogation area N_{int}. Furthermore, the displacement vector should be a fraction of the interrogation region to ensure that there is no signal drop-out. The parameters t, S and N_{int} are chosen so that the following relationship is satisfied:

$$d_{max} = v_{max} \frac{t}{S} \leq 0.25 \cdot N_{int} d_{pitch}$$

with d_{pitch} being the spacing between the pixels on the CCD array. For a interrogation area with N_{int} the upper velocity limit corresponds to a pixel pitch of 8 pixels.

A dynamic range of only 9 discrete velocities can be achieved with standard procedures and an interrogation area size of 32x32 pixels. The smallest velocity corresponds to one pixel pitch. With the aid of subpixel interpolation this limitation is improved, with a minimum resolution of 1/64 of one pixel pitch (see also Section 3.6.3 and Section 3.6.8). To allow this, the particles have to appear over at least 3 pixels to satisfy the Nyquist-theorem [24] (see Section 3.6.2).

Two PCO SensiCam QE cameras are used in the PIV system. A standard photographic lens, a Nikon AF Micro-Niccor 60mm f/2.8 is mounted on each camera.

The dimension of the pixels on the cameras CCD-chip are $6.45 \times 6.45 \mu m^2$, with a total spatial resolution of 1280x1024pixel on the chip. The camera features a 2-stage peltier cooling of the sensor chip, keeping its temperature as low as $-12°C$, thus improving the signal-noise ratio. The dynamic range of the A/D converter is 12bit. The exposure time can be varied between 500ns and 1000s.

3.2.3 Traverse Unit

The PIV system's cameras and laser head are mounted on a 3 axis high precision traverse system. The linear traverses and their controller are manufactured by ISEL. The traversing motion is controlled via software running on the PC. The setup of all the components relative to each other and to the wind tunnel is described in Section 3.4.

The accuracy of positioning of each traverse is stated by the manufacturer as $\pm 0.05mm$. The speed of traversing can be varied between 1mm/s and 50mm/s.

3.2.4 PC

The PC used in the PIV system is a dual processor DELL PRECISION 530 with 1GB of RAM and a processor speed of 2GHz. The operating system is Windows 2000. The PC features a 20" flat screen monitor to facilitate the focusing process of the CCD cameras. This computer is the main-interface between user and PIV system. In detail, the following processes are performed on this PC:

- controlling the traverse units with TRAVERSEMANAGER

- setting up the PIV system with FLOWMANAGER via the system unit

- synchronizing the cameras and the laser during the measurements with FLOWMANAGER via the system unit

- storing and organizing the raw data received during a measurement from the system unit with FLOWMANAGER

- correlating the images and validating the results with FLOWMANAGER

- post processing the results with TECPLOT

The data of the measurements presented in this work are stored and backed up on four external hard disks with a total capacity of 2TB.

3.2.5 System Unit

The system unit Flow Map systemHUB, manufactured by Dantec Dynamics, is the centre part of the PIV system. It contains special input buffers that can simultaneously read image maps from a CCD camera, store image maps in a memory area and send the entire image to the PC. Furthermore, this process unit provides physical communication and synchronization links between the processor, the PC, the cameras and the laser.

The systemHUB has a Gigabit communication port that enables the fast delivery of image-data to the PC using the TCP/IP protocol.

3.2.6 Software

There are three software packages used during the measurement with the PIV system. The Dantec Dynamics FlowManager software is installed on the PC. This package provides the user interface, enabling the control of all components in the system. The FlowManager software is a visual database, which keeps track of the recorded data, the set-ups and the experimental configuration. Data analysis is available in the FlowManager Analysis option. Besides functioning as a database, the FlowManager software also controls the process unit through the use of online-menus. The communication with the system unit is performed by uploading set-up information and device drivers.

The software running on the system unit creates the necessary synchronisation sequences required for data acquisition. This is handled automatically by the system while being transparent to the user. The required synchronisation sequences are uploaded to the system unit via an Ethernet interface.

Inside the system unit, the synchronisation unit provides a physical platform for communication signals to and from the laser, the cameras and the external trigger devices. Thus a measurement sequence is initiated to generate input data, the images the camera detects. The cameras transmit the resulting image maps to the system unit for subsequent uploading to the PC. The software then stores the image maps in a database on the hard disc of the PC and keeps track of both the data and corresponding data acquisition and analysis parameters using the database.

The last, relatively small program used during a measurement is the package controlling the traverse unit.

TECPLOT is used as a tool for post processing the acquired data. This allows a vast amount of manipulations and graphical representations of the data.

3.3 Seeding

In PIV it is not actually the velocity of the flow that is measured, but the velocity of particles suspended in the flow. In this respect these seeding particles can be considered to be the actual velocity probes, and seeding considerations are thus important in PIV. The particles must be small enough to track the flow accurately, yet large enough to scatter sufficient light for the camera to be able to detect them. Ideally, the particles should also be neutrally buoyant in the fluid. Particles whose motion is used to represent that of a fluid continuum should be:

- Able to follow the flow

- Good light scatterers

- Conveniently generated

- Cheap

- Non-toxic, non-corrosive, non-abrasive.

- Non-volatile, or slow to evaporate

- Chemically inactive

Beside the high requirements on the seeding particles due the complex flow field further difficulties due to the thermal conditions of both flows are considered in the choice of seeding material and generation.

After research of literature and several experiments the oil Dioctylsebacat DEHS is chosen as the seeding material to be used in aerosol generators. This material is non-toxic, non-carcinogenic, and only slightly corrosive towards gaskets and paint. It is of low enough volatility to partly recirculate in the closed loop wind tunnel. However, unlike other oils it will completely evaporate eventually, reducing the long-lasting contamination. DEHS is an organic material ($C_{26}H_{50}O_4$). It is combustible and open flames have to be prevented. Since the flash point of DEHS is high (ca. 210°C) a danger due to explosion is not present in the current test facility. The lower explosive limit can be calculated from the flash point. The saturated vapour pressure p_d at this temperature is 150.8Pa and gas constant of DEHS R_{DEHS} is 19.48J/kg/K. The explosive limit in vol.% in air is 2.2. Tests confirm that the DEHS-particles survive in a 120°C environment, are detectable and available in sufficient quantity to allow a successful correlation of the recorded images.

The seeding for the main flow is generated by an in-house designed and manu-factured seeding generator. The seeding for the cooling flow is generated with a Laskin-Nozzle atomizer. Both generators produce particles with a mean diameter of below 4μm, which fulfil the requirements on tracking capabilities.

Injection into the main flow is achieved by means of 2 tubes with many discrete holes that release aerosol far upstream of the test section (see also Fig. 2.2). The injection of seeding into the coolant flow is done via a T-flange 1.5m upstream of the pulsator.

3.3.1 Seeding Generation

The particle size distribution of the generated aerosol is important for the quality and reliability of the PIV measurements. The particles should be of a narrow band-width regarding the size and monodisperse to permit reliable statements about their respective quality in the PIV application.

The measurement of the particle size was done with a Sympatec-BSM (Beu-gungs-Spektro-Meter). This machine classifies the particles in 32 discrete radius ranges within the total range of diameter from 0.2μm to 35μm. The results of the measurements are given as a particle volume distribution, which is the measure of the total particle volume that is occupied by the particles of a certain size (i.e. how many percent of the volume is occupied by particles larger than 3μm and smaller than 4.2μm).

The number of particles within a certain diameter range is the particle count dis-tribution. The conversion of the particle volume distribution to a particle count dis-tribution is performed, as this is the relevant quantity for seeding.

The two particle generators used in this research are presented in the following section and their working principle is explained.

3.3.1.1 Laskin Atomizer

This commercial DLR-40 seeding generator is manufactured by PIVTEC. Air or gas is blown through four holes in a tube in the liquid located in a reservoir. The tube is closed at its lower end. These four sonic jets then suck liquid through verti-cal holes in the ring, to produce air bubbles containing finely atomized droplets, Fig. 3.2. As the bubbles rise to the liquid surface, the droplets are released into the gas stream. An impactor plate is necessary to remove larger droplets from the poly-disperse spray.
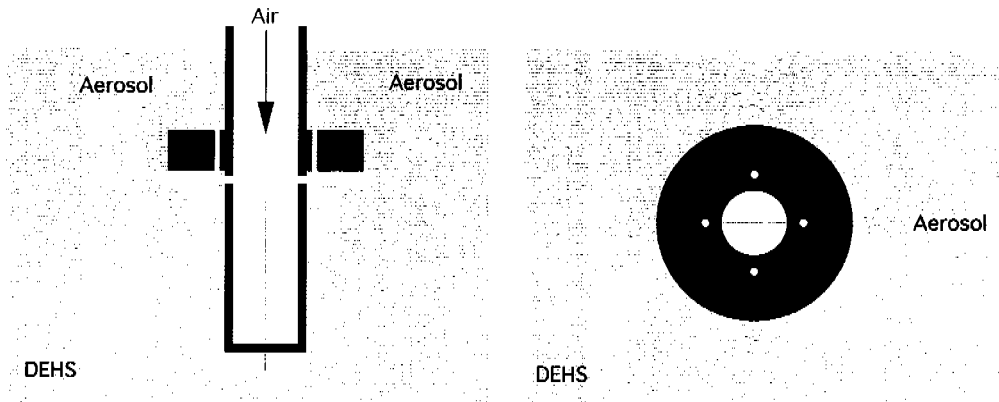
Figure 3.2: working principle of a Laskin nozzle

The particle concentration can be adjusted with the volume air flow within a defined range of inlet pressure between 0.5bar and 1bar over pressure, which is governed by the choke limit of the jets and the required jet intensity for particle generation. Other than by the method described the concentration can only be decreased by dilution of the air supply. By adding Laskin nozzles the particle production can be increased. The seeding generator is equipped with 40 Laskin nozzles.

With this design the particle size is mostly independent on the volume air flow through the generator. The liquid material has the main influence on the particle size. The measured data showed no difference in particle size within the measurement accuracy of the BSM while varying the pressure difference between inlet and outlet. The number of laskin-nozzle arrays was varied between 1 and 5. The difference of particle size distribution due to that variation was below 1%.

The measured particle volume distribution is shown in Fig. 3.3. The corresponding numbers are: $x_{10}=3\mu m$, $x_{50}=3.43\mu m$, $x_{99}=4.95\mu m$.
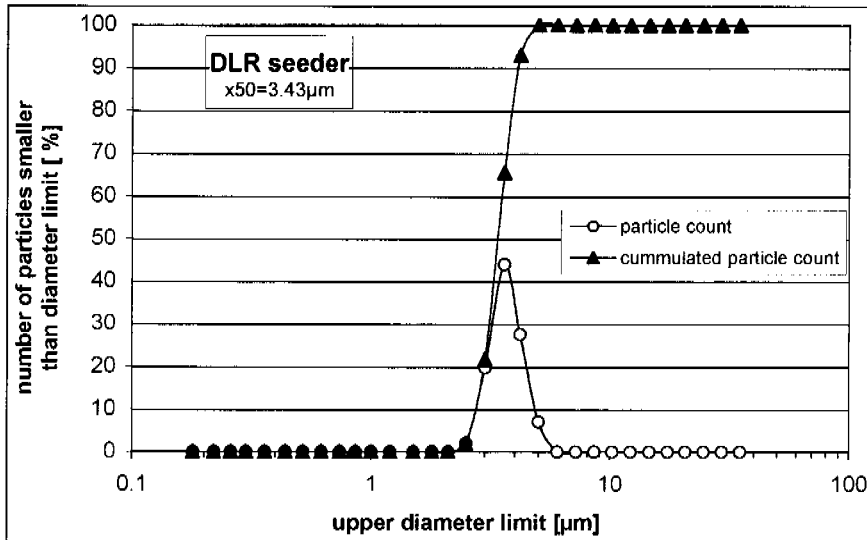
Figure 3.3: particle size distribution of DLR seeder

3.3.1.2 LSM Seeding Generator

This seeding generator was designed and manufactured after several experiments with different seeding generators. The working principle is shown in Fig. 3.4.
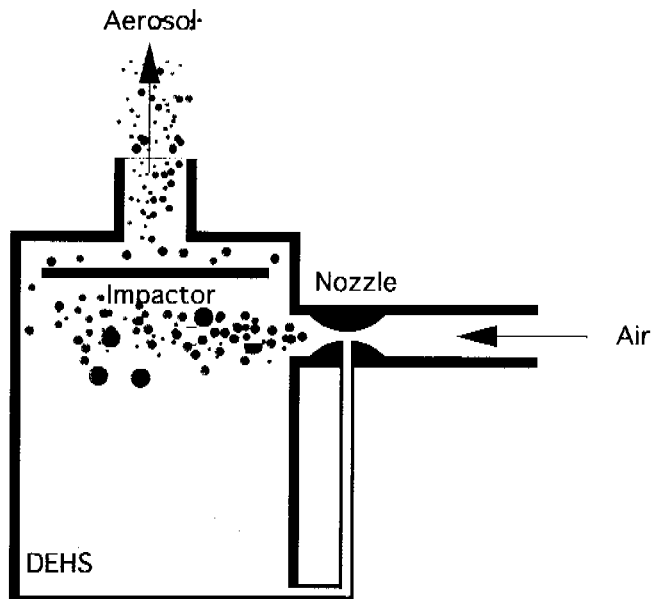

Figure 3.4: working principle of LSM seeding generator

The generator consists of a pressure vessel with a spray nozzle blowing horizontally into the vessel. DEHS is drawn from the pressure vessel reservoir by the low static pressure of the entraining gas jet and forms a liquid spray. The spray nozzle produces a polydisperse spray. Large droplets are removed with the aid of an impactor, consisting of a plate in front of the aerosol outlet.

The particle concentration proved to be constantly high, independent of pressure levels at the inlet and outlet of the generator. The corresponding particle size distribution is shown in Fig. 3.5.
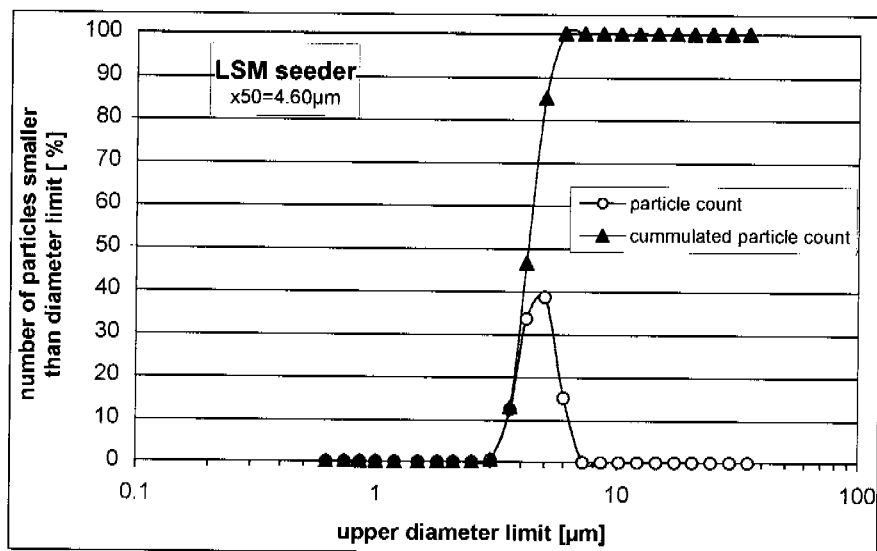
Figure 3.5: particle size distribution of LSM seeder

The distribution of particles size is spread slightly wider than the one of the DLR seeder, the average diameter is about 1μm bigger. Another difference was the occurrence of a number of over 98% of particles smaller than 0.3μm diameter, although they only occupy 2% of the total particle volume. As discussed in the introduction and proven by experiments, these small particles, with sizes smaller than the wavelength of the laser light, have no noticable influence on the captured pictures. Taking the small particles out of the distribution, and plotting the particle number distribution gives the result shown in Fig. 3.5. The mean particle diameter is 4.60μm, the largest particles are smaller than 6μm, the smallest relevant particles are larger than 2.5μm. Thus the total bandwidth of relevant particle diameter is less than 3.5μm.

3.3.2 Seeding Injection

The equipment to inject seeding consists of two brass tubes with an inner diameter of 20mm. They are plugged into the tunnel and are fixed by a nut and a rubber core, which has an additional sealing function. Fig. 3.6.
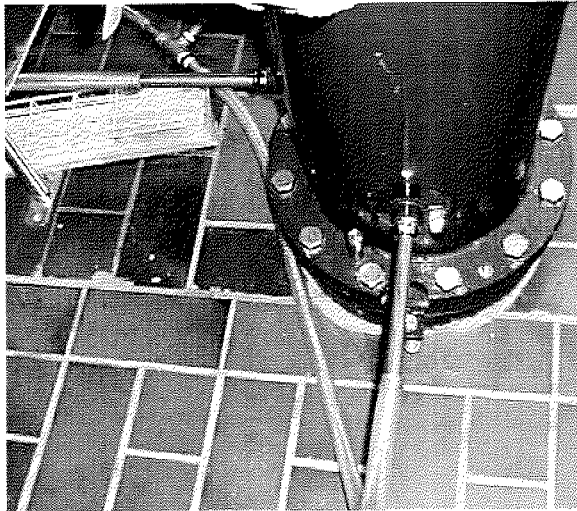

Figure 3.6: seeding tubes upstream of the heat exchanger

Holes (2mm) are distributed along the half circumference with 5 holes per row and are non-uniformly distributed regarding to the length of the tube (see Fig. 3.7).
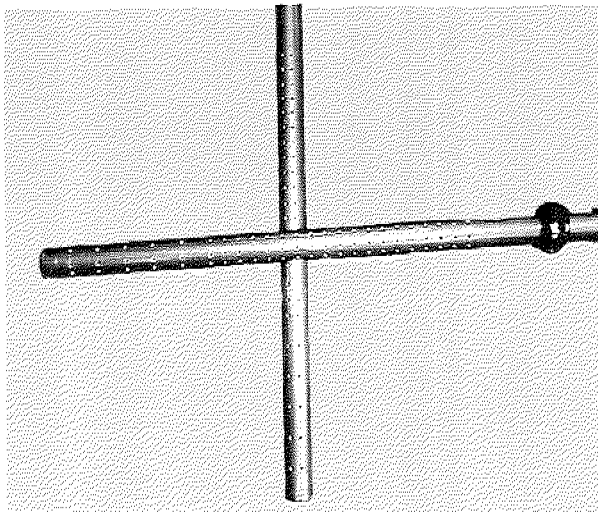

Figure 3.7: arrangement of the seeding tubes

In the last third of the tube the distance between circumferential sets of holes is doubled compared to the rest of the tube. These features of the feeding design, like the hole distribution and the crosswise arrangement of the tubes together with the heat exchanger and the honey comb, support the uniform distribution of particles across the whole cross section of the tunnel.

Extensive testing confirmed a sufficiently uniform particle distribution in the whole test section due to this injection arrangement. The contamination of the windows is strongly influenced by the location of the injection of seeding into the main flow. The best results are achieved with the described arrangement. The main flow can be seeded continuously for 1.5 hours before cleaning is necessary.

3.3.3 Theory

There are two conflicting factors, which determine the size of an ideal seeding particle. On the one side, the tracking capabilities of the particles should be as good as possible in order to avoid significant discrepancies between fluid and particle motion. Especially in gas flows, where usually the density ratio between particle and fluid is very high (>1000), this requirement has to be considered thoroughly.

On the other side the particles should be detectable with the given laser power. Besides the particle material and geometry the particle size determines the scattered light power to a high degree.

Due to the trade off characteristic of the relation between tracer capability and particle size and the relation between scattering capability and particle size, the optimal size is a result of a compromise between these two relations (see Fig. 3.8).
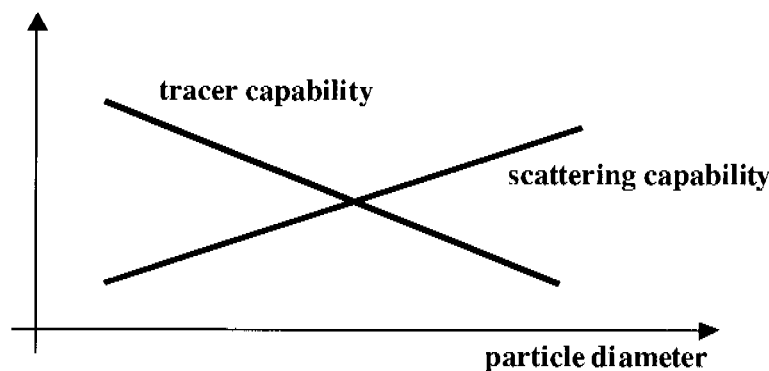

Figure 3.8: trade off between tracer and scattering capability

3.3.3.1 Tracking Behaviour

In general the motion of particles suspended in a fluid is affected by

- Particle shape

- Particle size

- Relative density of particle and fluid

- Concentration of particles in the fluid

- Body forces

The shape of the seeding particles affects the drag exerted on the particle by the surrounding fluid, and the size of the particles along with their relative density influence their response to velocity changes of the surrounding fluid. The concentration of particles affects particle motion through interaction between different particles. In practice the concentrations used are normally so low, that the particles on the average are separated from each other by several particle-diameters, so the particle interaction can be neglected. Also body forces, such as gravity, can normally be neglected, except in very slow flows, where buoyancy of the seeding particles may be an issue. The tracking behaviour does impact on the measurement accuracy. Therefore, the two relevant aspects of the particle behaviour in a vortical structure and a turbulent flow are discussed in detail in the error analysis at the end of this chapter (Section 3.9).

3.3.3.2 Scattering Behaviour

PIV is based on light scattered sideways. In this context forward, backward and sideways refer to the direction of the incident light. Forward scatter means away from the light source, backward scatter towards it. Small particles generally scatter most light in the forward direction, somewhat less in the backward direction, and very little light is scattered sideways.

Depending on the nature of the flow, seeding particles used for PIV-measurements usually have particle diameters ranging from 0.1 to 50μm. This is comparable to the wavelength of the light used, which for the frequency-doubled Nd:YAG laser is 0.532μm.

With particle sizes comparable to the wavelength of light, the Lorenz-Mie light scattering theory applies. This theory considers spherical particles, and thus describes only the dependence on particle size, but in practice also the shape and orientation of seeding particles play a major role in the scattering of light.

In general large particles scatter more light than smaller ones, but particle size also affects the spatial distribution of the scattered light. For large particles the ratio of forward to backward scattered light can thus be in the order of 10^2 to 10^3, where smaller particles scatter more evenly. The light scattered sideways is of highest interest for PIV, which is low even for large seeding particles.

For large seeding particles, direct surface reflection generally dominate the scattered light, and the intensity is thus roughly proportional to the square of the particle diameter. For smaller particles diffraction plays a major role in the light scattering, and polarisation of the incident light has significant influence. This is particularly important when using submicron-seeding particles, which may be required for measuring supersonic flows and/or shocks. In such cases the incident light should be polarised parallel to the light sheet to produce maximum intensity in the light scattered sideways.

It is clear that the larger the particle is, the better the scattering capabilities are. So the following consideration has the goal to find information about the minimal particle size, which is just detectable by the laser system. The consideration is based on Melling [85] and Raffel et al. [93]. For spherical particles with diameters larger than the wavelength of incident light Mie scattering occurs.

A convenient measure of the light scattering capability is the cross section C_s, defined as the ratio of the total scattered power P_s to the laser intensity I_o incident on the particle:

$$C_S = \frac{P_s}{I_o}$$

The cross section C_s is a function of the particle diameter d_p, the laser wave length l and the particle size range n.

$$C_s \propto \left(\frac{d_p}{\lambda}\right)^n$$

The scattering efficiency is strongly dependent on the ratio of the refractive index of the particle to that of the fluid. The scattering of particles in air is at least one order of magnitude stronger compared to particles of the same size in water.

In the size range below 0.5μm the dependence on particle size is very strong ($n=4$), as illustrated in the Fig. 3.9 (from Raffel et.al [93]). This is the range where Rayleigh scattering occurs, which is orders of magnitude smaller than Mie scattering. This is the reason why the detection of particles below this size is difficult. The scattering capability of a molecule (nitrogen or oxygen) is 21 orders of magnitude smaller than the scattering capability of an 1μm-particle.

Rayleigh
Scattering

$$C_S \propto \left(\frac{d_p}{\lambda}\right)^4$$

Mie Scattering
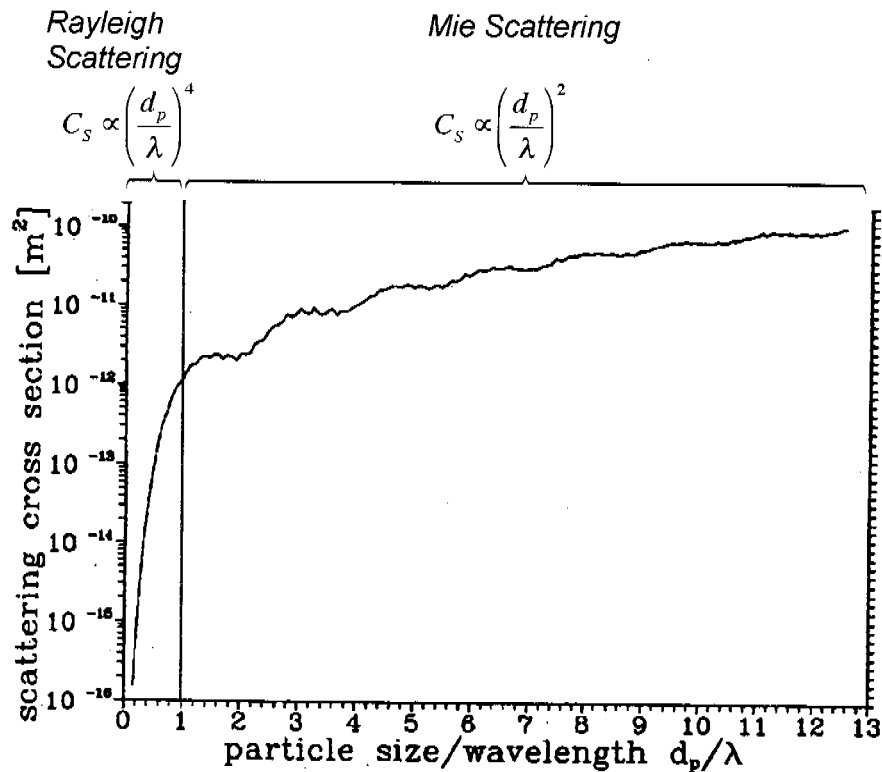
$$C_S \propto \left(\frac{d_p}{\lambda}\right)^2$$

Figure 3.9: scattering cross section as a function of particle size

A further feature of particle light scattering is the angular variation of the scattered light, which depends on the ratio of particle diameter and wavelength of the incident light b .

The following behaviour can be observed:

- For increasing b the ratio of forward to backward scatter intensity $I_{180°}/I_{0°}$ will increase rapidly.

- For increasing b the ratio of scatter intensity perpendicular to the incident light to forward scatter intensity $I_{90°}/I_{180°}$ decreases.

Fig. 3.10 illustrates this phenomenon on the basis of polar distribution of scattered light intensity by glass particles suspended in water (from Raffel et.al [93]). It has to be noted that the intensity scales are logarithmic and are plotted so that the intensity for neighbouring circles differ by a factor of 100.
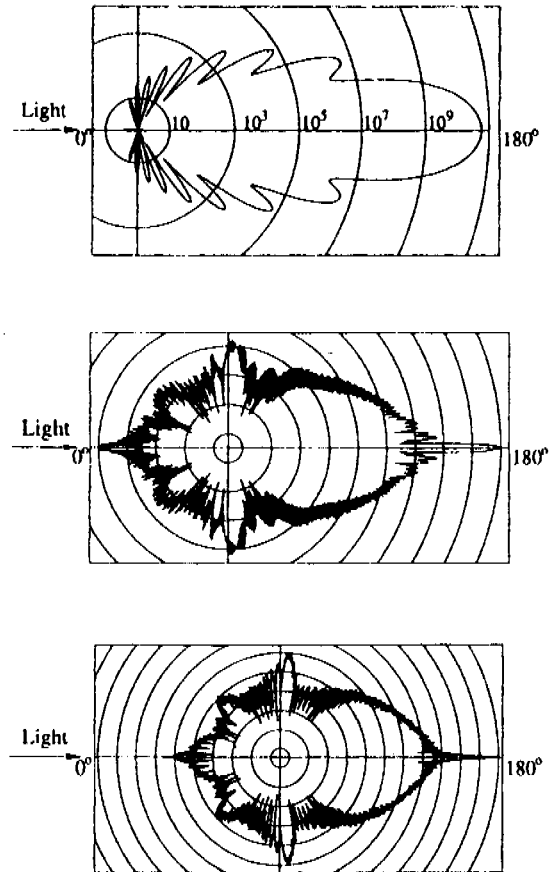
Figure 3.10: light scattered by a 1μm glass particle in water, diameter 1μm, 10μm, 30μm from top to bottom

The forward scatter intensity always dominates the 90° scatter intensity. Due to the limited depth of field, 90° recording is most often employed compared to the more advantageous forward scatter recording method. The fact that the scattered light is not blocked, but instead spread by the particles in all directions, causes illumination of neighbouring particles. This illumination can be used to increase the scattering efficiency with the addition of more particles to the flow.

3.4 Setup

This section describes the rather complex arrangement of the separate parts of the PIV system relative to each other and to the wind tunnel. Also the specific preparations for setting up the system to perform measurements are explained.
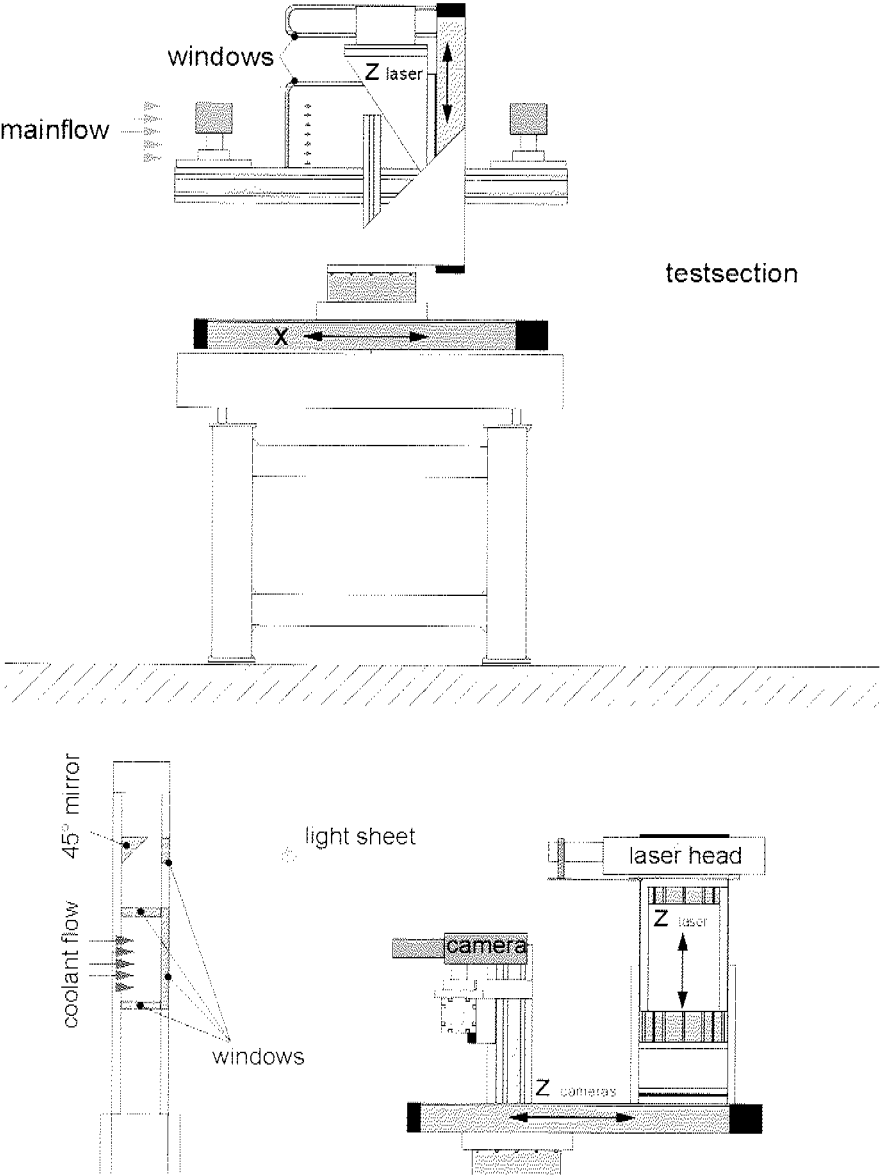

Figure 3.11: mounting of PIV system

The wind tunnel and the PIV-hardware are not physically connected, with exception of the two seeding generators. The arrangement of the laser head, cameras, traverse system and test section is shown in Fig. 3.11. A massive cast iron table stands in front of the test section of the wind tunnel. This table supports the PIV traverse system. One axis translates the assembly of cameras and laser head parallel to the main flow direction X. The second axis translates the assembly towards the test section, in Z direction. The third axis translates the laser head in vertical direction Z_{laser}. All three axis are aligned to the test section with an accuracy of ±0.1mm to ensure the validity of the global calibration approach.

Simultaneous traversing of the laser in vertical direction (Z_{laser} in Fig. 3.11) with traversing of the cameras in horizontal direction ($Z_{cameras}$ in Fig. 3.11) allows the scanning of the flow volume in Z-direction without the need of re-calibration for every light sheet position.

The cameras each rest on a Scheimpflug mount. This device, as shown in Fig. 3.12, is required as the cameras look at an angle on the object plane, the light sheet. Without such a mount the best plane of focus is parallel to the image sensor and not to the plane of the laser light sheet. Therefore the Scheimpflug principle is used. This arrangement where the object plane, the image plane (CCD-plane) and the plane of the imaging lens intersect at a common point realises complete focus at the image plane for all off-axis camera angles (see Fig. 3.12).
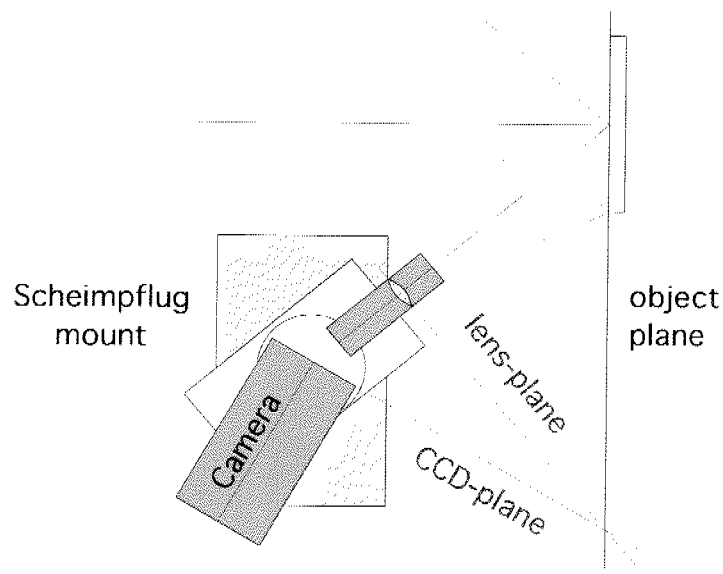

Figure 3.12: Scheimpflug camera mount

The Scheimpflug mount makes it possible to tilt the CCD plane relative to the lens-plane around one axis (CCD-axis) and it makes it possible to rotate the connected whole camera set-up around the CCD-axis. The gap between the camera and the lens holder is enclosed by a flexible bellows to prevent surrounding light from reaching the CCD-chip. The Scheimpflug arrangement like any other off-axis arrangement introduces perspective distortion. This means that the velocity vectors have to be transformed to convert them from images to non-distorted fluid space velocity vectors. This will be discussed further in the section about calibration.

The height of the cameras is adjusted so they look at the centre of the test section regarding the Y coordinate. The angle of the cameras is adjusted so that a maximum overlap of both images is achieved. The focus of each camera is adjusted in the centre of each image. After that step the Scheimpflug mount is adjusted for each camera to obtain best focus on both sides of the centre of each image.

The laser head is mounted on a third traverse axis. The light sheet optics, which are directly connected with the laser, create a light sheet in XY-orientation with variable thickness. The path of the lightsheet inside the test section is illustrated in Fig. 3.13. The lightsheet exits the optics in horizontal orientation and enters the wind tunnel through a 15mm heat resistant quartz window. It then gets reflected downwards via a high precision surface coated silver mirror that is mounted at 45° inside the wind tunnel. The lightsheet enters the test section via another quartz window from top leaves via a third window at the bottom and gets finally dispersed in the cavity below the test section.

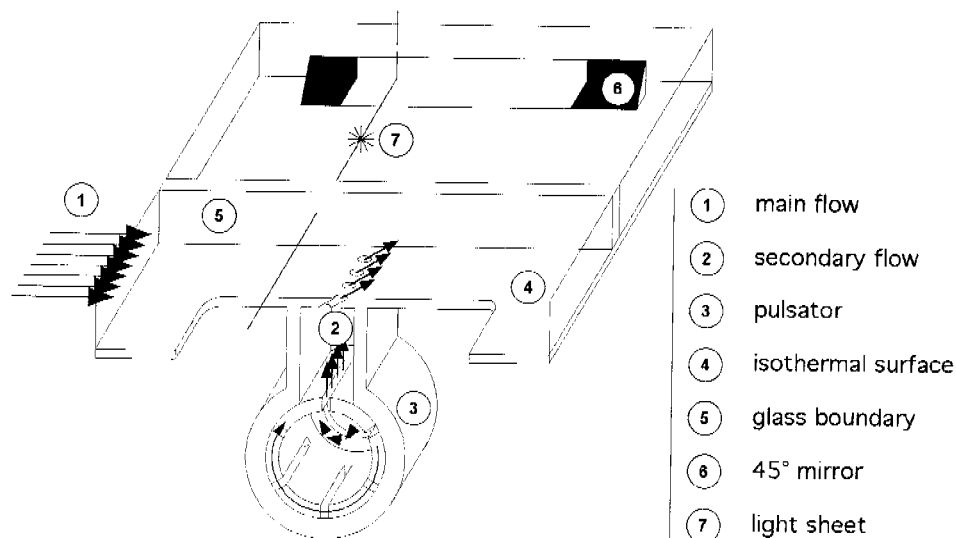|	
1	main flow
2	secondary flow
3	pulsator
4	isothermal surface
5	glass boundary
6	45° mirror
7	light sheet

Figure 3.13: schematic of injection arrangement

The alignment of the lasersheet parallel to the test section is of importance for the accuracy of the reconstruction of the 3D vectors from the two camera images. The positioning of the lightsheet is of importance for the reconstruction of the flow volume from the separate vector planes.

The required laser sheet thickness is around twice the size of the interrogation area projected out in object space. The factor 2 is necessary to compensate for the Gaussian distribution of the light intensity.

3.5 Calibration

The mapping of the displacements from the CCD-plane to the object plane in fluid space can be performed, provided it is known how points in the object plane are imaged onto the CCD-plane. This knowledge is acquired by the calibration procedure. The calibration uses a well defined grid of dots inserted in the test section. The calibration target is aligned with the light sheet and the cameras are traversed relative to the target in several positions. The dots on the calibration target are used to calculate a linear calibration equation for each camera. The linear calibration will compensate for difference in scale and lack of orthogonality (e.g. perspective). An example of such an imaging model is the pinhole camera model, which based on geometrical optics leads to the so-called Direct Linear Transform (DLT):

$$
\begin{bmatrix} kx \\ ky \\ k \end{bmatrix} = \begin{bmatrix} A_{11} & A_{12} & A_{13} & A_{14} \\ A_{21} & A_{22} & A_{23} & A_{24} \\ A_{31} & A_{32} & A_{33} & A_{34} \end{bmatrix} \cdot \begin{bmatrix} X \\ Y \\ Z \\ 1 \end{bmatrix}
$$

where uppercase symbols X, Y and Z are used for object coordinates, and lowercase symbols x and y represent image coordinates. With imaging models based on physics, calibration coefficients can in principle be calculated from known angles, distances and so on. In practice, however, this approach is not feasible since in the actual experimental set-up in the laboratory it is very difficult to measure the relevant angles, distances and so on with sufficient accuracy. An experimental approach to camera calibration is therefore used. Images of a calibration target are recorded, which contain calibration markers whose true (X,Y,Z) positions are known. Comparing the known marker positions with the positions of their respective images in each camera image, the model parameters are calculated

The calibration target contains a grid of white dots on a black background. It is important to know the exact dot spacing since the grid defines the coordinate sys-

tem. In the centre of the target is a larger dot surrounded by four smaller dots. By definition the larger dot is the origin of the coordinate system $(0,0,Z)$ and the common fixed point for the two cameras. The four smaller points identify the X- and the Y-axes. Therefore both cameras must be able to see the large dot surrounded by the four smaller ones. As the area of interest varies for the different measurements the calibration targets are self made according to the recommended guidelines by Dantec Dynamics. The target as shown in Fig. 3.14 used for all the measurements of film cooling flow has a spacing of the dots of 5mm, with a centre marker of 3mm diameter, axis markers of 1mm diameter and general markers of 2mm diameter. The number of dots is 385.
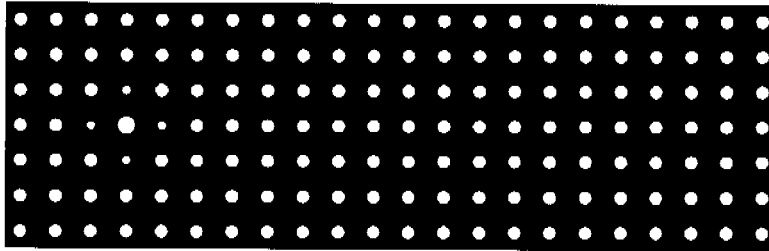
Figure 3.14: calibration target

Image processing parameters

Camera calibration is the task of modifying the parameters of an imaging model to make the model match sample observations as good as possible. The image model relys on a sample observation where corresponding object- and image-coordinates are known. Identifying markers in an image and determining their coordinates requires image processing. The first step in identifying markers is to binarize the calibration images using a threshold value determined from the grayscale histogram of each image. The threshold is determined as the grayscale value midway between two peaks. The targets have white markers on a black background. In the binarized (black-and-white) image neighbouring pixels of identical colour are grouped into so-called objects, and for each object the area and the centroid position is calculated. Each calibration marker corresponds to an object. Objects touching the image boundary are discarded, since they are assumed to extend beyond the boundary and thus will be clipped, making the calculated centroid position invalid.

From the remaining objects the mean area is calculated, and a range of acceptable areas determined:

$$A_{min} = \frac{A_{mean}}{DAT} \frac{D^2_{axis}}{D^2_{std}} \qquad A_{max} = A_{mean} \cdot DAT \frac{D^2_{axis}}{D^2_{std}}$$

Objects smaller than A_{min} or larger than A_{max} are discarded and on the basis of the remaining objects A_{mean} is recalculated for later use. Nominal dot diameters D_{Axis}, D_{Std} and D_{Zero} are taken from the target specifications and are included to account for the fact that not all markers have the same size. Beyond this, the dot area tolerance (DAT) accounts for variations due to perspective as well as normal variations in the images. Dot area tolerance is a variable value >1.

The remaining objects are all assumed to be calibration markers, and it is verified that there is at least a (specified) minimum dot count within each calibration image. The default value is 25, corresponding to a grid of 5x5 markers.

Among the remaining objects the largest one is assumed to be the zero marker. The four nearest neighbours are found in directions up, down, left and right of the assumed zero marker. These are assumed to be axis markers. Centroid coordinates (X,Y) of each marker are stored as well to facilitate the imaging model fit.

To perform a calibration the target is placed in the test section. The target is aligned with the light sheet with the aid of fluorescent markers. The cameras both take a picture of the target and are then traversed to the next position orthogonal to the target. This is done for 5 different positions. This set of pictures is analysed as described above to detect the points. With the information of the coordinates of the points the conversion matrix is established for each camera. These matrices are used later to convert the acquired 2D vector fields from each camera into one 2D plane containing 3D vectors. This plane is in the same orientation as the light sheet.

With the present setup of straight windows and a rectangular test section it is possible to have a global approach of calibration, enabling a single calibration for all XY-positions of the set-up of cameras and laser head. The calibration is done once at any given location in X and Y direction and is assumed to be valid at all other X and Y locations. This assumption has been checked experimentally and has shown good validity. The difference of accuracy of the calibration at different X-positions changed less than 0.3%.

3.6 Correlation

This section describes the mathematics used in the FlowMap software to perform the correlation of the recorded particle images, which consists of several steps. First the recorded image is separated into interrogation areas. Initially no offset is introduced from the first window, the interrogation area in the image frame from

laser pulse one, to the second window. Second, the particles in these areas are detected. Third, the particle positions in the first frame are correlated with particle positions in the second frame. This leads to the initial vector map. Fourth, validation procedures are applied to detect and remove faulty vectors. The now obtained vectors are used as an estimate for the window offset for the next correlation. A new run is made, but this time with a smaller interrogation area. The main benefit derived from using the shifted window is capturing the particle images that left the interrogation area during the time between the two light pulses. Loss of these particles reduces signal strength and the number of successful vectors that can be obtained.

This adaptive procedure is performed twice with decreasing window size for each step, until the final interrogation area size of 32x32 pixels is reached. The results obtained proved to give very reliable data, reducing the negative influence of background reflection and non-uniform seeding density strongly. More details about the accuracy can be found in the section about error assessment.

3.6.1 Coordinate System

The software uses a Cartesian coordinate system with the XY-plane coinciding with the light-sheet and thus with the surface such that the positive X-axis points to the right and the positive Y-axis points upwards as seen when observing the light-sheet from behind the camera. It is thus the light-sheet and the orientation of the camera that define the coordinate system. The origin is in the lower left corner of the observed area corresponding to the bottom left-hand pixel in the camera image. The following uses symbols like (i,j), (k,l) and (m,n) to describe image-coordinates measured in pixels, while the symbols (x,y) are used for object-coordinates measured in SI-units.

3.6.2 Cross Correlation

The following description of the applied cross correlation process is based on Willert et.al [110]. In PIV two sequential image maps are sub-sampled. The resolution of the sub-sampling is defined as an interrogation area and the interrogation areas form a regular array. Within these interrogation area samples, an average spatial shift of seeding particles may be observed from one sample to its counterpart in the second camera image, provided a flow is present in the illuminated plane.

The function $f(m,n)$ describes the light intensity within the interrogation area recorded at time t, and the function $g(m,n)$ describes the light intensity recorded at

time $t+\Delta t$. The latter can be considered the output of an image transfer function $s(m,n)$, taking $f(m,n)$ as input, and with the noise function $d(m,n)$ added. Capitalized functions are the Fourier transforms of the corresponding lower case functions, and (u,v) are coordinates in the spatial frequency domain. The spatial shifting function $s(m,n)$ is directly related to the flow and the time between the two recordings, while the noise function $d(m,n)$ is a result of seeding particles moving into or out of the interrogation area in the period between the two recordings. The major task in PIV is the estimation of the spatial shifting function $s(m,n)$ on the basis of the measured values of $f(m,n)$ and $g(m,n)$, but the presence of noise complicates matters. The method chosen to estimate the displacement function $s(m,n)$ is the statistical technique of spatial cross-correlation. The discrete cross-correlation function $\phi_{fg}(m,n)$ of the sampled regions $f(m,n)$ and $g(m,n)$ is given by the expected value:

$$\phi_{fg}(m,n) = E\big[f(m,n),g(m,n)\big]$$

$$\phi_{fg}(m,n) = \sum_{k=-\infty}^{k=\infty} \sum_{l=-\infty}^{l=\infty} f(k,l)g(k+m,l+n)$$

In the literature, the cross-correlation is often normalised to obtain values between 0 and 1, but in this context only relative correlation levels within the investigated interrogation area are of interest.

A high cross-correlation value is observed, where many particles match up with their corresponding spatially shifted partners, and small cross-correlation peaks may be observed when individual particles match up with other particles. The former is known as true correlation, while the latter is called random correlation. Seeding particles entering or leaving the interrogation area between the recording of the first and the second image will not contribute to the true correlation since either the initial or final particle position is missing. They do, however, contribute to the random correlation, and as such decrease the signal-to-noise ratio. The highest correlation peak can safely be considered to represent the best match between the functions $f(m,n)$ and $g(m,n)$ when the number of matching particle pairs is sufficiently large. The position of the peak in the correlation plane corresponds directly to the average particle displacement within the interrogation area investigated. In practice, to efficiently compute the correlation plane, Fourier transform processing is used in PIV. A camera image may be considered as a two-dimensional signal field analogous to a one-dimensional time series. The operation can be reduced to a complex conjugate multiplication of each corresponding pair of Fourier coefficients. The resulting new set of coefficients is then inversely transformed to obtain the cross-correlation function $\phi_{fg}(m,n)$.

The Nyquist sampling criterion associated with the discrete Fourier transforms limits the maximum recoverable spatial displacement in any direction to half the window size in that direction. In reality even this displacement is often too large for the technique to work properly, since the signal-to-noise ratio in the cross-correlation decreases with increasing spatial shift. Given a window size of length N, a maximum particle displacement of N/4 is required to ensure a reasonable signal-to-noise ratio. Another important parameter influencing the signal-to-noise ratio is the number of seeding particles within each interrogation area. With a large number of seeding particles, there will be many true correlations ensuring a high signal-to-noise ratio, and in this case an average displacement exceeding N/4 may be accepted. With a relatively small number of particles within the interrogation area, the signal-to-noise ratio will decrease, and a minimum of 5 particles/region is required in the software to achieve reasonable results using the cross-correlation technique.

3.6.3 Particle Detection

With cross-correlation the correlation plane is not generally symmetrical, and there is no central peak unless the flow velocity is actually zero. In this case the entire correlation plane is scanned to find the two highest correlation peaks. For each of the peaks found in the correlation plane, a 2-D curve-fit is used to interpolate both width, height and position of the peak. Assuming that the peak can be considered a symmetrical Gaussian curve, with no baseline-offset:

$$f(x,y) = h \cdot \exp\left(-4\frac{(x - x_0)^2 + (y - y_0)^2}{w^2}\right)$$

The parameters to be estimated are position (x_0, y_0), height h and width w, where the peak-centre (x_0, y_0) represents the primary information. The width w represents the full width at the e^{-1} level (37% of peak value) The standard deviation σ is often used as width parameter for a Gaussian curve:

$$f(x,y) = h \cdot \exp\left(-\frac{x^2}{2\sigma^2}\right)$$

The standard deviation represents the half width at the level $e^{-0.5}$ level (61% of peak value), and the relation between w and σ is:

$$w = 2\sqrt{2}\sigma$$

The function can readily be separated:

$$f(x,y) = h \cdot \exp\left(-4\frac{(x-x_0)^2}{w^2}\right)\exp\left(-4\frac{(y-y_0)^2}{w^2}\right)$$

$$\frac{\partial}{\partial x}f(x,y) = h \cdot \frac{-8}{w^2}(x-x_0) \cdot f(x,y)$$

$$\frac{\partial}{\partial y}f(x,y) = h \cdot \frac{-8}{w^2}(y-y_0) \cdot f(x,y)$$

This implies that x_0 can be estimated without y_0 being known, and vice versa. The images are sampled by a CCD array, so $f(x,y)$ will be known for integer values of x and y, when the CCD's pixel separation (pixel centre to centre spacing) is used as scaling factor. We want to estimate x_0,y_0 with sub-pixel resolution, so some interpolation scheme is required. The first step is a search for local maxima, that is to find a (x_m,y_m) so that $f(x_m,y_m)$ is greater than (or equal to) each of its eight neighbours.

The next step is to find x_0 from the maximum and the two immediate neighbours. Parabolic interpolation is chosen since it is a robust technique. The Gaussian peak is approximated by a parabola by applying $exp(x) \approx 1+x$:

$$f(x,y) = h \cdot \exp\left(-4\frac{(x-x_0)^2}{w^2}\right)\exp\left(-4\frac{(y-y_0)^2}{w^2}\right)$$

$$f(x,y) \approx h \cdot \left(1 - 4\frac{(x-x_0)^2}{w^2}\right) \cdot \left(1 - 4\frac{(y-y_0)^2}{w^2}\right)$$

The interpolation in the x-direction is based on:

$$h_{ym} = h \cdot \left(1 - 4\frac{(y-y_0)^2}{w^2}\right)$$

$$A = f(x_m - 1, y_m) = h_{ym} \cdot \left(1 - 4\frac{((x_m - 1) - x_0)^2}{w^2}\right)$$

$$B = f(x_m, y_m) = h_{ym} \cdot \left(1 - 4\frac{(x_m - x_0)^2}{w^2}\right)$$

$$C = f(x_m + 1, y_m) = h_{ym} \cdot \left(1 - 4\frac{((x_m + 1) - x_0)^2}{w^2}\right)$$

From this derives:

$$x_0 - x_m = \frac{1}{2}\frac{C-A}{2B-A-C}$$

$$h_{ym} - B = \frac{1}{4}(C-A)(x_0 - x_m)$$

$$w_x^2 = \frac{8 \cdot h_{ym}}{2B-A-C}$$

An equivalent interpolation is made for the y-direction. The height h is found by adding the height corrections calculated from the x-interpolation and from the y-interpolation to the value of the centre-pixel B. The width estimate w is calculated as

$$w = \left(w_x^2 \cdot w_y^2\right)^{0.25}$$

The interpolated widths, heights and positions of the two largest peaks are sent to the PC. The position of the highest peak is assumed to represent the average particle displacement in the interrogation area, while the lower peak is assumed to represent noise. The software now compares the heights of the peaks to validate the calculated raw vector. With h_0, h_1 and h_2 representing the height of the zero-peak, the signal-peak and the noise-peak respectively, the following should be fulfilled for good quality PIV-recordings:

$$\frac{h_1}{h_0} \geq k, \quad 0.5 < k < 0.8$$

$$\frac{h_1}{h_2} \geq k, \quad 1.0 < k < 1.5$$

The calculations in the processor are performed with a resolution of 1/64 of a pixel, to avoid reducing the basic measurement accuracy, which with good quality seeding and proper camera settings should be better than 1/10 of a pixel. For any type of curve-fit to function properly, at least three data points are needed.

3.6.4 Window-Functions

The correlations are calculated using the Fast Fourier Transformation FFT. This approach gives much higher calculation speed than a direct implementation, but the method is based on the assumption that the input particle patterns are cyclic and this leads to phantom particles and phantom correlations. A particle's initial position within the interrogation area is correctly correlated with the corresponding final position, but the FFT also correlates it with phantom particles originating

from the assumed cyclic pattern. The phantom particles and the resulting phantom correlations produce so-called cyclic noise in the correlation plane, effectively reducing the signal-to-noise ratio. To decrease the influence of phantom particles a window is applied to the interrogation area. The window function manipulates the camera image grey scale values, and thus acts like an input filter to the FFT-algorithm. It is implemented as a weighting function $W(x,y)$, where the recorded intensity of each pixel in the interrogation area is multiplied with a factor between 0 and 1 depending on the pixel position within the interrogation area. The window function thus allows the suppression of particles near the edge of the interrogation area, where phantom correlations are most likely to dominate. A Gaussian window is used:

$$W(m,n) = \exp\left[-\left[\frac{1}{k}\right]^2\left(\left(\frac{2m}{M}\right)^2 + \left(\frac{2n}{N}\right)^2\right)\right]$$

where M, N is the total number of pixels along the edges of the interrogation window, m and n are the coordinates along these edges in pixels, and k determines the width of the window.

The Gaussian window multiplys the recorded intensity with a factor, depending on their radial distance to the centre of the interrogation area. Particles in the centre of the interrogation area will be multiplied with one, while particle images are attenuated as you move away from the centre, and as such contribute less to the calculation of the velocities.

3.6.5 Overlapping Interrogation Areas

Since window functions effectively do not use the information near the edges of an interrogation area, interrogation areas are overlapped. The information not used in one interrogation area will thus be used in a different interrogation area, which partly overlaps the first. Overlap applies in both the horizontal and the vertical direction. Without overlapping there is a risk of not using information near interrogation area edges due to loss-of-pairs. Near interrogation area edges it is possible, that either the initial or the final particle position will be outside the interrogation area. Thus, particles near the edges are unlikely to contribute to the velocity calculation. Overlapping interrogation areas increase the chance that all particle pairs are completely within at least one interrogation area. Processing with overlap also produce more vectors, but this does not mean an increase in the fundamental spatial resolution rather than an over-sampling of the flow field. This over-sampling produces additional vectors as suitable interpolations, which are of great help when

calculating derived quantities from the vector map. It is better for such "interpola-
tions" to have been produced by over sampling the raw camera images rather than
by an artificial interpolation process. The only drawback of overlapping interroga-
tion areas is the processing time, which will increase in proportion to the number
of vectors generated.

3.6.6 Offset of Second Correlation Area

By default the interrogation areas are located at the same position within the first
and the second camera image maps, and the resulting measurable particle displace-
ment is ±1/4 of the length of the side of the interrogation area. It is possible how-
ever to move the velocity range by offsetting the second interrogation area relative
to the first, so that the range of measurable displacements are no longer symmetric
about zero. This is done in the adaptive correlation automatically, using the first
acquired vector field as the offset for the second iterative step.

3.6.7 Adaptive Correlation

The fundamental principle of the adaptive correlation is an iterative procedure:
From an initial guessed value, an offset is introduced from the first window (the
interrogation area in the image frame from laser pulse one) to the second window.
The obtained vector is validated and is used as a new estimate for the window off-
set. A new run is made, but this time with a smaller interrogation area. The main
benefit derived from using the shifted window is capturing the particle images that
left the interrogation area during the time between the two light pulses.

Capturing more particle images for each vector permits the interrogation area to
be refined while still obtaining an adequate number of successful vectors without
increasing the seeding density in the flow. Using adaptive correlation helps in two
ways. First, the signal strength is raised due to the capture of the in-plane dropout.
Secondly, a refinement of the interrogation area is possible because an adaptive
window offset may be applied, again producing a successful signal.

3.6.8 Dynamic Range and Spatial Resolution

The dynamic range in a PIV measurement may be defined as mean velocity
divided by the accuracy of the measurement. Based on a pixel displacement level,
it is the displacement divided by the sub-pixel accuracy. For a recording using
32x32pixel interrogation areas, the displacement is typically 8pixels. This corre-
sponds to a displacement where the time between the two light pulses is chosen so

the displacement is approximately 25% of the interrogation area. The sub-pixel accuracy is a function of many parameters, most of which are beyond the PIV system itself and therefore often unknown. As a rule-of-thumb 0.1 pixel accuracy is a realistic value for real particle seeded flows with a non-laboratory optical access. This results in a dynamic range of 8/0.1=80.

3.6.9 Zero-Velocity Biasing

In PIV there is a tendency to bias measurements towards zero. This is a problem that is worsened with increasing displacements and decreasing seeding density. The problem can be minimised by ensuring that there are always at least 5 seeding particles within each interrogation area. One of the reasons for the zero-velocity biasing is loss-of-pairs. Seeding particles, which move fast, are more likely to have their initial or final position outside the interrogation area, than particles moving slowly. As a result the slow particles will dominate the calculation of average particle displacement and effectively bias results towards zero.

Another reason for zero velocity biasing is the correlation technique itself. The general correlation theory assumes correlation areas to be of infinite size, but in reality interrogation areas are of finite size, and this makes the technique more sensitive to small displacements than large ones.

Using an offset of the second interrogation area is another way of reducing the bias. Ideally the selected offset should correspond to the average particle displacement. In this case loss-of-pairs will be minimised, since it will cancel the effect of in-plane motion, leaving out-of-plane motion as the only remaining cause for the problem. Furthermore the optimal offset will ensure that the correct particle displacement will correspond to 100% overlap between the first and the second interrogation area, which is where the correlation technique is most sensitive. If you calculate velocities as an average of several vector maps, outliers will also bias the results towards zero and artificially increase the calculated rms-values. Outliers are vectors in the vector map, which do not represent true particle displacements. They are a result of random correlations, which have drowned out the true correlation peak because in this particular interrogation area the signal-to-noise ratio is too low. Outliers tend to be longer than the true velocity vectors, but random in direction. This means that the average of several outliers will be zero, while the spread will be large, and this is why the outliers bias measurements towards zero and increase the rms-value.

3.7 Validation

Outliers are incorrect vectors resulting from noise peaks in the correlation function. They may occur in almost any PIV measurement. With FFT-processing it is important to note there will always be an outcome whether the input is meaningful or not. One conceptual difference between the FFT-processing in Particle Image Velocimetry compared to laser-Doppler anemometry is that in laser-Doppler anemometry signal conditioners are essentially used to ensure there is a meaningful input. This is possible because it is a time based measurement technique and so you can wait for the input. However, since PIV is an instantaneous measurement technique, all spatial information is sampled at the same time and there is a finite statistical probability there will be some regions where there is really no meaningful input. Therefore, it is necessary to subsequently validate the PIV vector map. Two validation methods are applied. They are

- peak height ratios

- moving average (a continuity-type method)

The purpose of validation methods is to recognize, reject and remove these outliers and possibly substitute other vectors instead of the rejected vectors. The reason for removing the outliers is that they might seriously bias the subsequent analysis of the measurement, e.g. statistical analysis as shown by Høst-Madsen et.al. [59]. Substituting a rejected vector with another might appear as some kind of trickery; however, the substitution is not necessarily an arbitrary process. The substituted vector is estimated from the surrounding measured vectors. Thus, the substitution of the rejected vectors is similar to removing noise from a signal by filtering it. The reason to substitute rejected vectors is largely because many subsequent calculation methods require a vector in every point but also for the visual appearance.

3.7.1 Peak Validation

Peak-height validation validates or rejects individual vectors based on the values of the peak heights in the correlation plane where the vector displacement was measured. The highest and the second highest peak in the correlation plane are detected. The more particles match, the more certain a velocity will be and the higher the measured correlation peak will be. The minimum allowed ratio between the highest peak and the second highest peak is defined by:

$$\frac{highest \quad peak}{second \quad highest \quad peak} \geq k$$

This assumes the measured peak is a signal and the second highest peak is merely noise and the signal should exceed the noise. Thus, if the signal-to-noise ratio is less than a certain threshold the vector is rejected. This criterion is know as the detectability criterion see, e.g., Keane at al. [63]. In this reference it is found that a good value for the detectability criterion is 1.2.

3.7.2 Moving Average Validation

Moving-average validation validates or rejects vectors based on a comparison between neighbouring vectors. The rejected vectors may be replaced by vectors estimated from surrounding values. Continuity of the flow field's behaviour is an implicit assumption in the moving-average validation method.

Moving-average validation is a special case of the general class of iterative filtered validation, described by Høst-Madsen at.al. [59]. In moving-average validation the average of the vectors in a rectangular neighbourhood of a vector is calculated and compared with the vector. Consider the vector at position (x,y). If the neighbourhood is of size (m,n), the average is calculated by the formula:

$$\bar{v}(x,y) = \frac{1}{mn} \sum_{i=x-\frac{m-1}{2}}^{i=x+\frac{m-1}{2}} \sum_{j=y-\frac{n-1}{2}}^{j=y+\frac{n-1}{2}} v(i,j)$$

The vector is the rejected if:

$$\left\| v(x,y) - \bar{v}(x,y) \right\| > k$$

where k is a variable and the norm is the usual vector distance, i.e.:

$$\left\| v(x,y) - \bar{v}(x,y) \right\| = \sqrt{\left(v(x,y)_x - \bar{v}(x,y)_x \right)^2 + \left(v(x,y)_y - \bar{v}(x,y)_y \right)^2}$$

The idea behind this approach is that the velocity field is slowly changing so that there is not too much change from a vector to its neighbour vectors. In other words, there is a correlation between neighbouring vectors, or equivalently, the vector field is essentially over-sampled. Thus, if a vector deviates too much from its neighbours, it must be an outlier. In the moving average validation calculation method the number k is not given directly. Instead some further calculations are done. First the difference:

$$\left\| v(x,y) - \bar{v}(x,y) \right\|$$

is calculated in all points *(x,y)* of the grid. The maximum:

$$\max_{x,y} \left\| v(x,y) - \bar{v}(x,y) \right\|$$

of these is found, and finally k is calculated by:

$$k = \alpha \cdot \max_{x,y} \left\| v(x,y) - \bar{v}(x,y) \right\|$$

Thus, all vectors that deviate more than a certain percentage of the maximum deviation are rejected. If the acceptance factor α is set to 1, all vectors are validated, while, if it is set to 0, all vectors are rejected. If a vector is rejected, it is replaced by the local average $\bar{v}(x, y)$ in the equation above.

The acceptance factor is not a physical parameter; it cannot be given a physical interpretation, and no natural value, related to the flow, can be given. A good choice usually is in the range 0.01–0.1. The lower the value, the more vectors will be rejected, and it should be set at least so low that all visible outliers are removed. However, as substitution is used, it is not a critical parameter. If it is set too low, so that some vectors that are actually not outliers are rejected, but the vector that substitutes them will be very close to the rejected vector. Therefore, no harm has been done.

To improve the performance of the method an iterative approach is adopted. During the first iteration the most deviating vectors are removed, during the next iteration those a little less deviating are removed and so on. For details see Høst-Madsen et.al. [59]. In general, the more iterations are used, the better the method will work, but at the expense of execution time. A number of 1 iteration together with an neighbourhood size of 3x3 vectors was found to give good results, and is used in all data processing.

3.8 Conduction of Measurements

The conduction of a measurement series consists of two main parts. First the flow parameters are adjusted with the aid of the real-time monitoring system. The 40 primary data channels (pressure, temperature, frequency and mass flow) are acquired directly from their corresponding sensors. These are written to a file together with 10 derived flow parameters. The most relevant parameters like main

flow Mach number, blowing ratio and density ratio are shown online, thus allowing their fast and accurate adjustment. The warm up of the entire system can take up to 3 hours, depending mainly on the density ratio chosen. Second, the flow velocities are measured using the PIV system. This includes a whole series of steps, starting with the set-up of the cameras and the laser, going on to the calibration and error assessment, over to the actual measurement and ends with the data processing.

The PIV system is used with two cameras at different angles to the test surface. Double pictures separated by a time step of $2.5\mu s$ are taken throughout all experiments. The field of view of a camera is around $45x36mm^2$. The corresponding displacement between the two frames of a seeding particle travelling with the free stream main flow velocity of 110m/s is close to 8pixels.

The set-up is the critical step in the PIV measurement, determining the quality and reliability of the final results. The cameras are adjusted so they look at the same area of the flow. Then they are focused and the light sheet is adjusted to be parallel to the XY-coordinates of the flow and to have a defined thickness of 1mm. The three traverse axes are adjusted to be parallel to the X, Y and Z-axis respectively.

The calibration is performed with the aid of a single layer calibration target, consisting of a flat black plate with white points. The target is placed into the test section parallel to the XY-plane. The points are arranged in a 2D array of constant spacing and have three different sizes. The difference in size defines the centre of the target and the orientation. Both cameras take pictures of that target in 5 defined distances orthogonal to the target. The PIV software detects the points and determines a linear transformation matrix for each camera. This matrix allows the transformation of the pictures taken in the respective orientation of each camera into the flow coordinate system. Furthermore, the two matrices allow the transformation of the two 2D-vector fields, derived from each camera, into one vector field in XY-plane with 3D-flow vectors.

In order to reduce the effect of reflection from the background 30 double frames are shot for each condition. An average pixel value of those 30 double frames is determined after the measurement. The average pixel value is subtracted from every double frame, thus eliminating the background reflection.

The final cross-correlation on every frame pair is performed with 32x32pixel interrogation windows to obtain a vector field. Further features used in the correlation are 50% overlap of the areas, a 1-step iterative refinement of the interrogation area with deforming windows, high accuracy sub-pixel refinement and a peak validation with a ratio between the minimum peak height and the peak 2 of 1.1. A local moving average validation over 3x3 vectors with an acceptance factor of 0.1 is

chosen as local neighbourhood validation. A Gaussian weighing function is applied to each interrogation area to deal with the particles at the border of the interrogation area. A detailed description of the options used can be found in the software manual [24].

The mean vector field over all 30 samples is determined for each camera in the next step. The 3D conversion is done with the two mean vector fields, thus giving a 2D plane in XY-orientation with averaged 3D velocity information.

The flow field is scanned in the Z-direction in increments between 1 and 3mm. All resulting planes are combined in a flow volume containing the 3 component flow vectors as well as a number of derivatives like flow angle, vorticity and shear stress. The flow volume consists of 10 to 12 planes with 79x63 vectors, giving a total number of roughly 50'000 to 60'000 data points.

The conduction of unsteady measurements is very similar to the one of steady measurements. The set-up, the correlation, averaging and post processing are the same, as is the scanning of the flow volume. The difference is in the triggering of the PIV system. This is now done with an external trigger signal originating from the pulsator. At a fixed time after the trigger signal the first frame is taken, while this time interval can be adjusted with an accuracy of $0.01\mu s$. The pulsation is scanned at different time intervals, to finally cover one entire cycle. The pulsation cycle is resolved in 12 steps.

3.9 Error analysis

The accuracy of the velocity measurement technique is established in two parts. First an experiment is conducted that allows the estimation of the accuracy of the measurement chain from the light scattered by the seeding particles to the ready processed 3D-vector field. This includes errors due to optics, calibration, correlation and validation. The fact that the seeding particles are of finite size and have a significantly higher density than the fluid leads to additional errors in the measurement of accelerated flow. The effects of vortical acceleration and of fluctuations of the flow are considered in the second part of the error analysis.

3.9.1 Measurement Chain

Establishing the accuracy of the measurement chain from raw picture to a 3D-vector field is done with the aid a simple experiment. Sandpaper is placed onto the test surface and lit in a diffuse way. That way the sandpaper appears to the cameras as a

field of seeding particles. The cameras are then traversed relative to the sandpaper over 1mm while taking the double picture. The timing is set by hand to $10\mu s$ between the two frames, thus creating a virtual velocity of 100m/s in one direction and 0m/s in the two other directions.

The resulting deviation relative to the imposed virtual velocity is presented in the following sample figure for all three velocity components. Traversing is performed in the Z-direction, creating a virtual velocity of $U=0m/s$, $V=0m/s$, $W=100m/s$. It is visible that the W-deviation is biased towards positive values, while the other two components deviate around zero. This bias is attributed to the accuracy of the traverse system and not present during measurements.
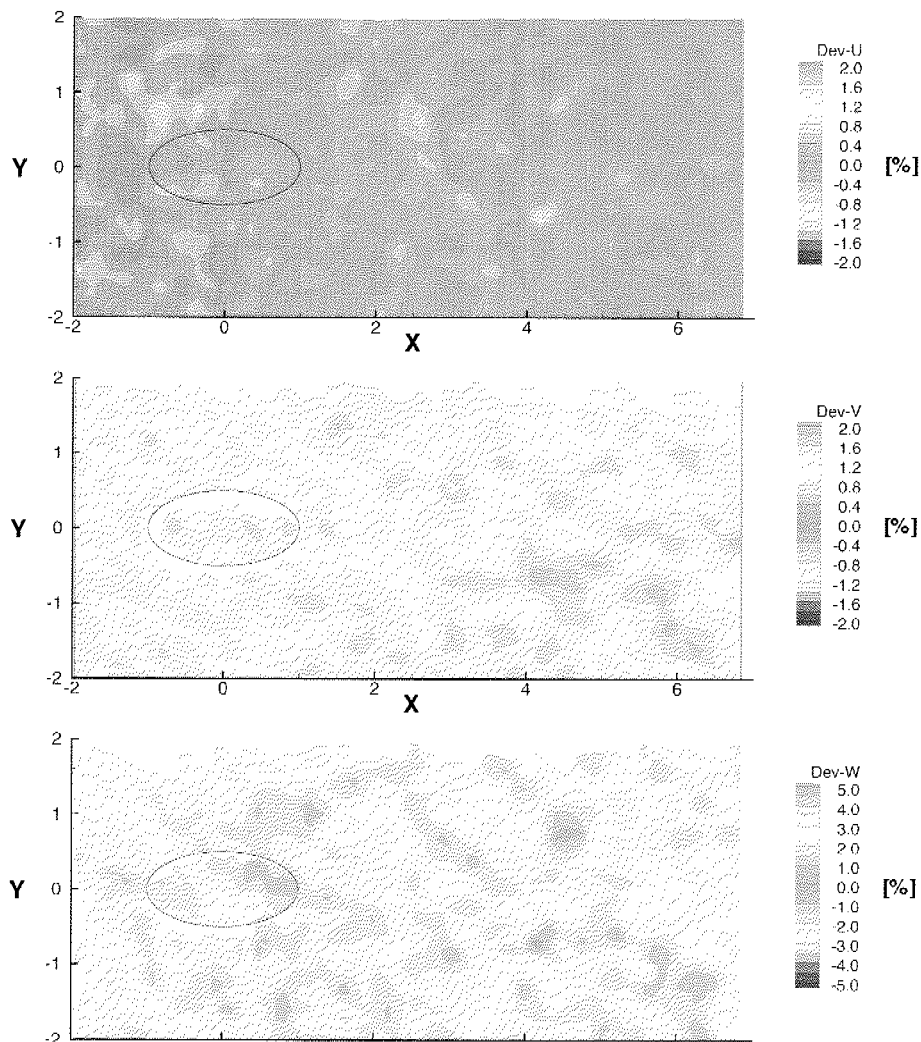
Figure 3.15: deviation of PIV-system

81

The deviation changes only slightly when the traversing direction is in the in-plane direction X, creating a virtual velocity field with $U=100m/s$, $V=0m/s$, $W=0m/s$. There is no accurate traversing possibility in Y direction. The results are not expected to be different to the ones of traversing in X direction, as no conceptual difference either in calibration, correlation, validation or any other part of the PIV processing chain is present between X and Y direction.

As expected [24], the deviation of the U and V velocity component is smaller than for the out-of plane component W. The accuracy of each component relative to the virtual freestream velocity is stated in the following Table 3.1 together with the absolute error.

Table 3.1: accuracy of PIV-system

component	relative accuracy [%]	absolute error [m/s]
U	1.2	1.2
V	1.5	1.5
W	2.3	2.3

3.9.2 Tracking Behaviour of Seeding Particles

The total accuracy of the velocity measurement is influenced by further aspects. The slip between particles and flow due to the difference in density and the finite particle size results in a difference between the flow velocity and the measured particle velocity if the flow is accelerated. The major accelerations present are due to the vortical movement in the kidney vortices and the periodic pulsation of the cooling flow.

Particle behaviour in a vortex structure

Seeding particles of higher density than the fluid are difficult to feed into high intensity vortices as centrifugal forces drive them outwards. A lack of particles occurs in the vortex core. The outwards drift can be estimated for the case of a forced vortex with zero radial fluid velocity in which particles obeying Stokes' drag law have reached the tangential fluid velocity. The tangential velocity of a solid body rotation will be calculated as the product of angular velocity ω and the distance from the core R:

$$V_t = \omega R$$

Equating the Stokes' force and the centrifugal force leads to a formula for the radial velocity V_r:

$$R\frac{1}{6}\pi\omega^2\rho_p d_p^3 = \underbrace{3\pi\mu d_p V_r}_{\substack{Stokes' \\ force}}$$
$$\underbrace{\qquad\qquad}_{\substack{centrifugal \\ force}}$$

which can be rewritten as:

$$V_r = \frac{R\omega^2 d_p^2 \rho_p}{18\mu}$$

The ratio of V_r and V_t is given by:

$$\frac{V_r}{V_t} = \frac{\omega d_p^2 \rho_p}{18\mu}$$

The dependency between the radial movement of a 3.5μm DEHS particle suspended in 20°C warm air and angular velocity of the vortical structure is linear and illustrated for completeness in Fig. 3.16.
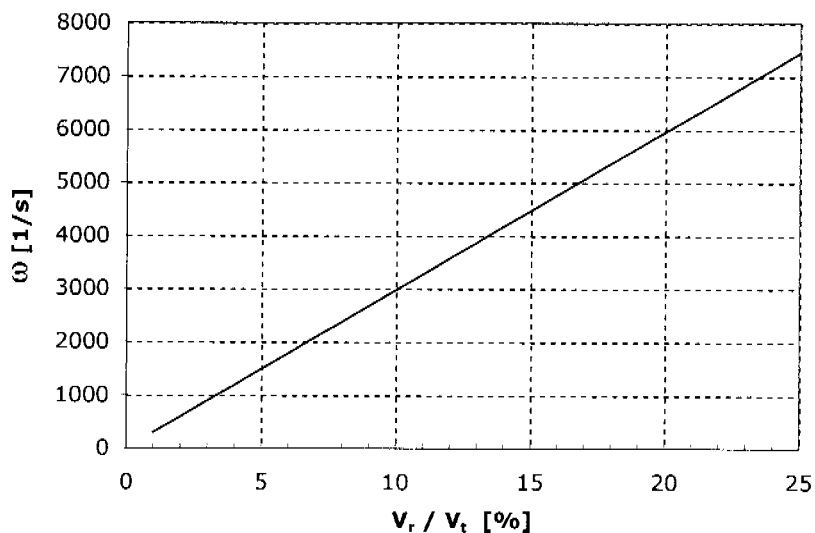
Figure 3.16: angular velocity of vortical structure as a function of radial velocity allowed

The estimation of the absolute error due to vortical movement requires information about the angular and about the tangential velocity. The greatest non-dimensional streamwise vorticity observed is in the order of ω_x =1.2, which is equivalent to ω_x =2400 1/s. Now Fig. 3.16 allows the extraction of the ratio between radial and tangential velocity, which in this case is about 8%. The peak tangential velocity is in the order of 60 m/s, resulting in a maximum expected error of 4.8m/s.

Particle behaviour in a turbulent flow

If external forces can be neglected, the tracking capability of suspended particles is influenced only by the particle shape, particle diameter d_p, particle density ρ_p, fluid density ρ_f and fluid dynamic viscosity η or kinematic viscosity ν. Furthermore, a spherical particle shape, low particle concentration of less than 10^{10}particles/m^3, which represents an infinite fluid and a high density ratio of particle and fluid is assumed. For an optimal PIV application 15 particles per interrogation volume (Interrogation area and light sheet thickness >1mm^3) are required according to Adrian [6]. This concentration of 1μm particles results in a suspension with a mean distance between the single particles of 500 diameters.

The following equation describes the unsteady motion of a suspended sphere. Basset [11] derived this equation of motion for a sphere relative to an infinite, stagnant fluid already in 1888, and in 1959 Hinze [56] expanded this to a moving fluid, considering the instantaneous velocity $V=U_p-U_f$ of the particle relative to the fluid:

$$\underbrace{\frac{\pi}{6}d_p^3\rho_p\frac{dU_p}{dt}}_{\substack{accelerating \\ force}} = \underbrace{-3\pi\mu d_p V}_{\substack{Stokes' \\ viscous \\ drag}} + \underbrace{\frac{\pi}{6}d_p^3\rho_f\frac{dU_f}{dt}}_{\substack{pressure \\ gradient \\ force \\ on \\ fluid}} - \underbrace{\frac{\pi}{12}d_p^3\rho_f\frac{dV}{dt}}_{\substack{fluid \\ resistance \\ to \\ accelerating \\ sphere}} - \underbrace{\frac{3}{2}d_p^2\sqrt{\pi\mu\rho_f}\int_{t_0}^{t}\frac{dV}{d\xi}\frac{d\xi}{\sqrt{t-\xi}}}_{\substack{dragforce \\ associated \\ with \\ unsteady \\ motion}}$$

U characterises the instantaneous velocity of the sphere or of the fluid, subscript p refers to the seeding particle, and subscript f refers to the fluid. The first term in this equation represents the force required to accelerate the particle, and the second term describe the viscous drag as given by Stokes law. Acceleration of the fluid produces a pressure gradient in the vicinity of the particle, and hence an additional force on the particle as described by the third term. The fourth term is the resistance of an inviscid fluid to acceleration of the sphere, and is predicted by potential flow theory. This term is equivalent to the fluid mass which is displaced by the accelerating sphere. The last term is the *Basset history integral* which defines the resistance caused by the unsteadiness of the flow field. Note that when the first, third and fourth terms are combined, the accelerating force is equivalent to that of a sphere whose mass is increased by an additional *virtual mass* equal to half the mass of the displaced fluid.

In the first part of this section the particle motion in turbulent flow, based on Melling [85], will be considered followed by consideration of the particle behaviour in a vortex structure, according to Melling et.al [86].

For the case of particle motion in turbulent gas flows the last three terms on the right side can be neglected due to the high density ratio between particle and fluid.

84

The viscous term (Stokes' drag law) dominates due to the small particle Reynolds number $Re_p \ll 1$, defined as:

$$Re_p = \frac{\left(U_p - U_f\right)d_p}{\nu}$$

Now the unsteady motion of a suspended sphere can be expressed as:

$$\frac{dU_p}{dt} = -C\left(U_p - U_f\right)$$

After an algebraic transformation and an implementation of the Stokes number, the non dimensional frequency of the particle response, the expression C can be rewritten and renamed as the characteristic frequency of the particle:

$$C = \frac{18\mu}{\rho_p d_p^2} = \frac{18\omega_c}{S_K^2 \cdot s}$$

with the angular frequency:

$$\omega_c = 2\pi f_c$$

the Stokes Number:

$$S_K = \left(\frac{\omega_c}{\nu}\right)^{\frac{1}{2}} d_p$$

and the particle density ratio:

$$s = \frac{\rho_p}{\rho_f}$$

Here, ω_c is the angular frequency of the fluctuations of the flow to be observed and f_c is the corresponding frequency. This experiment is not aimed at the quantification of turbulence but on the quantification of the pulsating cooling jet. Pulsating frequencies are in the range of f_c=50-250Hz.

The occurring turbulent frequency can be estimated with the Kolmogorov time scale, but for most flows of practical interest it is not quantifiable with any precision. Estimated by experiment ω_c lies in the range of f_c=1-10kHz

An analytical solution of the equation above gives an expression for the particle response in unsteady flow, which characterizes the fluctuation energies of the time-averaged particle and fluid motion. The criterion for specifying the maximal size of a seeding particle is defined as follows. It is determined from the amplitude ratio of the particle and the fluid velocities, which is set to a minimal value of 0.99, accord-

ing to Melling [85]:

$$\frac{\overline{u_p^2}}{\overline{u_f^2}} = \left(1 + \frac{\omega_c}{C}\right)^{-1} \geq 0.875$$

Fig. 3.17. shows the graphical expression of this equation for DEHS with a density of 0.914g/cm^3 for the lower and upper turbulence frequencies. The particles are suspended in air at 20°C and 1bar. A strong dependency of the tracking capabilities on the particle diameter is obvious.
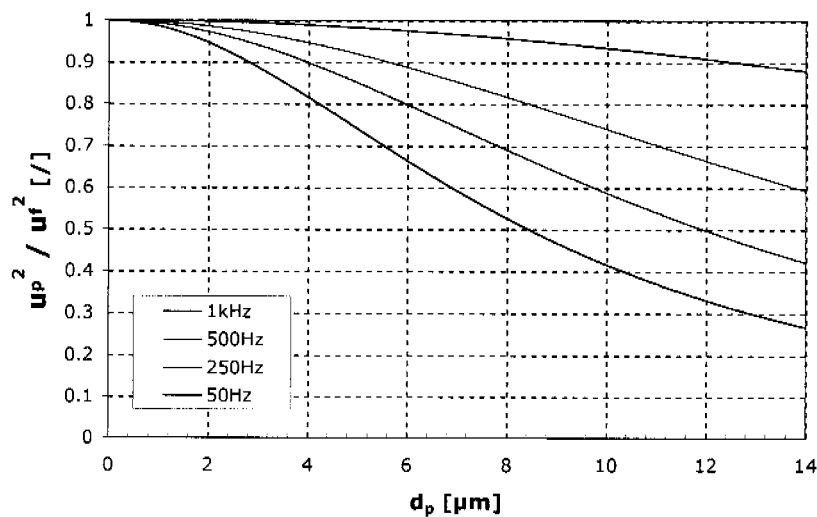
Figure 3.17: relation between tracking capability and particle diameter for DEHS

The tracking capability for particles of 3.5μm is very good for the occurring pulsating frequencies of 50Hz and 250Hz, as can be seen in the figure above. The tracking capability of these particles for the turbulent frequencies of 1kHz and above are not ideal. Smaller particles would resolve those better. The impact on the overall accuracy of the PIV system is discussed at the end of this chapter in the error analysis.

The estimation of the absolute error due to fluctuations in the flow is done with above figure, the known mean particle size (3.5μm), the observed peak velocity of 140m/s and the maximum frequency of pulsation of the coolant (250Hz). The relative error of 98% corresponds to an absolute deviation of 2.8m/s.

3.9.3 Total Measurement Accuracy

The total accuracy of the velocity measurement technique is summarized in the following Table 3.2.

Table 3.2: total accuracy of velocity measurement

source	absolute error [m/s]
measurement chain	2.1
tracking of vortical structure	4.8
tracking of fluctuations	2.8
total	**5.9**

It should be considered that the error of the measurement chain and of the tracking behaviour of flow fluctuations are of random nature while the tracking of vortical structures is a systematic error. The stated total error is the worst case, where the out of plane velocity component W measured in the presence of strong vorticity, high tangential velocity and fast flow fluctuation.

4. FLOW STRUCTURE

This chapter presents the results of the measurements and discusses the major find-ings regarding the near hole film cooling flow structure. First the flow conditions under which the measurements were conducted are defined and summarized in Section 4.1. The flow derivatives used in the following analysis are defined and dis-cussed in Section 4.2, followed by a detailed section about the trajectory of the cooling jet.

The phase resolved flow behaviour of pulsating coolant injection is analysed in Section 4.5. The velocity field and the centre line trajectory of the cooling jet are utilized to reach the conclusion that the near hole flow field behaves in a quasi steady manner.

The fundamental vortical structure of near hole film cooling is revealed in the next Section 4.6. Kidney and Horseshoe-vortices are detected and quantified.

The entrainment of low momentum fluid into the centre of the kidney vortex pair is quantified in Section 4.7. The expected impact on the cooling performance is discussed.

4.1 Flow Conditions

The flow conditions under which the measurements were conducted are described by a set of non-dimensional parameters. These are the displacement thickness δ^*, the momentum thickness θ and the shape factor H for the main flow boundary condition, the main flow Mach number M, the density ratio DR, the blowing ratio BR, the momentum ratio IR, the axial hole angle α and the reduced frequency f_r. Their respective definition and error are given in Chapter 2.6.

The velocity measurement technique is described in detail in Chapter 3, together with its accuracy. The raw results are 3D velocity vectors in a volume

extending from $-2d$ to $+6.5d$ in the axial direction X, $-2d$ to $+2d$ in the lateral direction Y and $0.2d$ to $2d$ in the normal direction to the surface Z. The velocity in the layer on the surface at $Z=0d$ is set to zero, which is considered accurate except for the area occupied by the hole. The respective spatial resolution in the XYZ volume is $77x62x14$. The unsteady measurements have a lower resolution of 9 points in the Z direction. The graphical representation uses linear interpolation between the discrete data points. This is considered a good approximation except for the boundary layer between $Z=0d$ and $Z=0.2d$.

The measurements are grouped in two fundamentally different sets of measurements, those with steady and those with pulsating cooling injection. Further variations were made in axial hole angle α, density ratio DR, blowing ratio BR and reduced frequency f_r. The influence of the boundary layer condition, the main flow Mach number and the lateral injection angle β are not quantified yet. All measurements were taken with an approximate free stream Mach number of $M=0.3$. An overview of the different measurements is given in the following Table 4.1.

Table 4.1: flow condition in the experiments

case	α	M	BR	DR	IR	f_r
1	30°	0.30	0.99	1.02	0.97	0
2	30°	0.30	0.99	1.53	0.65	0
3	30°	0.30	2.00	1.07	3.76	0
4	30°	0.30	2.04	1.66	2.51	0
5	30°	0.30	2.69	1.12	6.50	0
6	30°	0.30	2.69	1.73	4.19	0
7	50°	0.30	1.00	1.01	1.00	0
8	50°	0.30	2.00	1.06	3.78	0
9	50°	0.30	1.00	1.48	0.68	0
10	50°	0.31	2.01	1.60	2.56	0
11	30°	0.30	1.00	1.01	1.01	0.38
12	30°	0.30	2.00	1.06	3.78	0.38
13	30°	0.30	1.98	1.05	3.74	1.88
14	50°	0.30	1.00	1.01	1.00	1.88

All parameters presented in the following analysis are non-dimensionalized. The velocities are non-dimensionalized with the respective free-stream velocity U_f and all length scales are non-dimensionalized with the hole diameter d. All derived parameters are based on non-dimensional values.

4.2 Flow Derivatives

4.2.1 Vorticity

The vorticity has three components, the axial or streamwise ω_x, the lateral or crosswise ω_Y and the normal vorticity ω_z. The axial vorticity describes the rotational strength of the fluid around the streamwise axis X at one point. Similarly, the lateral vorticity describes the rotational strength around an axis Y crosswise to the main flow direction and parallel to the surface and the normal vorticity around an axis normal to the surface Z. Their respective definition is given as:

axial / streamwise vorticity

$$\omega_x = \frac{\partial W}{\partial Y} - \frac{\partial V}{\partial Z}$$

lateral / crosswise vorticity

$$\omega_Y = \frac{\partial U}{\partial Z} - \frac{\partial W}{\partial X}$$

normal vorticity

$$\omega_z = \frac{\partial V}{\partial X} - \frac{\partial U}{\partial Y}$$

Non-dimensional parameters are used in the calculation of the vorticity, resulting in non-dimensional vorticity components. The vorticity components are derived at every point in the flow field with central 2 point differences and added to the data set. The relative accuracy of the vorticity is 5.9%.

4.2.2 Circulation

The circulation that is used in the following section compactly expresses the vortical information contained in the flow data. The axial circulation Γ_x of the coolant jet is calculated as a function of the axial coordinate X. In general the circulation of a vortex is expressed as the line integral of the velocity vector along a closed loop around this vortex:

$$\Gamma = \oint \vec{v} \cdot d\vec{r}$$

This can be expressed as the integral of the vorticity vector over the area vector according to Stokes Theorem. The area contains the vortex of interest:

$$\Gamma = \oiint \vec{\omega} \cdot d\vec{A}$$

This is the form used to derive the circulation Γ from the vector field. The vorticity component normal on the area vector is integrated over the area. Since the circulation as a function of X is investigated, the area of integration is the YZ-plane. The vorticity component to be integrated is the streamwise vorticity ω_x. The equation applied to the data set now takes the form:

$$\Gamma_X = \oiint \vec{\omega}_X \cdot d\vec{A}_{YZ} = \oiint \left(\frac{\partial W}{\partial Y} - \frac{\partial V}{\partial Z} \right) \cdot d\vec{A}_{YZ}$$

The vortex of interest is the kidney vortex of the coolant jet. The sides of the kidney shape have opposite sign of vorticity. Deriving the circulation for the entire kidney vortex should result in the value 0, given that the boundary layer does not contribute to the streamwise vorticity and the noise in the velocity field is isotropic.

The circulation used in the following sections is derived from the left hand side (looking in streamwise direction) of the kidney vortex only, to gain information about dissipation of the vortical strength. The integration in Y-direction is performed from the centre of the cooling hole at $Y=0$ to the symmetry plane between the two holes at $Y=2$. The integration in Z-direction is done over the full range of available data, from $Z=0$ to $Z=2.4$. The right hand side should ideally give the same result with opposite sign. Fig. 4.1 sketches the area of integration. The circulation is determined with an accuracy of 6.1%.
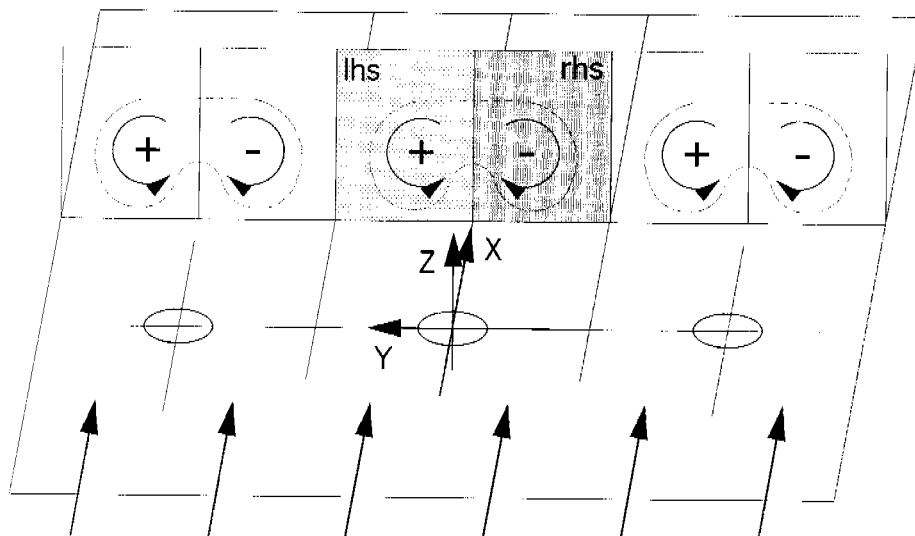
Figure 4.1: illustration of area of circulation

Typical plots of the entire kidney vortex, the left-hand-side and the right-hand-side for the circulation as a function of X are given in Fig. 4.2.
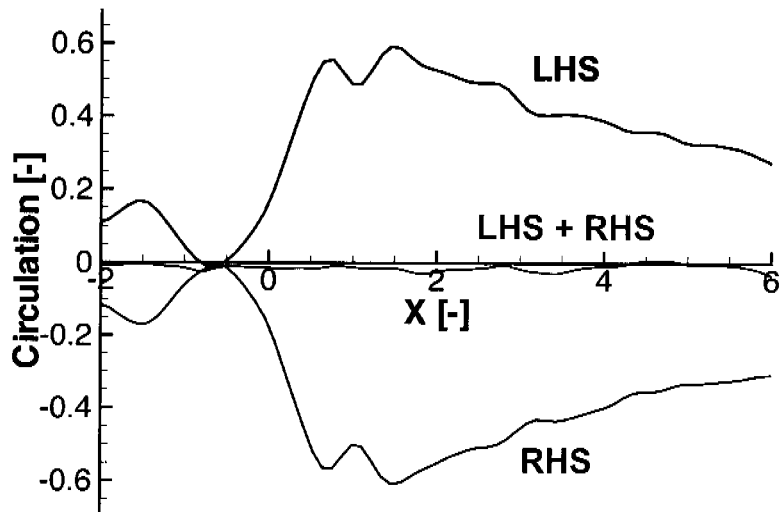
Figure 4.2: typical circulation of kidney vortex

The plot above confirms the theoretical considerations from before. Both sides have similar shaped circulation, mirrored at the zero-axis. Circulation of the entire kidney vortex is about zero, indicating that the boundary layer does not contribute to the streamwise circulation and that the noise is isotropic.

Furthermore, Kelvin's Theorem [47] for the change of circulation of an inviscid flow with conservative body forces applies for a closed loop C around both kidney vortices:

$$\frac{D\Gamma}{Dt} = -\oint_C \frac{\nabla p}{\rho} dl = 0$$

This means, that viscous and buoyancy forces are not of relevance for streamwise flow phenomena but only momentum forces.

4.2.3 Unsteady Blowing Ratio

The unsteady behaviour of the blowing ratio BR is estimated with the measured pressure variation in the plenum between pulsator and cooling holes and the assumption of a constant discharge coefficient in the cooling holes, as described in Section 2.6.2.7. The pressure variation inside this plenum is mainly dependent on the frequency, as is shown in the following Fig. 4.3.

This approach has a number of limitations. The variation is based on pressure measurements in the pulsator plenum which is upstream of the cooling holes. The discharge coefficient is assumed to be constant and pressure and expansion waves are visible in the $f_r=1.88$ curve. The volume of interest inside the test section is expected to experience attenuation of the waveform due to dissipation, damping and variable discharge coefficient.
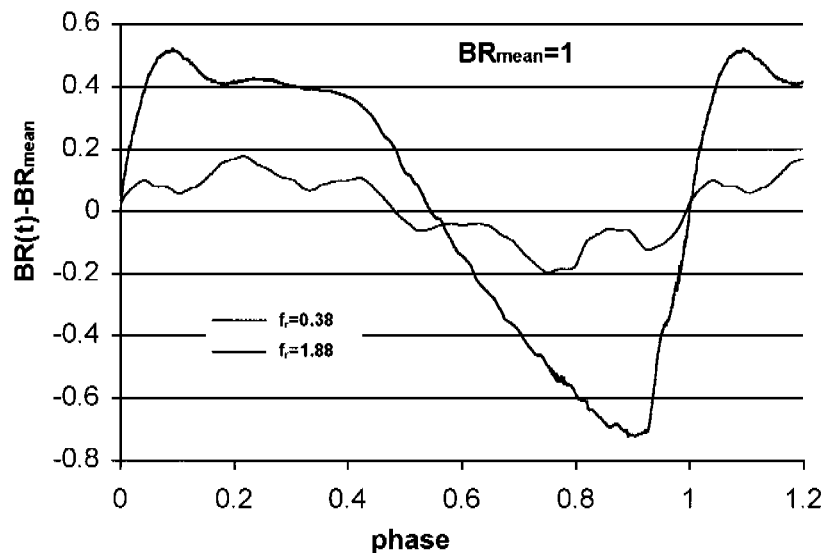
Figure 4.3: blowing ratio variation based on pressure measurement

The measured flow field is used to check the validity of the approach taken in Chapter 2.6.2.7. A control volume is placed over one cooling hole, extending from $2d$ upstream to $6d$ downstream and $1.8d$ in each lateral direction from the origin of the coordinate system (see Fig. 4.4).
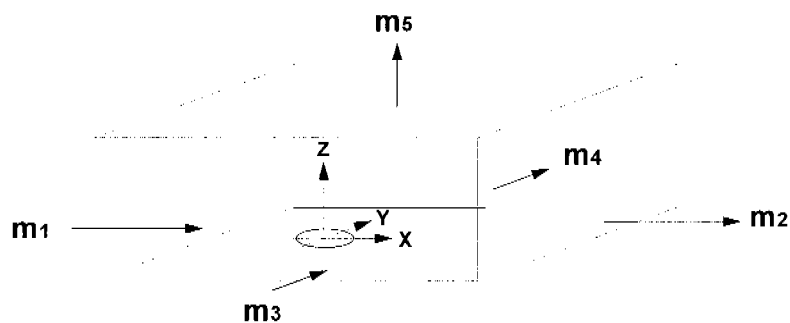
Figure 4.4: control volume for blowing ratio calculation

The respective mass flux is integrated over each side of this control volume, except the bottom one, where the velocity is set to zero. The cooling mass flow rate can be derived assuming that the flow through the upstream YZ area contains main flow only and that the mass flow through the other four faces is the sum of cooling flow and main flow:

$$\dot{m}_c = \dot{m}_2 - \dot{m}_3 + \dot{m}_4 + \dot{m}_5 - \dot{m}_1$$

The result is compared to the previous approach in the following two figures. The trigger signal is displayed as a reference. First the variation of the blowing ratio for a pulsating frequency of f_r=0.38 is shown in Fig. 4.5 followed by the comparison for f_r=1.88 in Fig. 4.6.
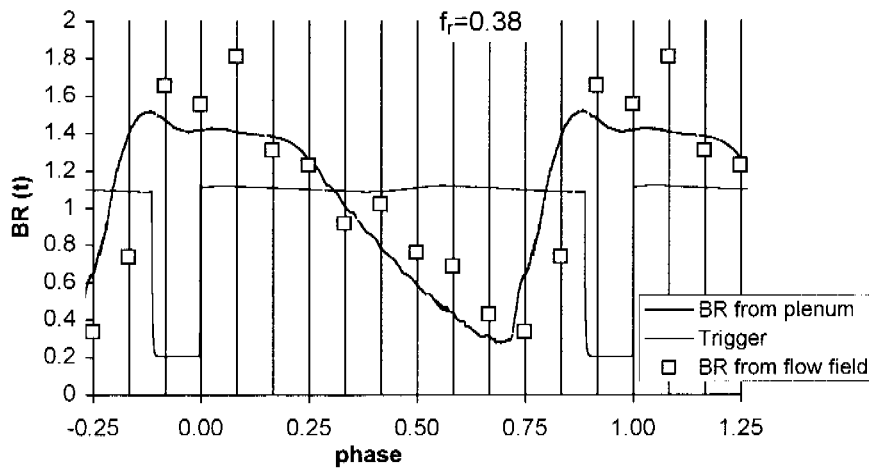
Figure 4.5: comparison of blowing ratio variation for f_r=0.38 pulsation

The figures Fig. 4.5 and Fig. 4.6 show several aspects. A time delay between BR based on pressure and the one derived from the flow field is visible, in particular for f_r=0.38. In this case the peaks and drops are even accentuated, which is unexpected.

The pressure and expansion waves observed at f_r=1.88 seem to be damped out. However, the resolution of the phase in 12 steps is too low to capture these fluctuations reliably. In this case the general BR level drops by almost 10%. Also no clear timeshift can be identified.
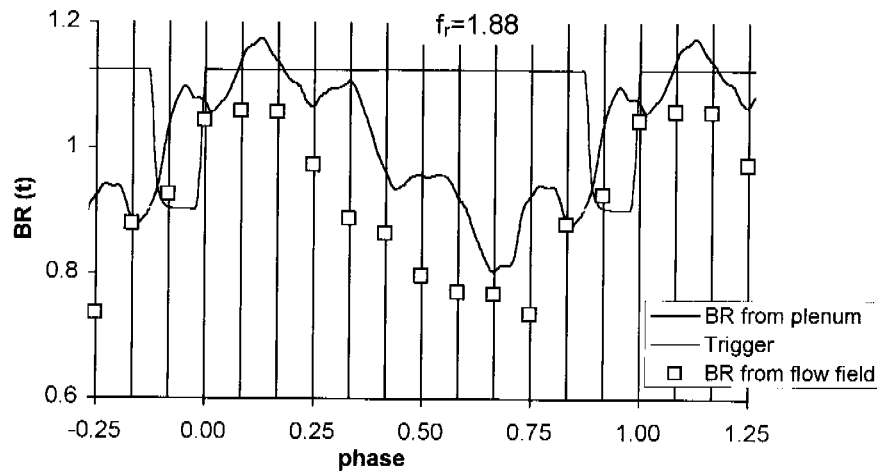
Figure 4.6: comparison of blowing ratio variation for f_r=1.88 pulsation

To check the influence of the downstream extent of the control volume a second, smaller control volume is placed over the hole. This volume spans from $-2d$ to $2d$ in streamwise direction X and from $-1.5d$ to $1.5d$ in lateral direction Y.
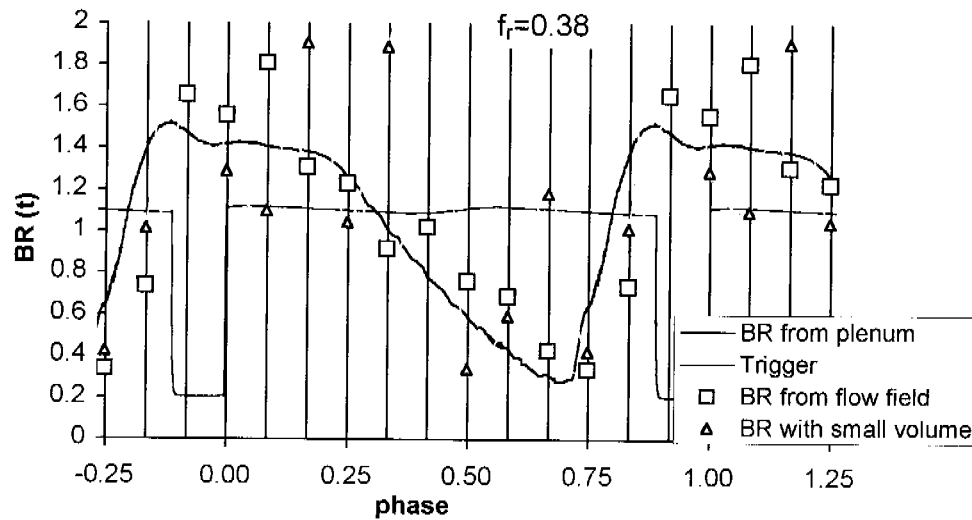
Figure 4.7: pulsating blowing ratio from small control volume for f_r=0.38

In this case with a pulsation frequency of f_r=0.38 the result shows very strong noise and no identifiable waveform.

In the f_r=1.88 case, which is known to have better seeding quality and less reflection in the raw images, the smaller volume shows no phase shift (see Fig. 4.8). A different offset to the mean level is observed, the general waveform, however, is quite similar to the one with the larger control volume.
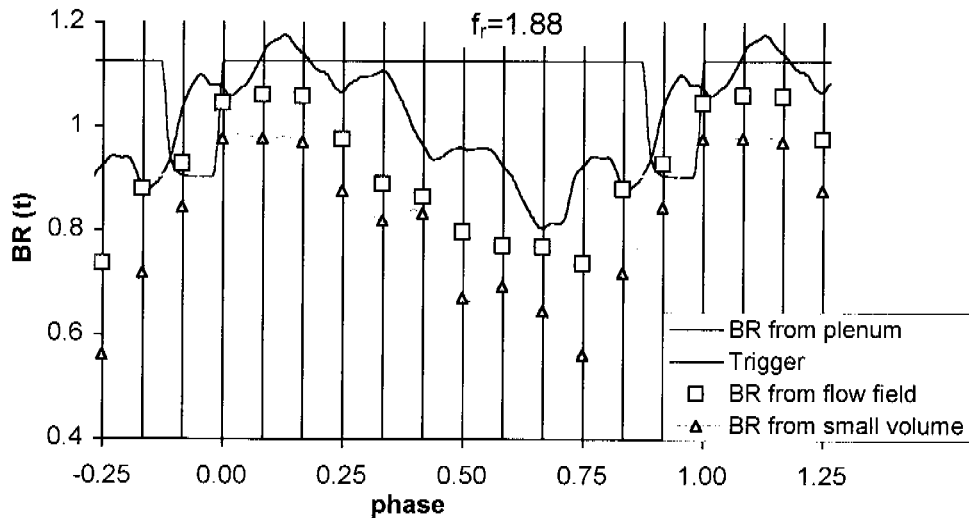
Figure 4.8: pulsating blowing ratio from small control volume for f_r=1.88

It can be concluded, that the match between the blowing ratio derived from the flow field and the one based on unsteady pressure measurements in the pulsator plenum is good. The general waveform is repeated; the mean level of the pressure-based prediction is higher than the one based on the flow field, the absolute offset for both frequencies is in the order of 0.1.

The f_r=0.38 case experiences a strong peak in blowing ratio. The f_r=1.88 case experiences attenuation of the multiple peaks and troughs. Since the data density is low, under-sampling is possible.

A general phase shift of about 1/12 of the period is observed for f_r=0.38, and a little less for f_r=1.88. This phase shift is not dependent on the streamwise extent of the control volume, therefore it is not due to convecting flow features in the control volume. This phase shift is also not expected to be due to convection between pressure measurement device and flow domain, as the phase shift in the f_r=1.88 case would be five times bigger as the one in the f_r=0.38 case.

There are two pieces of evidence, which suggest that the flow through the film holes is frequency dependent. Firstly the BR from the flow field is about 5% higher for f_r=0.38 and about 10% lower for f_r=1.88 than the respective average BR. Sec-

ondly the phase relationship between the pressure and the *BR* from the flow changes. The flow lags the pressure at f_r=0.38 and is in phase at f_r=1.88. This phase lag is not due to convection time as tested by changing the size of the control volume. A change of phase between excitation and response classically indicates proximity to resonance. So both the phase data and the amplitude data suggest that there is an unsteady effect of frequency on the discharge coefficient.

Evidence appears to point to more unsteady effects at f_r=0.38 than at f_r=1.88. Probably this is due to the greater amplitude at f_r=0.38.

4.3 Sample of Flow Structure

This section presents the general flow structure related to a single film cooling jet interacting with the main flow. An illustration of the measured near hole region is shown in Fig. 4.9. Case 8 is used for this illustration, where the cooling flow is injected via a hole with 50° streamwise angle. The momentum flux ratio *IR* is 3.78 with a density ratio *DR* at unity. The colour indicates the magnitude of the axial velocity. Velocity vectors are included at the three axial planes at *X*=-1, 2 and 4.

The main flow enters the volume from the left side. The velocity profile at X=-1, which is 0.23d upstream of the leading edge of the hole, shows the influence of the blockage of the jet. The boundary layer thickness is increased towards the centre of the jet.
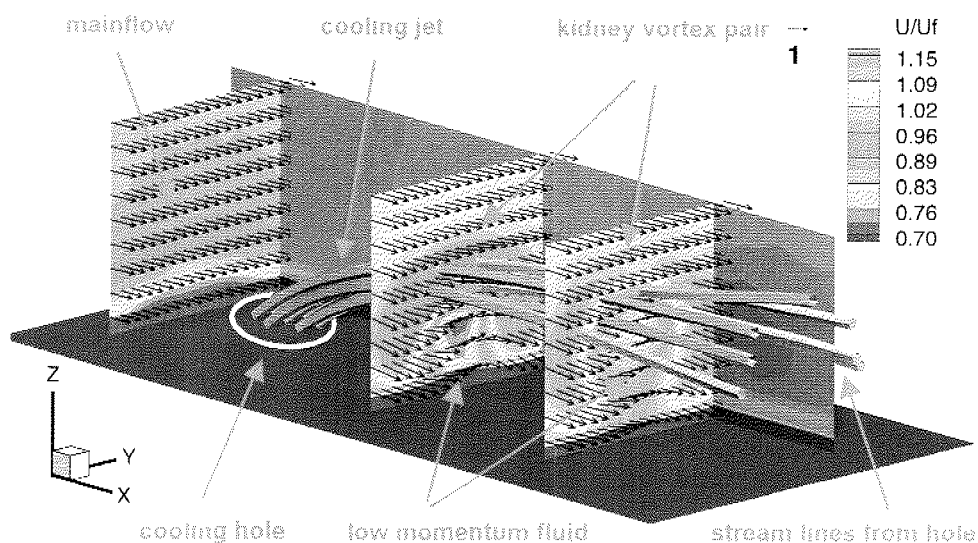
Figure 4.9: example for flow structure associated with film cooling

The cooling jet is indicated by 7 stream lines emerging from the hole. The centre line stays in the centre, which indicates a laterally symmetric flow. The kidney vortex pair is indicated by the high velocity region in the two axial cuts at X=2 and 4. The vectors in these planes show the typical counter-rotating pattern. The size of the vortical region increases with axial distance from the hole, while their strength decreases.

A region of low momentum fluid is visible close to the surface in the centreline of the cooling jet. It originates from the boundary layer and grows with axial distance from the hole.

4.4 Trajectory

First the way the jet trajectory is defined and extracted from the measured data is presented together with the necessary assumptions. The main assumption of axial flow angle at the point of emergence is validated in the next step. Two established trajectory models are introduced and compared to the measured data. Their respective accuracy is determined. Then a new empirical correlation for the near hole trajectory of a film cooling jet is presented. This correlation is validated with a measurement not used in determining its coefficients.

4.4.1 Definition

The centre line jet trajectory is defined by the streamline emerging from the centre of the cooling hole. This definition allows an easy comparison with different sets of measured data or numerical results. It has to be stated, though, that this definition does not reflect the trajectory of the geometrical centre of the jet and the disturbance it introduces into the main flow. The streamline will gradually move to the windward side of the jet, mainly due to the entrainment on the leeward side of the jet attributed to the kidney vortex pair.

Streamlines are inserted into the flow volume of each measurement case with the post processing tool Tecplot. The streamline path is integrated in three dimensions within the 3-D volume field in the flow direction with four steps between two data points. The injection site has to be at the lowest plane where measurements were taken, at $Z=0.2$. The streamline might not exit the boundary layer if it is inserted below that level as the velocity on the wall (at $Z=0$) is set to zero. This is done also in the region of the hole due to the lack of data in this region. The veloc-

ity between $Z=0$ and $Z=0.2$ is determined with linear interpolation.

The starting point of the streamline in lateral direction is in the centre of the hole at $Y=0$. The axial starting point X_{start} is determined from the streamwise hole angle α and the distance between the wall and the start of the stream line in vertical direction $Z_{start}=0.2$ as:

$$X_{start} = Z_{start} \cot \alpha$$

This is assuming that the jet emerges from the centre of the hole with the streamwise hole angle and that the flow does not get deflected between $Z=0$ and $Z=0.2$.

This assumption has been validated. The curvature of the streamline in the near hole region is investigated. The streamline would display a strong discontinuity in its curvature at $Z=0.2$ if this assumption is not correct. A slight discontinuity, however, is expected, as the region of initial curvature of the jet trajectory is approximated as a straight line. The discontinuity would be strongest for a steep injection angle and a low blowing ratio. This case of $\alpha=50°$ and $BR=1$ is shown in Fig. 4.10.
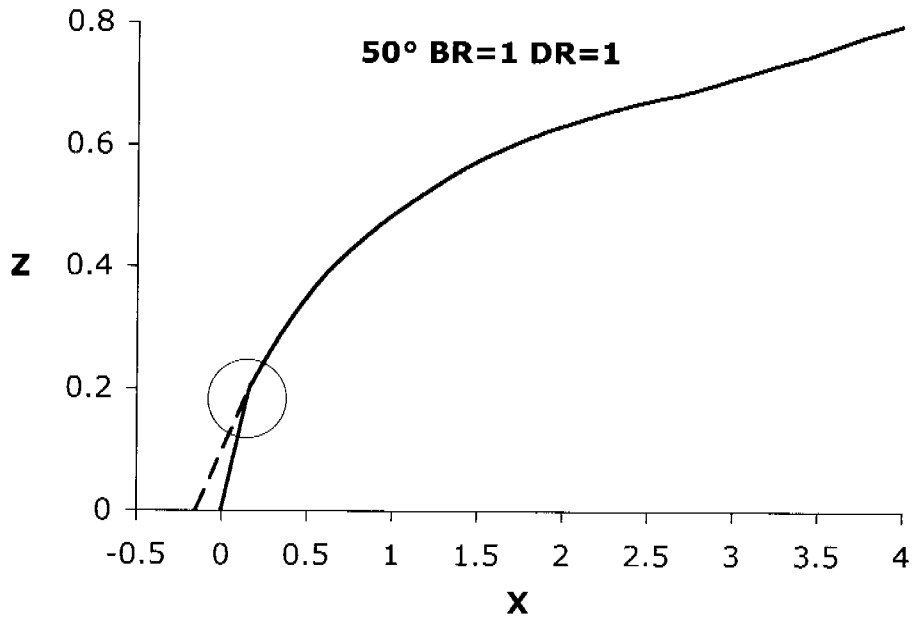
Figure 4.10: near hole centre-line trajectory of $50°$, $BR=1$

The trajectory, as defined in this chapter, is displayed by the black solid line. The green circle indicates the point where the discontinuity in the curvature occurs due

to above assumption. The discontinuity is visible. The tangent to the measured trajectory (above $Z=0.2$) is extended to the wall with a dashed red line (at $Z=0$) to estimate the error introduced by the assumption. The error refers to the axial point of emergence. The expected real point of emergence will be somewhere in between the two extremes shown in Fig. 4.10, as the real jet will be deflected to some degree. Therefore the error will be less than the case of the red line, which is $0.15d$ or 11% of the axial hole extent. This error, which presents the worst possible case, is considered to be acceptable for the further analysis.

A case with higher blowing ratio is analysed in the next Fig. 4.11 to validate the assumption that low blowing ratio will produce the greatest error.
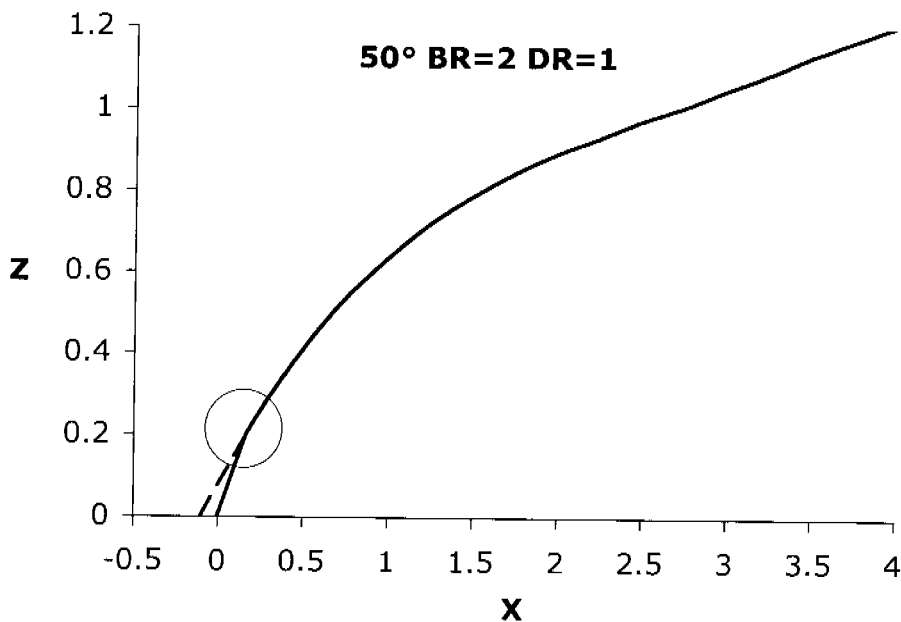
Figure 4.11: near hole centre-line trajectory of 50°, BR=2

Again, the black solid line displays the trajectory, the green circle indicates the point of discontinuity in the curvature and the tangent to the measured trajectory between $Z=0$ and $Z=0.2$ is shown by the red dashed line.

As expected, the error is smaller for higher blowing ratio. In this particular case it is better than $0.09d$ or 7%, the error associated with the red dashed line.

The effect of the axial start point of the stream line on the trajectory is analysed to round up this discussion. For this purpose a case with low blowing ratio $BR=1$

and stream-wise hole angle $\alpha=30°$ is looked at. Two additional streamlines are inserted, starting $0.5d$ upstream and $0.5d$ downstream respectively.

30° BR=1 DR=1
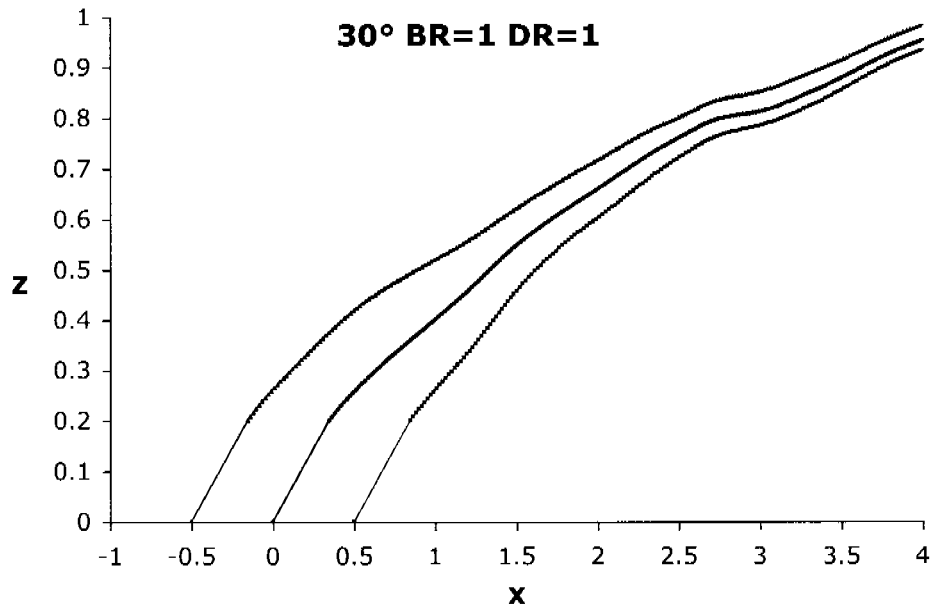
Figure 4.12: off-axial trajectories, $30°$, BR=1

Both streamlines converge towards the centre streamline. At $X=4d$ they are less than $1d$ apart. It also has to be noted, that the streamlines do not move in lateral direction with any significance, the flow behaves symmetrical around the lateral centre.

This finding supports the statement that the error introduced is acceptable in the further discussion.

4.4.2 Trajectory Models

Two established trajectory models are presented here. First is the basic model of Shandorov [99], which is a simple empirical model for the axis of a jet in cross-flow, based on experiments with air jets from a circular nozzle discharging in a cross-flow:

$$X = \frac{1}{IR} \cdot Z^{2.55} + Z\left(1 + \frac{1}{IR}\right)\cot\alpha$$

with the non-dimensional coordinates of the jet axis X and Z, the stream-wise injection angle α and the jet momentum ratio IR.

101

It is stated that the equation is valid over the following range of *IR* and α:

$$2 \leq IR \leq 22; \quad 45° \leq \alpha \leq 90°$$

A selection of three measured trajectories is plotted against the model in the following Fig. 4.13.
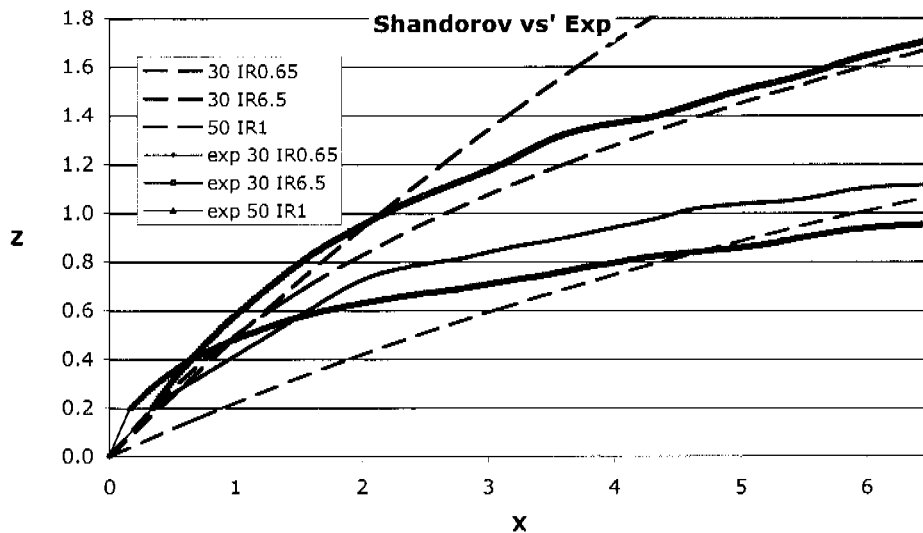
Figure 4.13: comparison between Shandorov's model and experimental data

The experimental data is represented by the solid lines, the model by the dashed lines and corresponding flow conditions use the same colour. The measured data is not matched too well. The curvature is not reflected by the model and it tends to over-predict the vertical position of the jet centre except for low momentum ratio *IR* within the first 6*d*. However, as stated before, the cases displayed here are not within the range of the measurements that were performed by Shandorov. Furthermore, the definition of the trajectory used by Shandorov is vague.

One big difference is the presence of a wall in the film cooling research, while Shandorov had a jet in unconfined space. The wall would have the effect of lowering the pressure, thus keeping the jets closer to the wall and inducing a stronger curvature into the trajectory, as observed in above figure.

Abramovich [4] developed a semi-analytical model that was recently used by Burdet [19] and Burdet et.al. [18] in his film cooling model.

$$Z = \sqrt{39k} \cdot \ln\left[\frac{10 + X + \sqrt{X^2 + 20X + 7k \cdot \cot^2 \alpha}}{10 + \sqrt{7k}\cot \alpha}\right]$$

where the coefficient k is dependent on the momentum flux ratio IR and the stream-wise injection angle α:

$$k = \frac{\pi \cdot IR \cdot \sin \alpha}{4C_n}$$

The factor C_n was determined by Abramovich from experiments and takes the value of $C_n = 3$. The comparison between the model of Abramovich and the measured data is shown in the following Fig. 4.14.
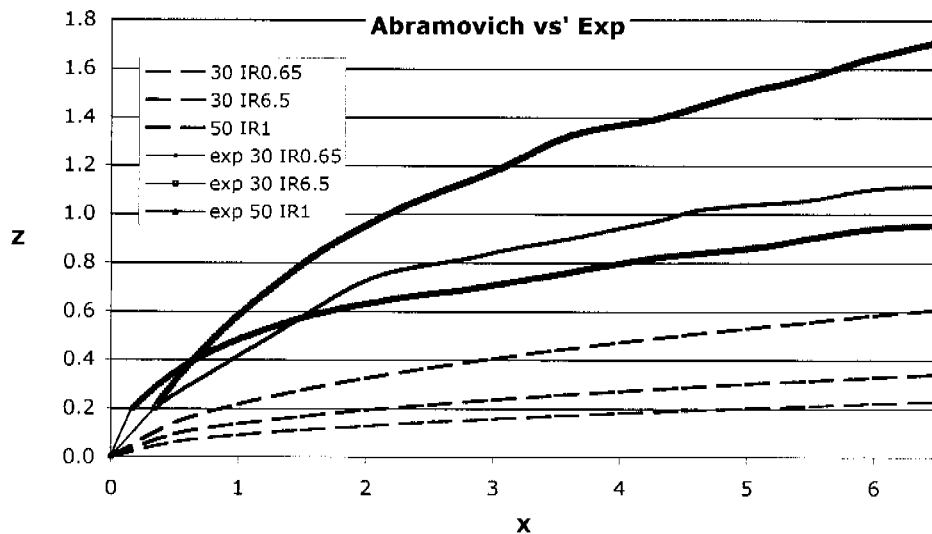
Figure 4.14: comparison between Abramovich's model and experimental data

The model strongly under-predicts the trajectory. This can be attributed to the fact that the model of Abramovich seems to describe the trajectory of the centre of the kidney vortices, and not of the streamline that emerges from the centre of the hole. Again, the definition of the actual line that is modelled is vague.

4.4.3 Empirical Near Hole Trajectory Correlation

The previous two comparisons show that the near hole trajectory defined with a streamline is not matched well with established models. It seems appropriate to

create an empirical correlation based on the measured steady cases to facilitate further analysis based on the trajectory.

A power function is used to match each of the 10 trajectories. The dependency on IR of the trajectory is modelled with another power function. The end result is a fit for each stream-wise injection angle with 6 coefficients, that describe the near hole trajectory with high accuracy.

A fit like this offers the opportunity of quick validation of numerical data, as the measurements are compressed in one equation.

About 200 different mathematical functions were tried in order to find the best fit of the measured results. The trajectories of the 10 steady film cooling measurements are matched well with a Langmuir-power function:

$$Z = \frac{a \cdot b \cdot X^{1-c}}{1 + b \cdot X^{1-c}}$$

and the three respective coefficients are matched with a simple power-fit as function of the momentum flux ratio:

$$a = a_1 \cdot IR^{a_2}$$

$$b = b_1 \cdot IR^{b_2}$$

$$c = c_1 \cdot IR^{c_2}$$

The centre-line-trajectory is described with above equations and 6 coefficients for each of the stream-wise injection angles. The resulting maximum standard deviation between the correlation and the measured data is $0.03d$ with a maximum discrepancy of $0.13d$. The respective coefficients are summarized in the following Table 4.2:

Table 4.2: trajectory correlation coefficients

	a1	a2	b1	b2	c1	c2
30°	1.768	0.291	0.352	-0.251	0.042	0.647
50°	1.727	0.498	0.350	-0.305	0.405	-0.417

The dependency of the trajectory on the stream-wise injection angle is not trivial, as can be seen in the Fig. 4.13 and Fig. 4.14. Inter- or even extra-polation between the two measured angles is not expected to result in highly accurate information.

The comparison between the measured data and the new correlation is illustrated in Fig. 4.15.
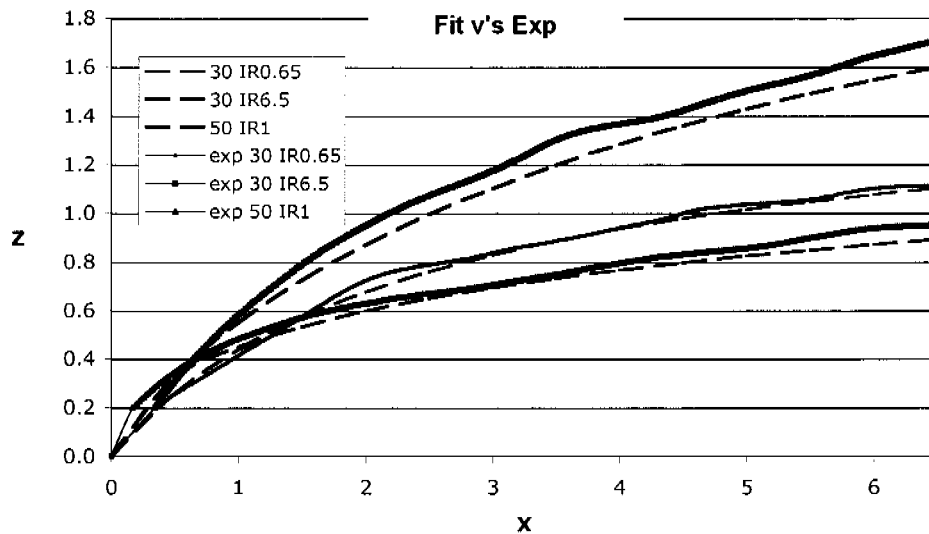
Figure 4.15: comparison between new correlation and experimental data

This selection of flow conditions shows that the match is good for low momentum flux ratios, irrespective of density ratio and the streamwise injection angle. The highest measured momentum flux ratio of *IR=6.5* shows the biggest discrepancy with a general underprediction of the trajectory of about 7%. The general curvature is reproduced well and at *X=1* all trajectories are almost identical with the correlation.

4.4.4 Validation of New Correlation

The trajectory of a measurement not included in the general analysis is utilized to gain further confidence in the newly established fit. This data-set was not used to obtain the coefficients and thus will show the generality of the correlation. The flow conditions of this case are *α =30°*, *BR=2.02*, *DR=1.32* and *IR=3.07*. The comparison between this data-set and the correlation is shown in Fig. 4.16.
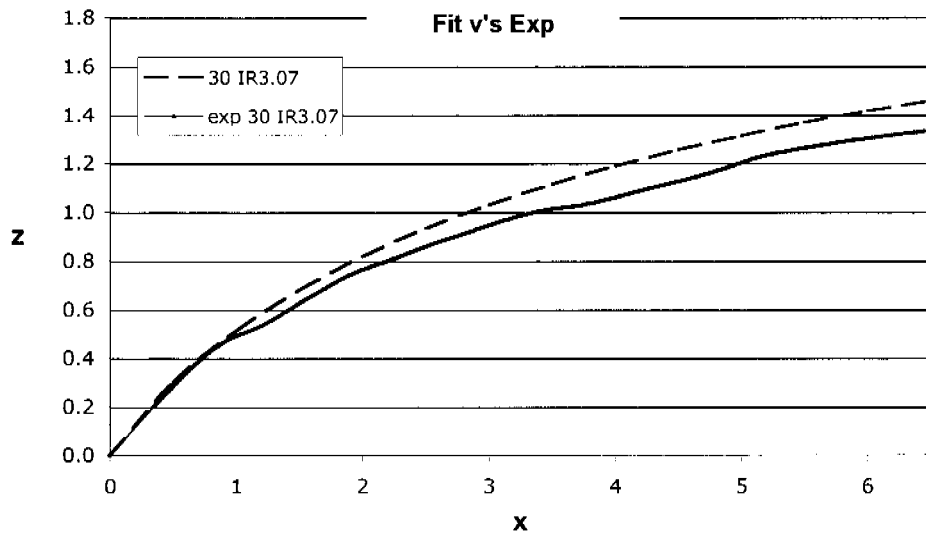
Figure 4.16: comparison between new correlation and steady experimental data

This comparison shows the general character of the correlation. The fit shows about 7% over-prediction of the height of the trajectory, which is within the accuracy of the correlation. Between $X=0$ and $X=1$ the correlation fits the data almost perfectly.

4.5 Quasi Steady Coolant Pulsation

The periodic pulsation of the cooling jet does have a visible influence on the flow-field, as illustrated in Fig. 4.17. This sample shows the phase resolved case 11 as iso-velocity contours. This illustration indicates that periodic jet-lift off and reattachment is taking place. Phases 1 to 5 have a slightly detached jet, indicated by an almost undisturbed low-velocity plane ($U<U_f$ in light green) downstream of the hole. Phases 6 to 12 show some disturbance of the low velocity plane in the jet centre. This indicates an attached jet.
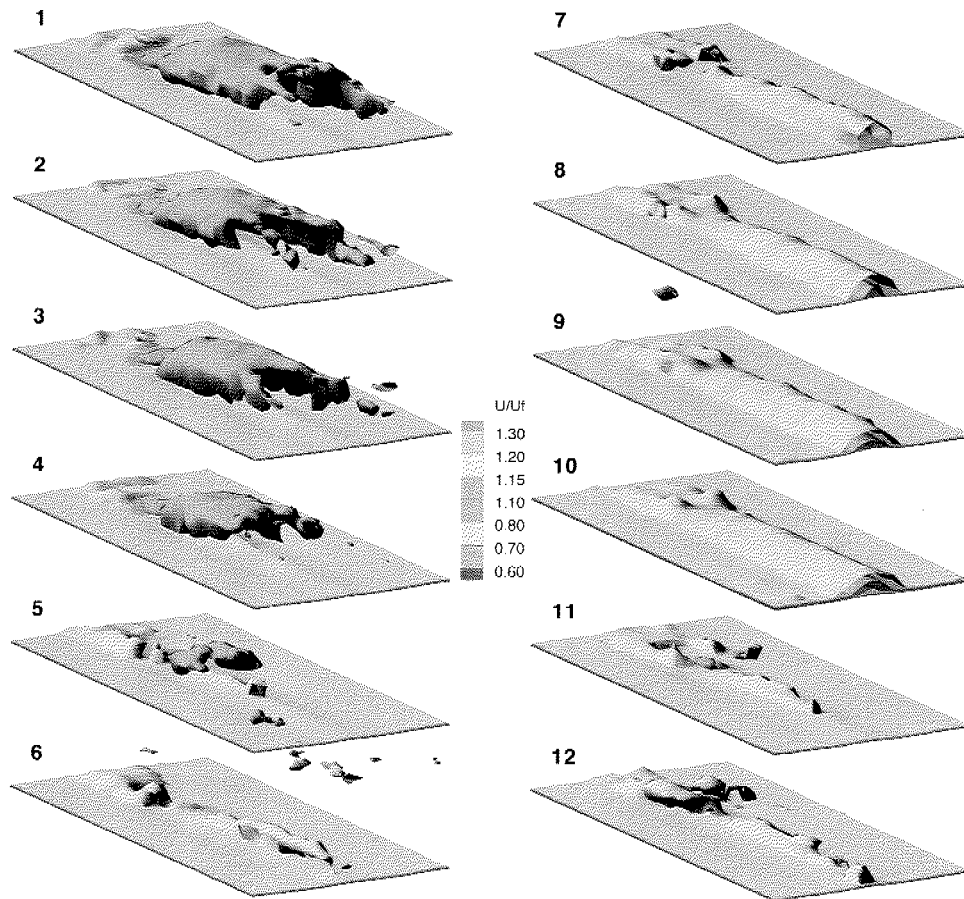
Figure 4.17: time resolved iso-velocity contour case 10 (*30° f_r=0.38, BR=1*)

The unsteady behaviour of the near hole interaction between cooling jet and mainflow is of great importance for the modelling of unsteady film cooling. The modelling is greatly facilitated if it is possible to model periodic changes in blowing ratio with a quasi steady approach. Each part of the periodic phase can then be modelled with the steady flow condition that corresponds to the momentary blowing ratio, which is easily obtained in a CFD calculation. The modelling would gain complexity if strong unsteady effects are present and have to be taken into account.

It is hypothesized that the near hole flow field behaves in a quasi steady manner if it encounters a pulsating cooling flow. This hypothesis is used as one of the main assumptions in the cooling model implemented in the in house CFD code MULTI3, as described by Burdet [19].

There are different definitions of quasi steady behaviour. The flow behaves in a

quasi steady fashion when each part of the period is the same as the steady flow with corresponding BR, IR and DR. It also behaves in a quasi steady fashion when the phase averaged flow field is similar to the steady one if the averaged BR, IR and DR corresponds to the steady ones.

It is expected that the quasi steady behaviour reduces with axial distance downstream of the injection, i.e. the flow becomes unsteady. The further downstream the quasi-steadiness persists the stronger this assumption is.

Steady flow and unsteady phase resolved cases with corresponding blowing ratio are chosen based on the considerations in Chapter 4.2.3. First the flowfield in YZ planes is compared, then the trajectories and finally the axial circulation.

4.5.1 Quasi Steady Flowfield

The knowledge about the blowing ratio variation offers the opportunity to validate the thesis of a quasi steady near hole flow field.

Comparisons between different measurements are made in two different ways in the following section. A visual comparison between the respective flowfields is achieved with respective figures. The quality of this comparison is established with the correlation coefficient k, defined as:

$$k = \frac{\sum \vec{u_1} \cdot \vec{u_2}}{\sqrt{\sum |\vec{u_1}|^2 \sum |\vec{u_2}|^2}}$$

where the sum over all points in the displayed plane of vector products of two measurements is normalized by the product of the sum of normed vectors. The subscript identifies the measurement the velocity $\vec{u}$ is taken from. k can take values between 0 and 1. The lowest value 0 indicates that the vectors do not match each other at all. The highest value 1 is reached when a perfect match between two flowfields is present.

The steady flow field for case 1 is compared to the corresponding phase resolved one in the pulsation cycle of case 11 with low pulsation frequency of $f=50Hz$. The best match in blowing ratio occurs at phase 0.33 on the downward slope (see Fig. 4.5).The steady case 7 is compared to the unsteady case 14 with $f=250Hz$ at phase 0 (see Fig. 4.6), which is at the end of the positive slope.

Additionally, a comparison between the steady case 3 with $BR=2$ and the phase 0.08 in the $50Hz$ case 11 is performed, although the level of blowing ratio is about 0.2 lower.

108

First the steady case 1 with $\alpha=30°$, $BR=1$, $DR=1$ is compared to the pulsating case 11 with $\alpha=30°$, $BR=1$, $DR=1$, $f_r=0.38$ at phase $4/12$, where a blowing ratio of about 0.95 is expected (Fig. 4.18).
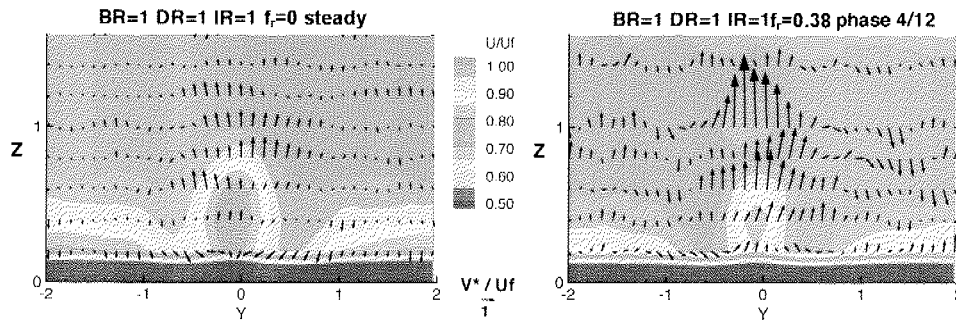
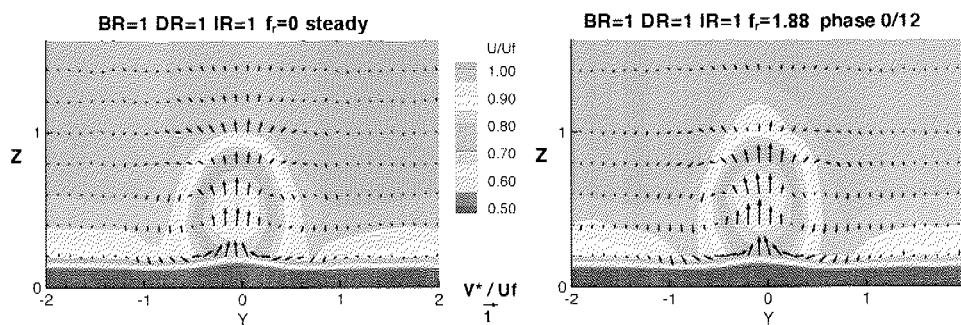**Figure 4.18**: velocity field cut at $X=4$, case 1 and case 11, phase $4/12$

The general shape as well as the magnitude of the jet differ visibly. The unsteady case has a more narrow low momentum core of the jet and a less pronounced boundary layer at both sides of the jet. It is also visible that the velocity data is rather noisy in this region of the flow volume, as was also observed when a small control volume was used to establish the blowing ratio. k takes the value of 0.33, supporting the observation of only partial correspondence of the two flow fields.

The comparison between this steady case 1 and the respective phase averaged case 11 is shown in the following Fig. 4.19:
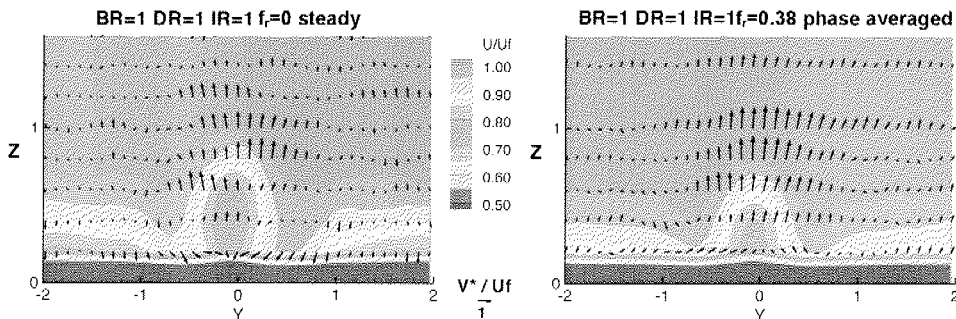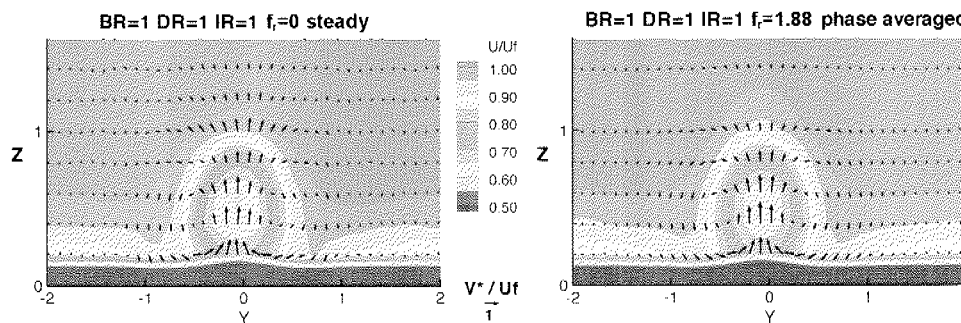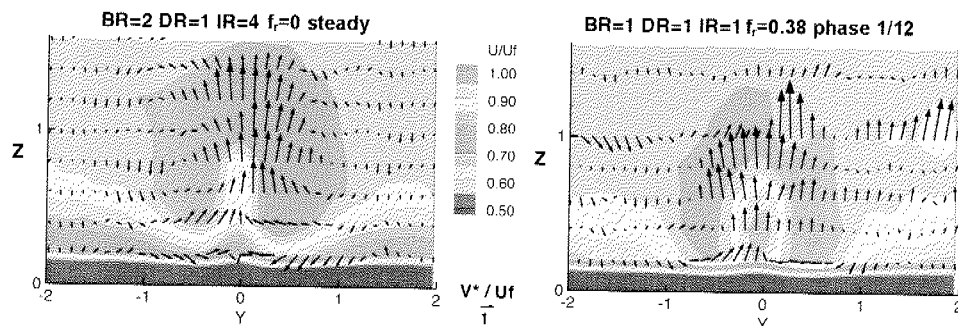

Figure 4.19: velocity field cut at $X=4$, case 1 and case 11, phase average

The two pictures compare much better than the previous ones. For one the noise in the unsteady measurement seems to be averaged out due to the 12 times higher number of samples. Also the general shape and magnitude of the jet compares bet-

ter. The unsteady case has slightly less low momentum fluid entrained into the jet and also a thinner boundary layer on both sides of the jet. This suggests that the entrainment is affected by the unsteadiness. k takes the value of 0.48, which is better than in the previous comparison. Still, the correspondence between the two flow fields is only partial.

Now the steady case 7 with $\alpha=50°$, $BR=1$, $DR=1$ is compared to the pulsating case 14 with $\alpha=50°$, $BR=1$, $DR=1$, $f_r=1.88$ at phase $0/12$, where a blowing ratio of around $BR=1$ is expected (Fig. 4.20).

Figure 4.20: velocity field cut at $X=4$, case 7 and case 14-phase 0/12

In this comparison, the general shape as well as the magnitude of the jets are very similar. The unsteady jet extends slightly higher and the drop of low momentum fluid on the outer sides of the kidney vortex pair is more pronounced. k has the value of 0.91, which supports the very good match of the two flow fields.

The comparison between this steady case and the respective phase averaged case is shown in the following Fig. 4.21:

Figure 4.21: velocity field cut at $X=4$, case 7 and case 14-phase average

In this comparison, the general shape as well as the magnitude of the jets are very similar. The unsteady jet still extends slightly higher but the dip of low momentum fluid on the outer sides of the kidney vortex pair is less pronounced than in the previous comparison. k takes the value of 0.93, indicating an even better correspondence than in the phase resolved comparison.

As a last comparison the steady case 3 with $\alpha=30°$, $BR=2$, $DR=1$ is shown with the pulsating case 11 with $\alpha=30°$, $BR=1$, $DR=1$, $f_r=0.38$ at phase $1/12$, where a momentary blowing ratio of about $BR=1.8$ is expected (Fig. 4.22).

BR=2 DR=1 IR=4 f$_r$=0 steady   BR=1 DR=1 IR=1 f$_r$=0.38 phase 1/12

Figure 4.22: velocity field cut at $X=4$, case 3 and case 11-phase 1/12

Although the blowing ratio and the momentum flux ratio are not very different the corresponding flow field clearly is. The unsteady jet is located closer to the wall, while the steady jet is lifted off. The steady jet is of greater strength and the boundary layer is thicker. The entrainment of low momentum fluid into the core of the jet is greater in the unsteady case. Additionally, the noisy data of the unsteady case makes the comparison look slightly worse. k takes the value of 0.57, indicating that the two cases do correspond only partly.

4.5.2 Quasi Steady Trajectory

Now the empirical trajectory correlation introduced in Chapter 4.4.3 is utilized to pick up the discussion about the quasi steady behaviour of the near hole flow with pulsating coolant. This is case 11 with $\alpha=30°$, $BR=1.0$, $DR=1.0$ $IR=1.0$ and $f_r=0.38$. First the trajectory of the dataset with strong pulsation amplitude is compared to the correlation. The comparison is done with both, the part of the pulsation where a blowing ratio of $BR=1$ is expected as well as with the phase average, with a mean blowing ratio of also $BR_{mean}=1$. The comparison is shown in Fig. 4.23.
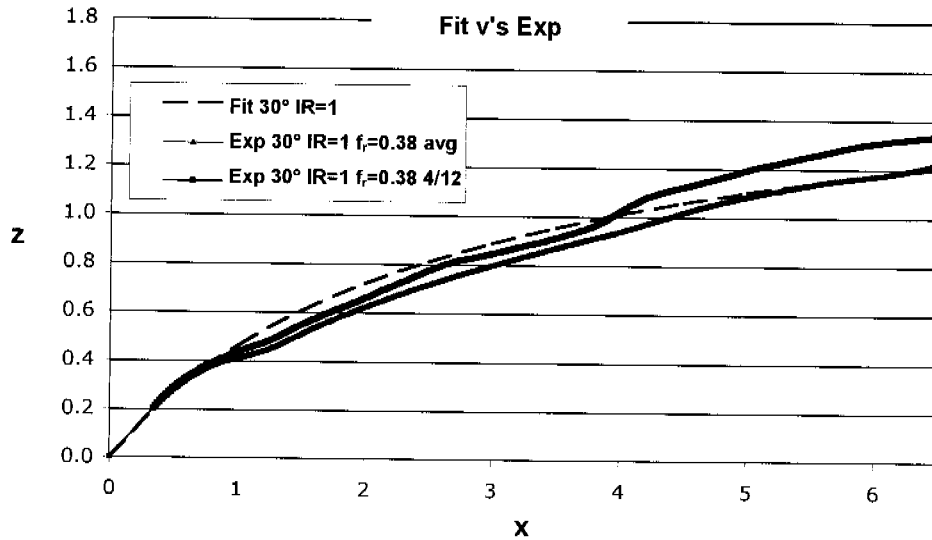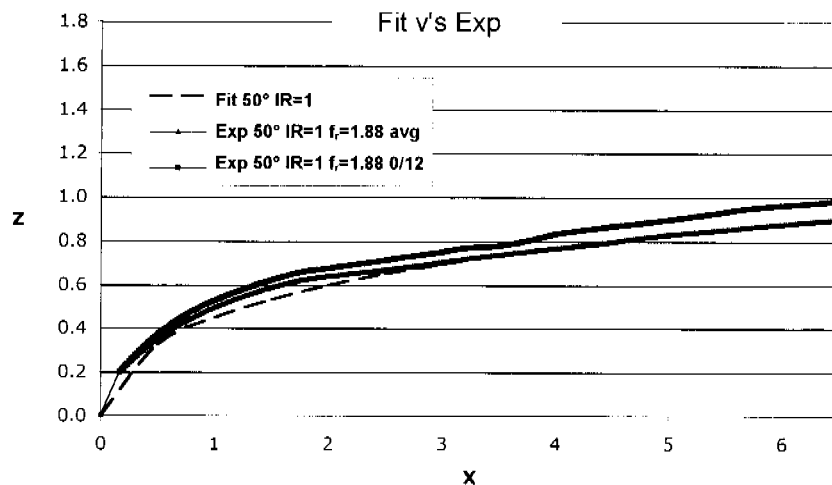
Figure 4.23: comparison between new correlation and unsteady experimental data

This comparison again shows the general character of the fit, as the match is in the order of the accuracy of the model with around 8%. Both trajectories, the phase averaged as well as the phase resolved case where a similar *BR* and *IR* as in the averaged case are expected follow similar paths. This confirms the thesis, that the near hole flow field behaves in a quasi steady manner with a pulsating cooling flow.

The trajectory of the respective phase with minimum and maximum blowing ratio is extracted to ensure the validity of above comparison. This case with low pulsating frequency is expected to have a strong variation of the trajectory, as the blowing ratio has strong variations. The trajectories are shown in Fig. 4.24.

It is clearly visible that the trajectory changes greatly over the pulsation phase. The match between the correlation and the measured trajectory is reasonably good for the high blowing part. The measured trajectory in the low blowing part falls after *X=2*. This explains partly why the elevation of the phase averaged trajectory is at a lower level than in the steady case. This effect is not captured by the correlation, and the quasi steady assumption is not true in this particular case.
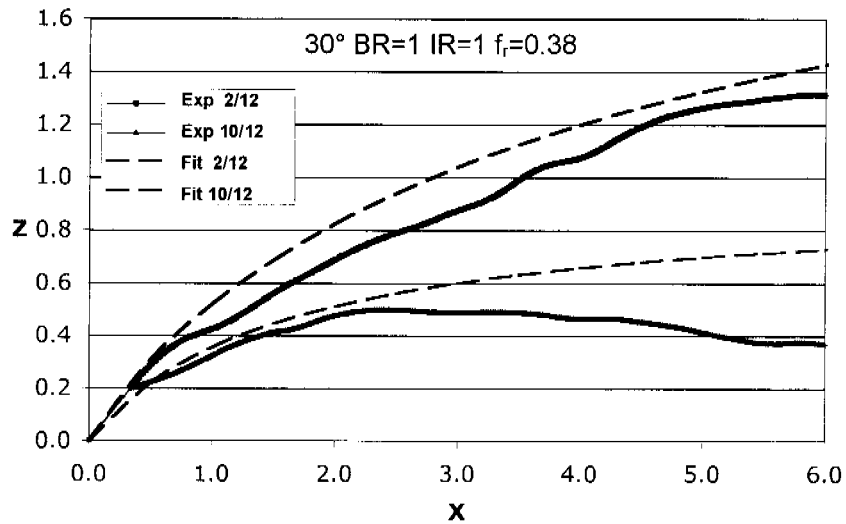
Figure 4.24: trajectory at maximum and minimum blowing ratio for $\alpha=30°$, $BR=1$, $f_r=0.38$

The comparison between the correlation and the measured trajectory is now made for the unsteady case 14 with low pulsating amplitude ($\alpha=50°$, $BR=1.0$, $DR=1.0$ $IR=1.0$ and $f_r=1.88$). The comparison again is done with part of the pulsation where a blowing ratio of $BR=1$ is expected and with the phase average, with a mean blowing ratio of also $BR_{mean}=1$. The comparison is shown in the following Fig. 4.25.

Figure 4.25: comparison between new correlation and unsteady experimental data

This comparison again shows the general character of the correlation, as the match is in the order of the accuracy of the model with around 8%. Both trajectories, the phase averaged as well as the phase resolved case where a similar *BR* and *IR* as in the averaged case are expected follow similar paths. This confirms the thesis, that the near hole flow field behaves in a quasi steady manner with a pulsating cooling flow.

The trajectory of the respective phase with minimum and maximum blowing ratio is extracted to ensure the validity of above comparison. This case with high pulsating frequency is expected to have less variation of the trajectory, as the blowing ratio little strong variations. The extracted trajectories are shown in the following Fig. 4.26.
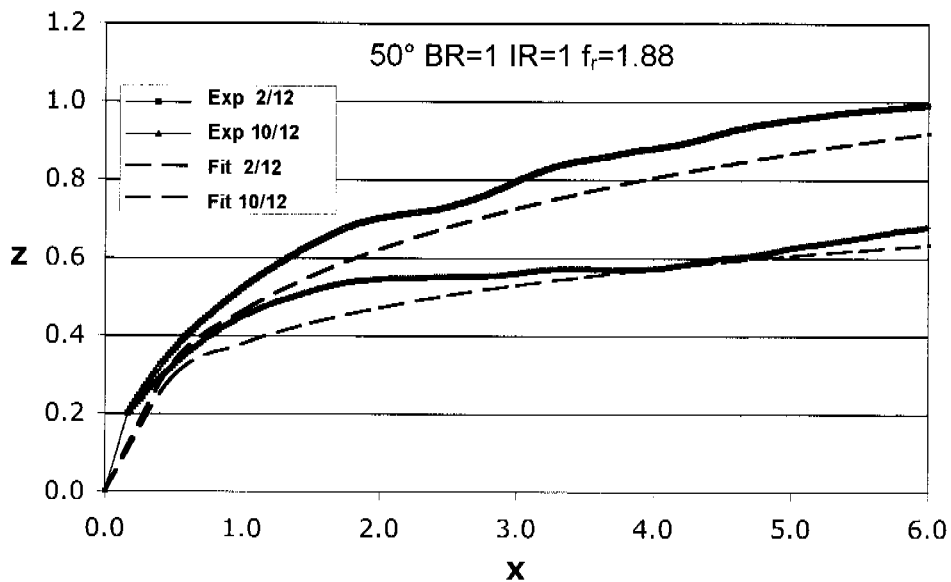
Figure 4.26: trajectory at maximum and minimum blowing ratio α =50°, BR=1, f_r=1.88

A clear change of the trajectory is visible also for this case with little variation of blowing ratio over the unsteady cycle. The phase resolved trajectories are matched well with the trajectory correlation. The quasi steady assumption is supported in this case.

4.5.3 Quasi Steady Circulation

Comparing the circulation of a steady and a phase averaged case is done in Fig. 4.27. The cases 7 and 14 are used with mean flow conditions of $\alpha=50°$, $BR=1$, $DR=1$ and $IR=1$. Pulsation frequency is $f_r=1.88$. It is clearly visible, that the pulsation has little influence on the phase averaged circulation. The almost perfect match of this derivative of the velocity field further supports the thesis of quasi steady behaviour in the case of small pulsation amplitude.
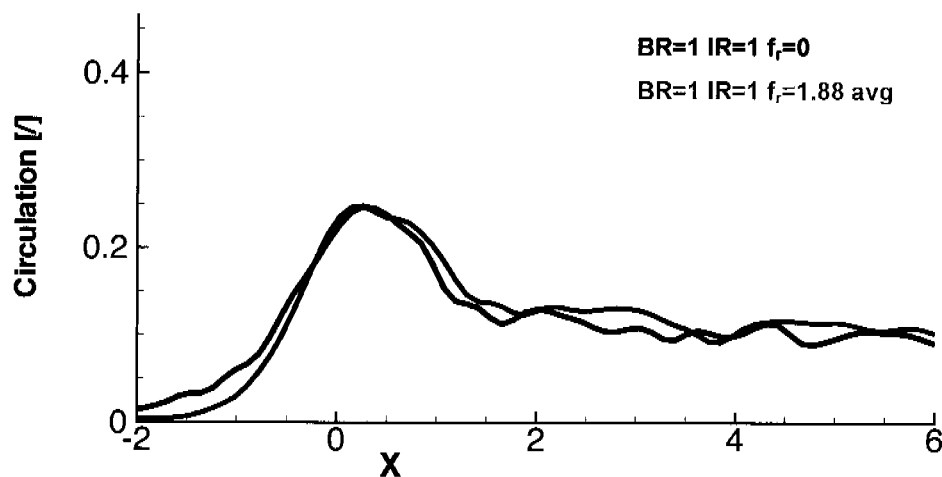

Figure 4.27: influence of pulsating on axial circulation; $\alpha=50°$, $DR=1.0$, $BR=1.0$

4.5.4 Summary

At $50°$ holes and $f_r=1.88$ pulsation a good match is observed, both with the phase average and the phase resolved data; the flow is quasi steady. Therefore the flow at lower frequencies should also be quasi steady.

The comparison to $30°$ $f_r=0.38$ case is different. The results suggest that the amplitude of the unsteady BR is an important factor. The strong amplitude must lead to some non-linear events e.g. flow separations. This event could be attributed to film 'lift off'. The isosurface time histories show unsteady lift of for this case (see Fig. 4.17). This would probably make a large difference as it is intermittent, when compared to steady attached or detached jets.

The quasi steady assumption is supported near the hole up to $f_r=1.88$ and with a pulsation amplitude $+-0.2$ in BR. For an amplitude of $+-0.7$ this is not well supported any more.

Overall, the further analysis will focus on the steady cases, which give sufficient information about the flow field with a pulsating injection of low amplitude.

4.6 Vortical Structure

This chapter discusses the vortical structure occurring in the film cooling environment. The three vorticity components and the axial circulation are utilized to identify the kidney and horseshoe vortices. The respective vorticity is directly derived from the velocity field at each data point. Non-dimensionalization is achieved with the free stream velocity and the hole diameter.

First a descriptive overview of all the steady measurements and the three vortical components is given. Then two cases are looked at in more detail, including their axial circulation.

4.6.1 Overview

The axial vorticity ω_x is plotted as iso-contour surfaces to achieve a good overall impression. First are the 10 steady cases in Fig. 4.28 and Fig. 4.29 with a set of $30°$ axial injection angle followed by $50°$.
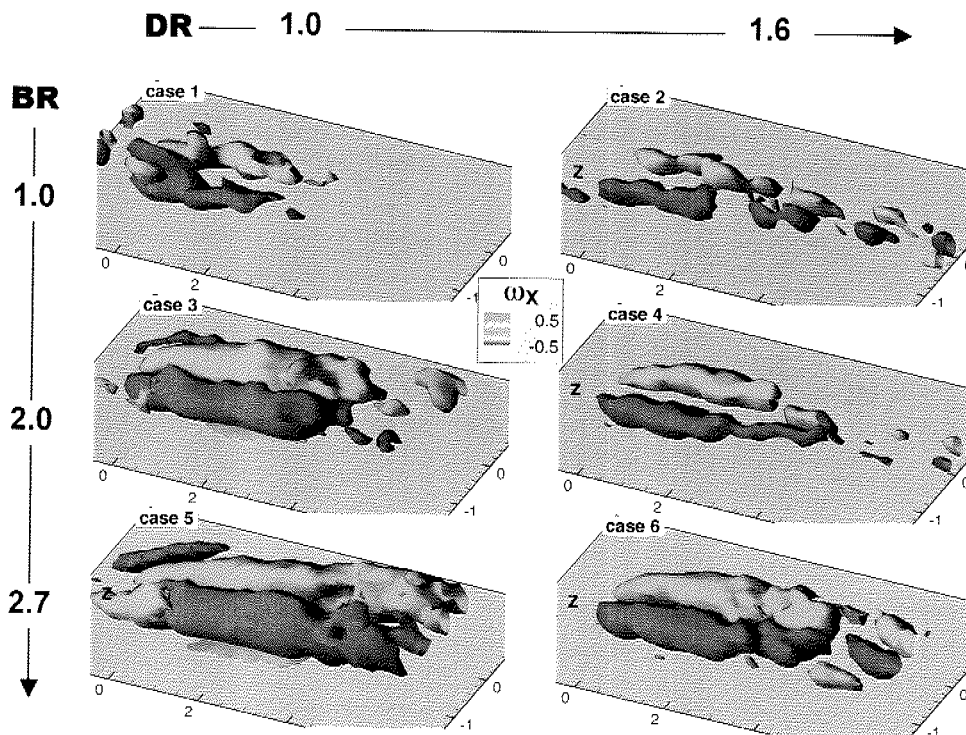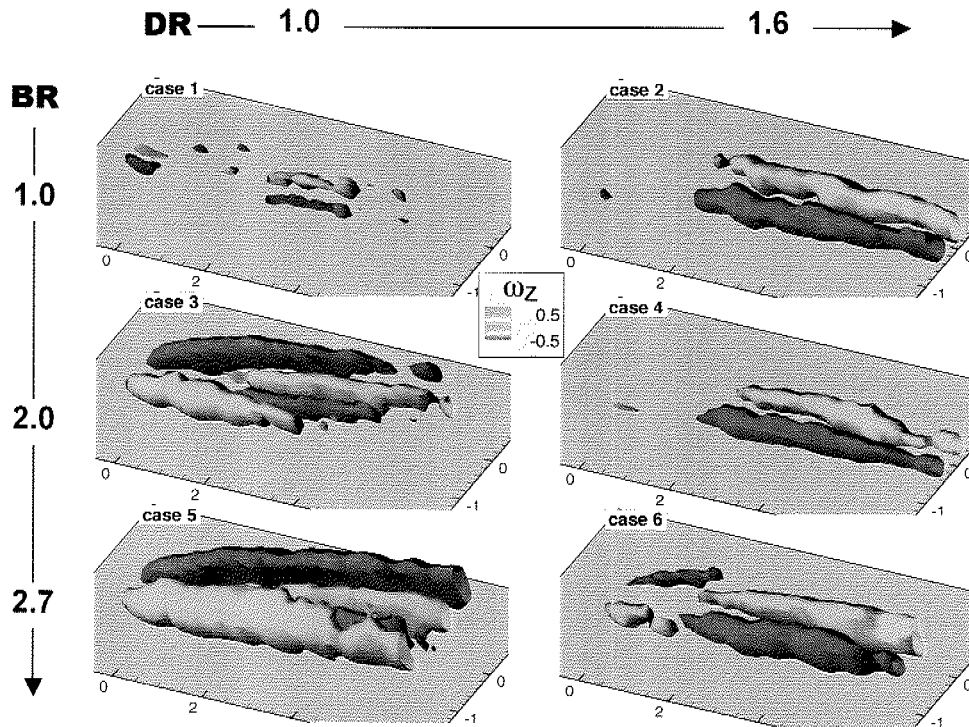

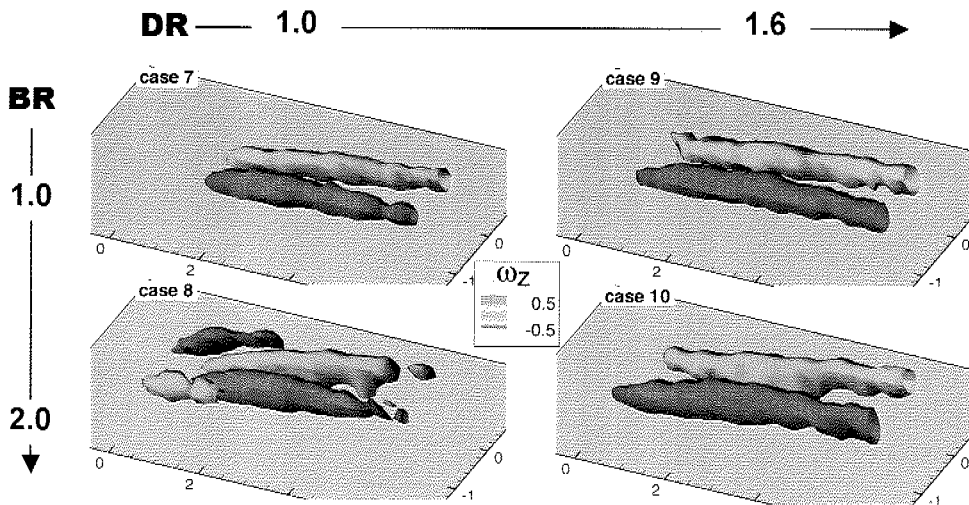Figure 4.28: axial vorticity with injection angle $30°$, cases 1 to 6

116
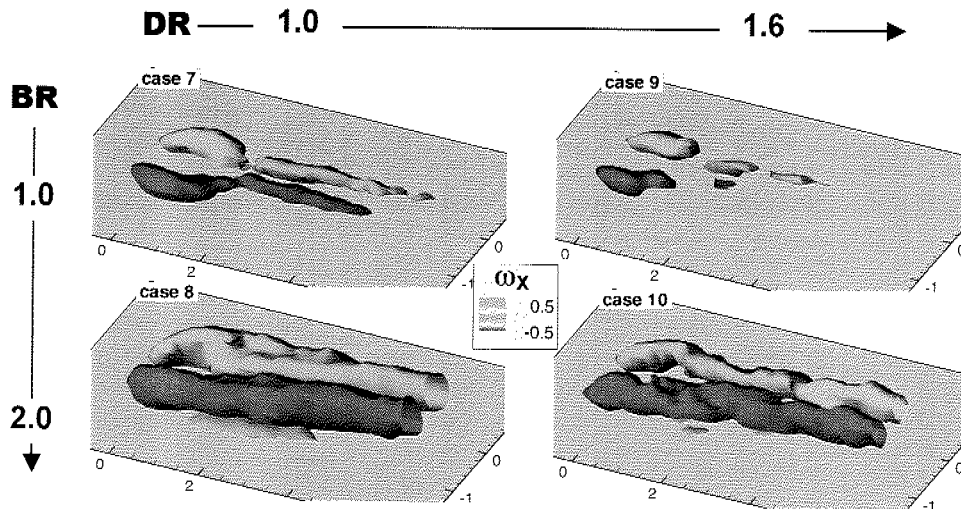
Figure 4.29: axial vorticity with injection angle *50°*, cases 7 to 10

The stream-wise vorticity, as shown in the previous two figures, indicates directly the location of the kidney vortex pair. It also shows the size of each vortex, and its extent in axial direction before it decays.

The 10 steady flow-conditions can be summarized as follows. Higher momentum flux ratio results in a kidney vortex pair that is bigger and extents further downstream. This is true for both streamwise injection angles and for different density ratios. Cases 3 and 5 show some indication of a horseshoe vortex, the small region on the upstream end with opposite sign. The *50°* cases show no horseshoe vortices.

The normal vorticity ω_y is plotted as iso-contour surfaces to achieve a good overall impression. First are the 10 steady cases in Fig. 4.30 and Fig. 4.31 with a set of *30°* axial injection angle followed by *50°*.
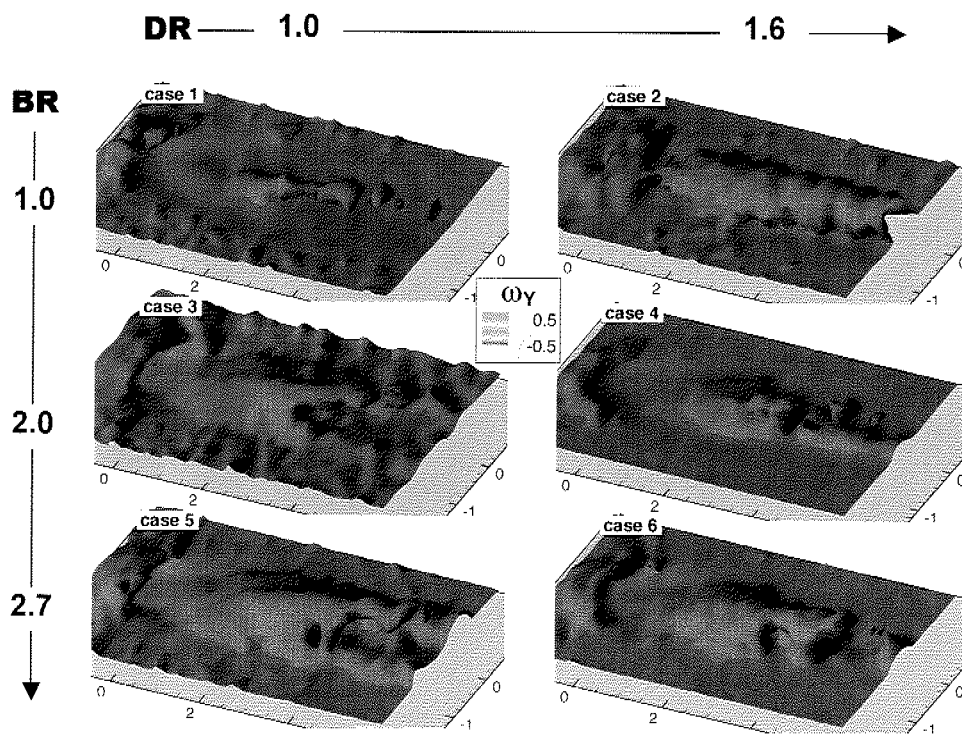
Figure 4.30: normal vorticity with injection angle $30°$, cases 1 to 6

Figure 4.31: normal vorticity with injection angle $50°$, cases 7 to 10

The normal vorticity indicates where the shear layers in the horizontal plane are located. Thus the two previous figures show the mixing zones of the jet. All 10 flow conditions show the inner mixing zone between the entrained fluid and the inner side of the jet. This feature increases slightly with increasing momentum flux ratio. The cases 3, 5, 6 and 8 show an outer mixing zone with reversed sign between the main flow and the outside of the jet. The cases with a momentum flux ratio below IR=1.6 show no pronounced outer mixing zone. This is partly due to the levels chosen in the presentation. This feature will appear as soon as the jet velocity is higher than the main flow velocity, i.e. for $BR>1$ if $DR=1$.

The lateral vorticity ω_Y is plotted as iso-contour surfaces, first the 6 steady cases with $\alpha=30°$ in Fig. 4.32 and then the 4 cases with $50°$ stream-wise injection angle in Fig. 4.33.

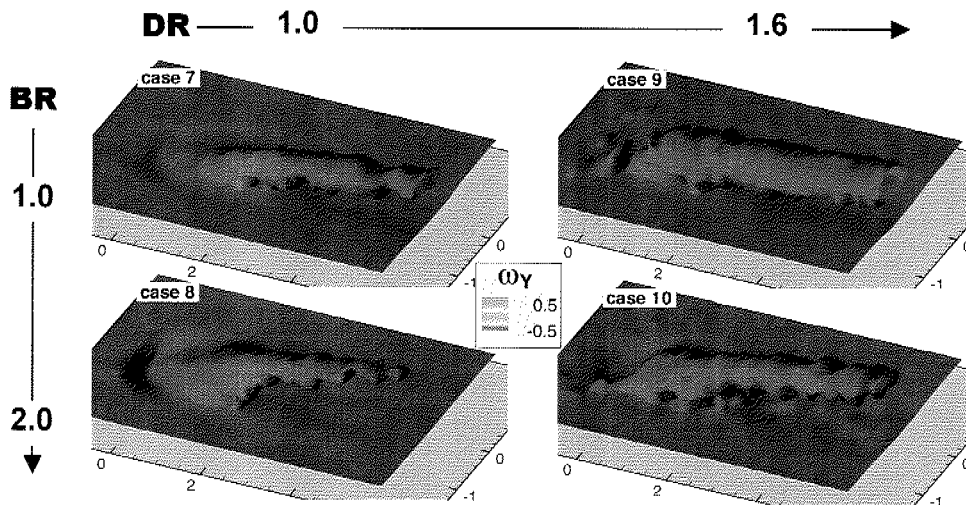**Figure 4.32:** lateral vorticity with injection angle $30°$, cases 1 to 6

Figure 4.33: lateral vorticity with injection angle 50°, cases 7 to 10

This type of vorticity is helpful in the characterization of undisturbed boundary layers as it describes the vertical change of velocity. The boundary layer is indicated by the flat blue plane outside the region of the jet, although it has to be noted that no information about its thickness can be derived from this type of representation. The figures above also help to identify the level of noise present in the data. Cases 1, 2, 3 and 5 seem to have a higher level of noise then the rest. In general the measurements with 50° injection angle seem to have higher quality data.

The region where fluid is entrained into the jet is indicated by the blue arms emerging on the centreline. The size or quantity of the entrained fluid again cannot be determined with this parameter. The area on the upstream side of the cooling hole is the most interesting feature to look at. This is where blockage of the main flow due to the emerging jet occurs, and where the formation of a horseshoe vortex is expected. The cases with 30° injection angle have a more pronounced feature there than the 50° cases. It is not possible to determine with final clarity if this is another artefact from the lower quality data, or if the 50° cases feature a less dominant horseshoe vortex.

4.6.2 Detailed Vorticity

Fig. 4.34 and Fig. 4.35 show plots parallel to the surface XY at 3 different heights from top to bottom. The holes are represented by ellipses of low eccentricity, showing the correct outline. The left column shows the streamwise vorticity ω_x. The

right column gives the vorticity normal to the surface ω_n. The third vortical component ω_y is not shown here, as it does not give further significant insight. Fig. 4.34 shows the low *BR*, *DR* and *IR* case for $\alpha=50°$ (case 7). We can see the streamwise vorticity ω_x associated with the boundary inside the cooling hole 'A'. We also see the trailing limbs of the kidney vortices fed by this vorticity. In Fig. 4.34. $Z=0.2$, streamwise vorticity, the vortices appear to attenuate rapidly with downstream distance; but this is due to the jet penetrating further into the mainstream flow. In $Z=0.6$, the signal of the kidney vorticity gets stronger 'B'. However, by $Z=1.0$, the vorticity values are much weaker, the jet does not penetrate this far. In Fig. 4.34 the normal vorticity reveals the dominant shear around the jet, positive on one side and negative on the other. At $Z=0.2$ the normal vorticity shows two weak regions of opposite sign 'C', indicating the position of the outer shear layer.
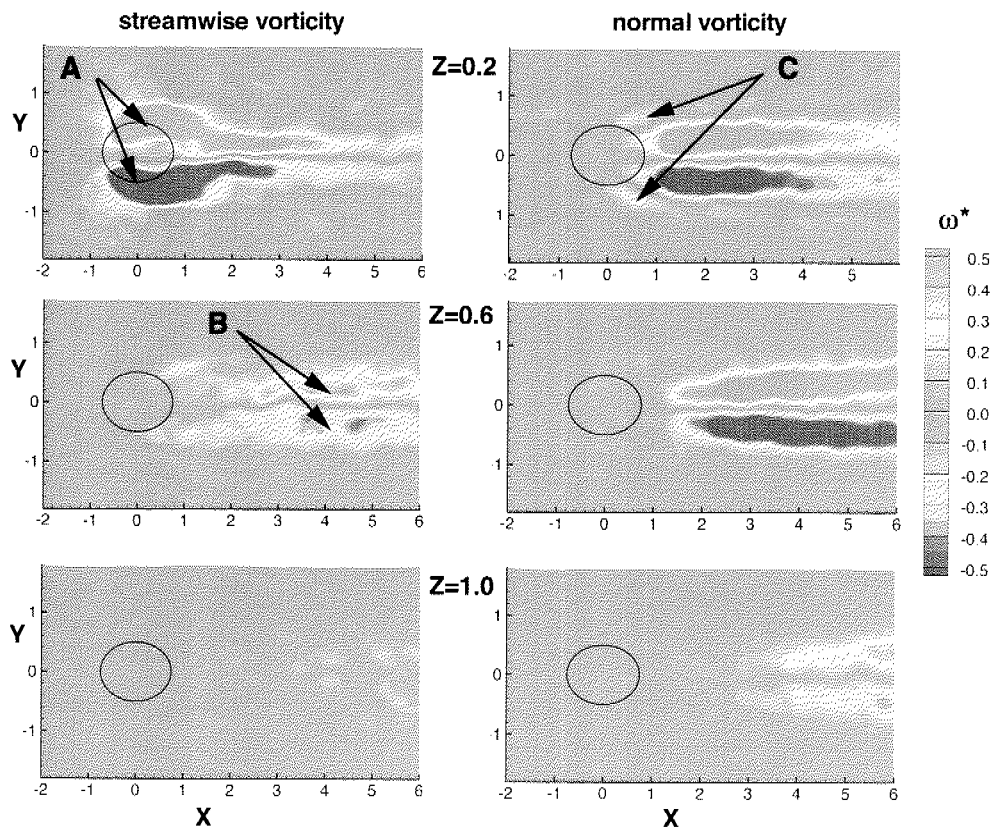

Figure 4.34: detailed vorticity, case 7, $\alpha=50°$ *BR=1 DR=1 IR=1*

In Fig. 4.35 we can see a significant change due to the increase of the blowing ratio. Penetration is much stronger and the vorticity has significantly greater magnitude. For the streamwise vorticity ω_x, near the wall at $Z=0.2$ evidence of a rather diffuse region of vorticity 'D' of the reverse sign of the kidney vortices can be seen. This can be interpreted as being vorticity due to the horseshoe vortex, which has been transported by unsteady flow structures and is rapidly mixing. At $Z=0.6$ and 1.0 we see the strong kidney vortex pair.

In Fig. 4.35 the normal vorticity ω_z shows four distinct regions. The central two are associated with the viscous mixing of the jet, as seen in Fig. 4.34 at lower blowing ratio. The outer two 'E' are also associated with the mixing of the jet. These appear to attenuate rapidly at all heights throughout the boundary layer. The reason we see this effect for higher blowing ratio is the higher velocity of the jet compare to its surroundings.
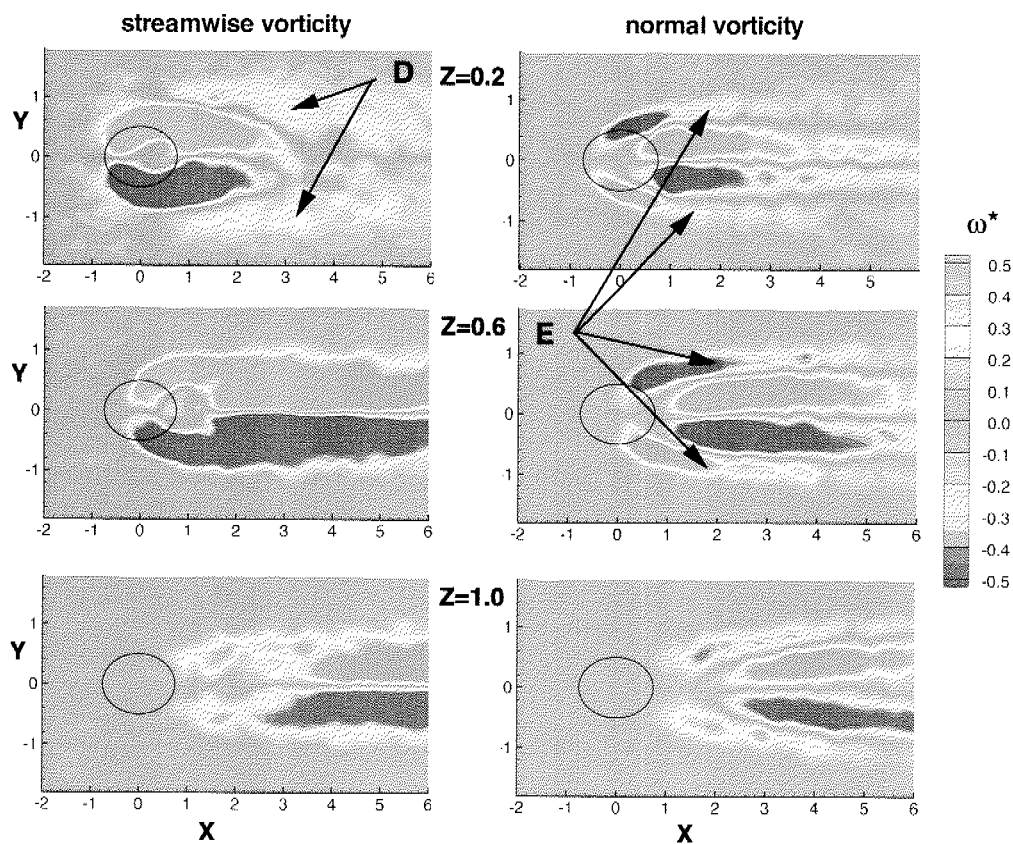

Figure 4.35: detailed vorticity, case 8, $\alpha=50°$ BR=2 DR=1 IR=4

4.6.3 Detailed Circulation

The axial circulation is extracted for the two cases 7 and 8, as shown in Fig. 4.36.
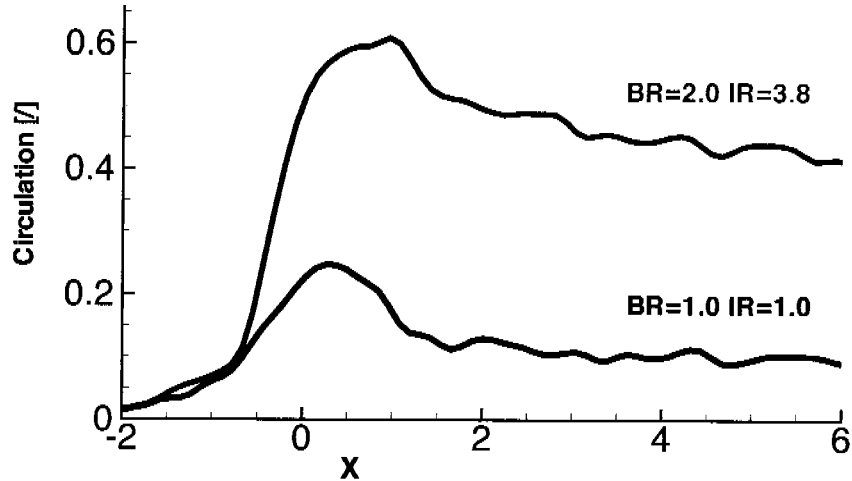

Figure 4.36: circulation as function of X and IR

The streamwise circulation is much greater for higher momentum flux ratio. It is almost proportional to the value of IR. The circulation upstream of the hole is near zero in both cases. In the region of the trailing edge of the hole the curves peak and then drop. Further downstream the level only drops slowly, indicating a slow dissipation of the vortical energy. The mixing out of those vortices is studied in Chapter 5.

Table 4.3: streamwise circulation for steady cooling injection

case	α	IR	Γ_{max}	$X_{\Gamma_{max}}$
1	30°	0.97	0.24	1.45
2	30°	0.65	0.26	1.69
3	30°	3.76	0.58	1.10
4	30°	2.51	0.36	1.46
5	30°	6.50	0.94	1.45
6	30°	4.19	0.52	1.46
7	50°	1.00	0.25	0.38
8	50°	3.78	0.61	0.96
9	50°	0.68	0.20	0.38
10	50°	2.56	0.34	0.15

Table 4.3 summarizes all the steady flow cases regarding the peak of the circulation and the axial position of this peak.

Above table contains a number of interesting aspects. First of all, the peak of the circulation in case of the 50° holes is clearly further upstream than for the 30° holes. All the 50° holes have the peak located above the hole, while the 30° holes show the Γ_{max} at about $0.5d$ downstream of the trailing edge of the cooling hole. The second interesting aspect is illustrated in the following Fig. 4.37.
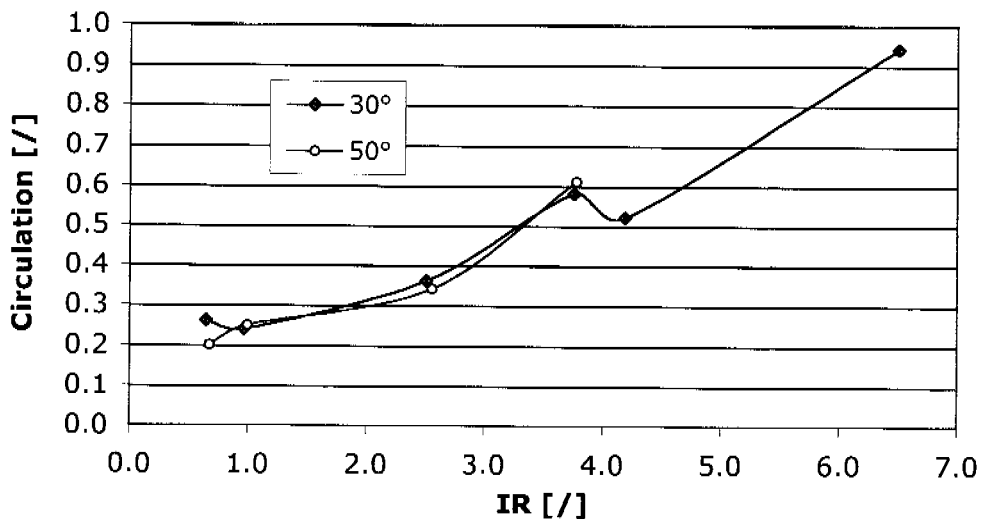
Figure 4.37: maximum circulation

Above figure indicates that the peak of the circulation scales linearly with the momentum flux ratio. This is relevant for the film cooling performance, as higher circulation causes higher mixing and thus reduces the effectiveness. Surprising is that the streamwise injection angle has no influence on Γ_{max}. Secondary flow theories like the one of Hawthorne [52] would lead to the expectation that a steeper injection angle results in a stronger streamwise vorticity and thus in a stronger streamwise circulation as the flow experiences greater turning.

4.6.4 Summary

All 10 steady flow conditions have been analysed regarding their vortical structure. The kidney vortices were identified, their respective extent was illustrated. Horseshoe vortices are only found in high momentum flux cases and *30°* stream-wise injection angle. It seems like the steeper injection angle of *50°* does not support the

formation of strong horseshoe vortices. It is expected, that horseshoe type vortices build up in all cases. In general they are not of great strength, and might also stay close to wall, making a detection with the used measurement technique impossible.

It is shown that the peak of the circulation scales linearly with the momentum flux ratio and that the streamwise injection angle has no influence on Γ_{max}.

4.7 Entrainment

The entrainment of fluid into the cooling jet is of interest as the entrained (usually hot) fluid raises the average jet temperature and thus reduces its potential film cooling effectiveness. Additionally, the jet entrains fluid from the surface boundary layer, reducing its thickness on both sides of the jet. This results in an increase of the heat transfer coefficient.

There are two general regions of entrainment. The outer region of the jet entrains surrounding free stream fluid due to mixing in the shear layer. The entrainment in this region is assumed to be small, as only a moderate lateral growth of the jet is observed in between $X=1$ and 6. The inner region of the jet entrains fluid from the boundary layer by the scouring effect of the kidney vortex pair and thus reduces its thickness in the surrounding area. This portion of entrainment is of primary interest.

An overview of the distribution of low velocity fluid is given in the beginning. A new parameter describing entrainment is defined, and its distribution in the flow domain is discussed together with the axial and lateral average.

Looking at iso-velocity plots gives a good impression of the 3D distribution of low momentum fluid. The following two figures each show an iso-surface representing $U/U_j = 0.95$. Effectively, the entrainment of low velocity fluid into the centre of the jet is represented here. Fig. 4.38 shows case 7 (with $\alpha = 50°$ $BR=1$ $DR=1$). Fig. 4.39 shows case 8 (with $\alpha = 50°$ $BR=2$ $DR=1$).

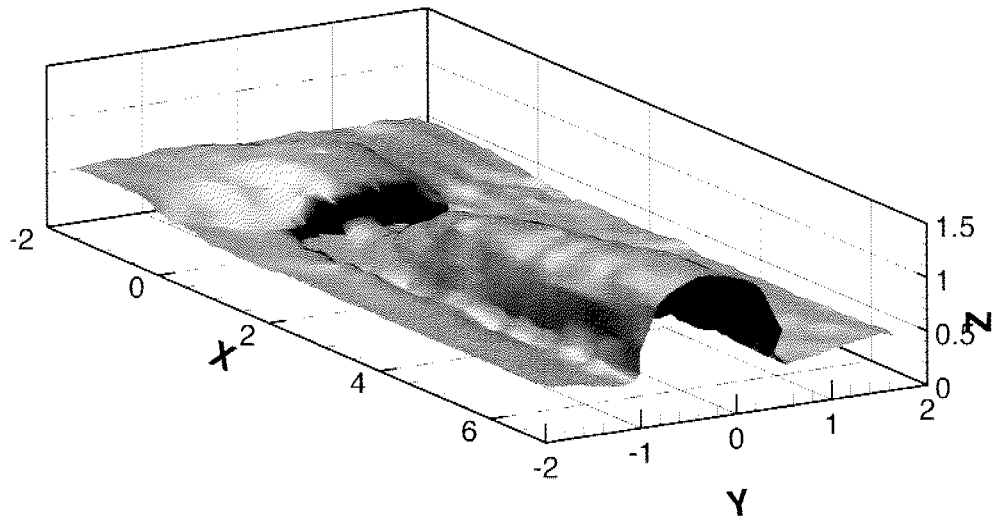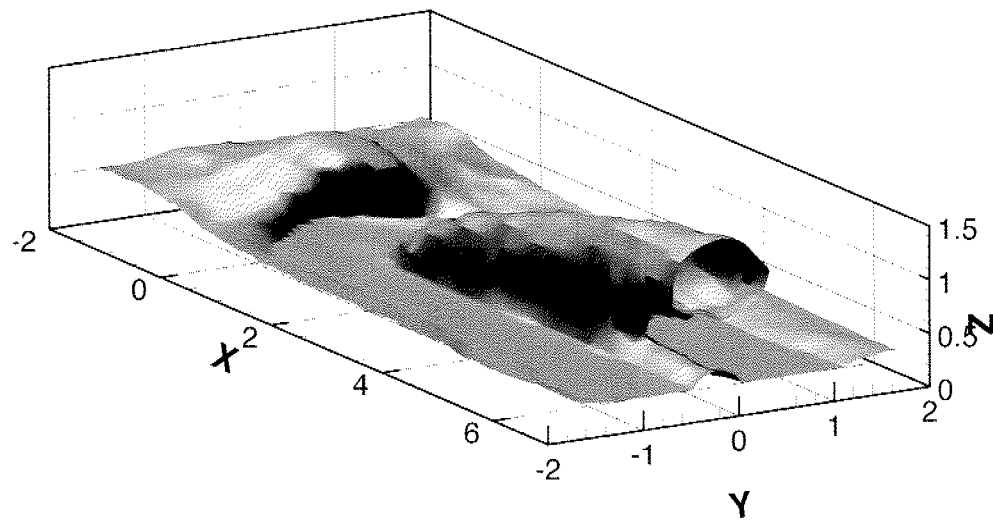**Figure 4.38:** iso-plane $U/U_i=0.95$; *50° BR=1 DR=1 IR=1*

Figure 4.39: iso-plane $U/U_i=0.95$, *50° BR=2 DR=1 IR=4*

The above figures show a number of interesting aspects. The boundary layer on the symmetry plane between two holes (at $Y=-2$ and 2) drops along the axial coordinate. This is mainly due to the entrainment of boundary layer fluid into the core of

the jet. This drop is slightly stronger for higher blowing ratio.

A clear bulb above the upstream edge of the cooling hole is visible in both cases. This bulb indicates the blockage of the main flow by the cooling jet, and is clearly stronger for higher blowing ratio.

The rise in the centreline of the jet is associated with the fluid entrained into the core of the jet. This effect looks quite different for the 2 blowing ratios chosen. At low blowing ratio an attached bulb spanning a rather big area is visible. The bulb in the high blowing ratio case is detached and encircles an altogether smaller area.

A new parameter ETR is defined for the further analysis. The definition of the entrainment parameter ETR is analog to the one of the displacement thickness of a simple boundary layer and takes the form of:

$$ETR = \left(\int 1 - \frac{u}{U_f} dz \right) - \left(\int 1 - \frac{u}{U_f} dz \right)_{X=-2, Y=0}$$

with the freestream velocity U_f and the axial velocity u at the position Z above the surface. The integration is done in the range from $Z=0$ to $Z=2$. The second term in brackets represents the reference value of the freestream at $X=-2$ and $Y=0$. Filtering of the velocity data is required before this calculation is performed. Velocities above the freestream level are set to the free stream value to avoid artificial decrease of ETR which is not related to entrainment.

This parameter takes only the axial velocity component into account, which experiences the strongest change. This parameter can be treated as a displacement thickness in regions of 1D-flow, which is true in the symmetry plane between two holes. Negative values of ETR indicate a displacement of the low momentum layer relative to the undisturbed boundary layer upstream of the hole. Positive values indicate an addition of low momentum fluid, in other words entrainment, at the respective location. The drawback of this parameter-definition is that a separation between entrainment on the inside of the jet and on the outside is not possible.

This parameter is derived for the two previously presented cases 7 and 8, the result is shown in the following two figures.
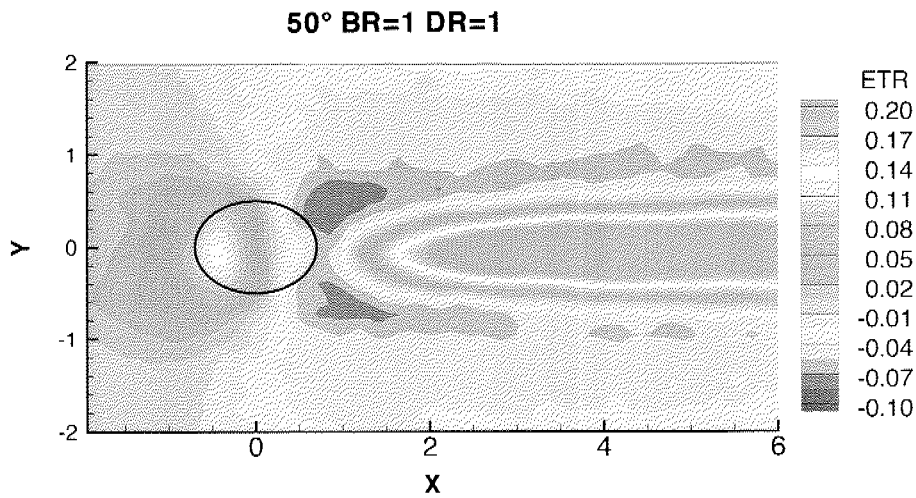
50° BR=1 DR=1

Figure 4.40: entrainment with case 7, *50° BR=1 DR=1 IR=1*
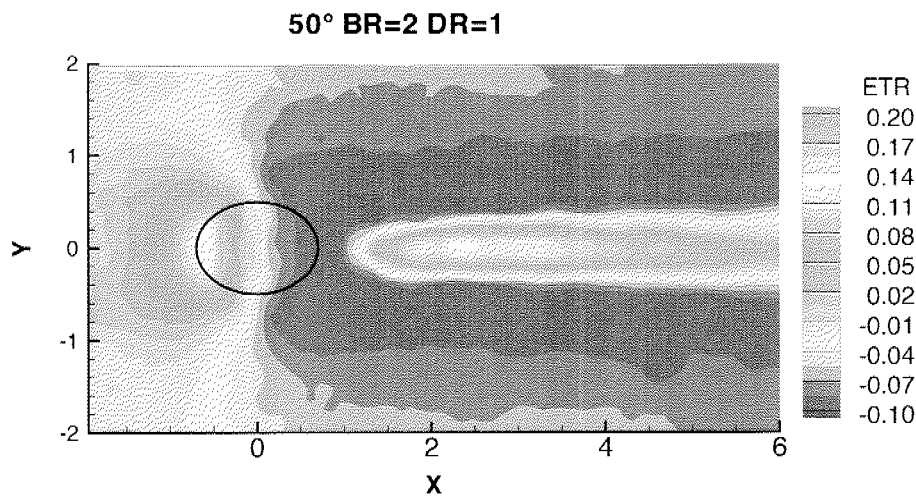
50° BR=2 DR=1

Figure 4.41: entrainment in case 8, *50° BR=2 DR=1 IR=4*

These two figures support the findings achieved with the iso-velocity plots. The displacement thickness on the symmetry plane drops next to the cooling hole. This drop is stronger for higher blowing ratio. The increase of low momentum fluid above the leading edge of the cooling hole is visible as well. This is not due to entrainment.

The amount of entrained fluid in the centre of the jet is lower for high blowing ratio which is expected from the iso-velocity plots as well, where it was apparent that the area surrounded by the contour is bigger in the low *BR* case. A direct comparison between the level of entrainment in the centreline for the two blowing ratios is not possible, as the difference in jet velocity contributes to *ETR*.

It can be postulated, that the average jet velocity decreases after injection due to friction and diffusion. The change of *ETR* along the axial coordinate can be discussed with that assumption. The area next to the hole experiences acceleration, thus lowers *ETR*. It has to be noted, that the acceleration is local around the holes and does not expand over the entire passage height. This is based on the fact that the variation of velocity at $Z=3$ is less than 1% of the freestream value.

Looking at the centreline trend (Fig. 4.40 and Fig. 4.41) a distinct difference between the two blowing ratios is visible. Most of the entrainment for the high blowing ratio case takes place between the hole and $X=2.5$. The centreline value of *ETR* drops downstream of that location, leading to the conclusion, that no significant amount of low momentum fluid is entrained from there on. The low blowing ratio case experiences its main increase in centreline *ETR* up to $X=3$. From there on it continues to rise only gradually. This difference can be attributed to jet lift-off, which is visible in the iso-velocity plots Fig. 4.38 and Fig. 4.39. The low blowing ratio case is attached and seems to continue entrainment from the boundary layer fluid. The high blowing ratio case is lifted off and subsequently does not feed from the boundary layer.

The next figure shows the level of *ETR* in the symmetry plane ($Y=2$) for both high and low blowing ratio.
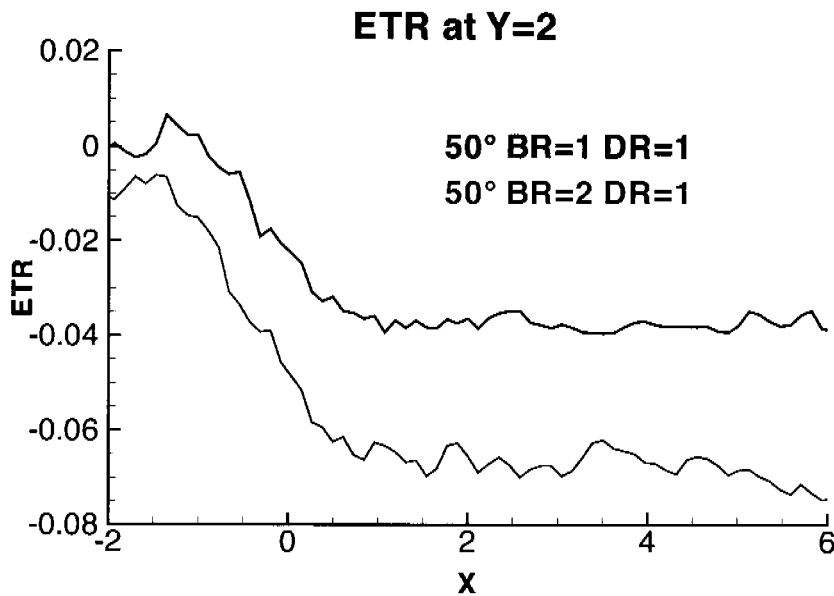
Figure 4.42: ETR at Y=2, in case 7 and 8

The parameter *ETR* is similar to the displacement thickness at the symmetry plane. A strong decrease of *ETR* is visible in both cases, starting slightly upstream of the leading edge of the hole (which spans from $X=-0.65$ to 0.65). This decrease extends beyond the trailing edge of the hole to about $X=1$. After that the level of *ETR* stagnates for the low *BR* case and continues to drops slightly in the high *BR* case.

The reduction of the displacement thickness depends on *BR* / *IR*. In numbers, the displacement thickness for $BR=1$ is reduced by 21% relative to the undisturbed freestream boundary layer, while the reduction for $BR=2$ is about 36%. This reduction has a direct impact on the heat transfer coefficient, the higher blowing ratio will cause a higher heat transfer coefficient.

The decrease is potentially associated with two effects, the acceleration of the fluid due to blockage and the reduction of the boundary layer by entrainment. These two effects are not easily separated. Entrainment is not expected to occur upstream of the hole. The start of the downslope is therefore associated with acceleration. The acceleration is not expected to extend much beyond the hole. The decrease does continue its downward trend further downstream without significant change of its slope. Therefore it can be postulated that the driving factor is the entrainment of the boundary layer.

The second part of the curve from $X=1$ downstream shows two general physical effects that influence the value of the entrainment factor. The frictional growth of the boundary layer would tend to increase ETR, while entrainment of boundary layer fluid into the jet would decrease it. The streamwise change in pressure rise due to streamwise diffusion is not expected to play a significant role. The system data does show a general decrease of pressure over the test section, indicating that an occurring pressure rise is local and not very strong.

To conclude, it is shown, that the boundary layer experiences a strong reduction next to the cooling holes. From $X=2d$ it starts to thicken gradually. This change in boundary layer thickness is directly related to the heat transfer coefficient. However, the region where this effect is the strongest is thermally protected from over-heating on a real turbine blade, as heat conduction in the blade material to the cooling holes gives an extra cooling effect.

5. MIXING

This chapter introduces a novel approach to the analysis of raw PIV images. The measurements are taken with a distinct difference between the seeding concentration in the main flow and cooling flow. Thus, the concentration of cooling flow in the flow domain is detected.

A dimensionless parameter is introduced to describe the respective cooling concentration CC in the first part of this chapter. The detailed distribution of the cooling concentration is analysed.

The rate of mixing between cooling jet and main flow is derived from the cooling concentration in the second part of this chapter. This information is averaged at axial planes to get the overall trend of the rate of mixing in the axial direction. The result is matched with an appropriate function and a typical length scale of the decay of mixing is found. This length scale is compared to the corresponding length scale found in the decay of circulation along the axial coordinate.

The conservation equation of cooling concentration is established in the third part of this chapter. This equation is fully defined by measured CC and velocity data, except for the diffusion coefficient. Information about the spatially resolved diffusion coefficient is gained from the data.

This chapter will analyse one flow condition, the case 13 in Table 4.1. The seeding of both flows in this measurement proved to be of exceptional contrast, enabling the subsequent analysis. The respective flow conditions are: $\alpha=30°$, $M=0.3$, $DR=1.0$, $BR=2.0$, $IR=3.7$, $f_r=1.88$.

5.1 Cooling Concentration

The raw PIV pictures are dewarped with the calibration matrix introduced in chapter 3 to transform them into planes parallel to the surface. The single pictures are

averaged over all the pictures taken for each condition and Z-position, usually a number of 30. A sample of a dewarped and averaged picture is shown in Fig. 5.1. This picture is taken one diameter above the surface.
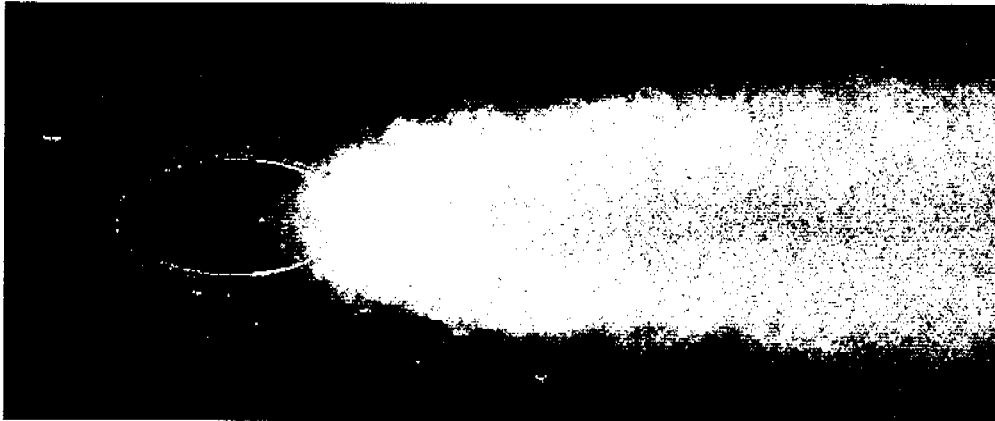

Figure 5.1: seeding concentration difference between main and cooling flow

The averaged image is then subdivided into interrogation areas of 32x32pixels size. The respective recorded light intensity LI of the pixels of each sub-area is averaged. The sub-areas are overlapped by 50% in both directions, analoge to the procedure described in Chapter 3. Then the averaged planes at different vertical positions above the surface are assembled to a flow volume.

The amount of light reflected from the particles LI_i, at each point i in the data volume is averaged over the sub-area and the number of pictures taken. The light intensity at two reference points is read from the data set. The reference point LI_f for the main flow is at $X=-2d$, $Y=0d$, $Z=2d$, which is upstream of the centre of the cooling hole, two hole diameters above the surface. The reference point for the cooling flow LI_c is at $X=0d$, $Y=0d$, $Z=0.2D$, which is at the centre of the cooling hole at the measurement plane closest to the surface.

The main assumption in this analysis is that the amount of light reflected from the seeding particles is directly proportional to the concentration of coolant. With that assumption a dimensionless parameter representing the cooling concentration at each point CC_i can be defined as:

$$CC_i = \frac{\left(LI_i - LI_f\right)}{\left(LI_c - LI_f\right)}$$

The cooling concentration describes the location of coolant in the flow volume above the surface and thus gives insight into mixing and entrainment.

Obviously, reflections from the surface will directly influence the result obtained. They appear as area of high cooling concentration, while there might not be coolant at all. This can be seen in the sample picture in Fig. 5.1. Here the edge of the hole is clearly visible. The hole area therefore is blanked out in the figures to come.

A large number of pictures have to be taken in general to reduce the noise to an acceptable level. The difference in seeding concentration should be as large as possible. However, enough seeding particles must remain in both flows to enable the cross-correlation procedure. This fine line was met with one of the later measurements taken, where only the cooling flow was seeded. Enough seeding particles recirculated in the main flow to enable a successful correlation.
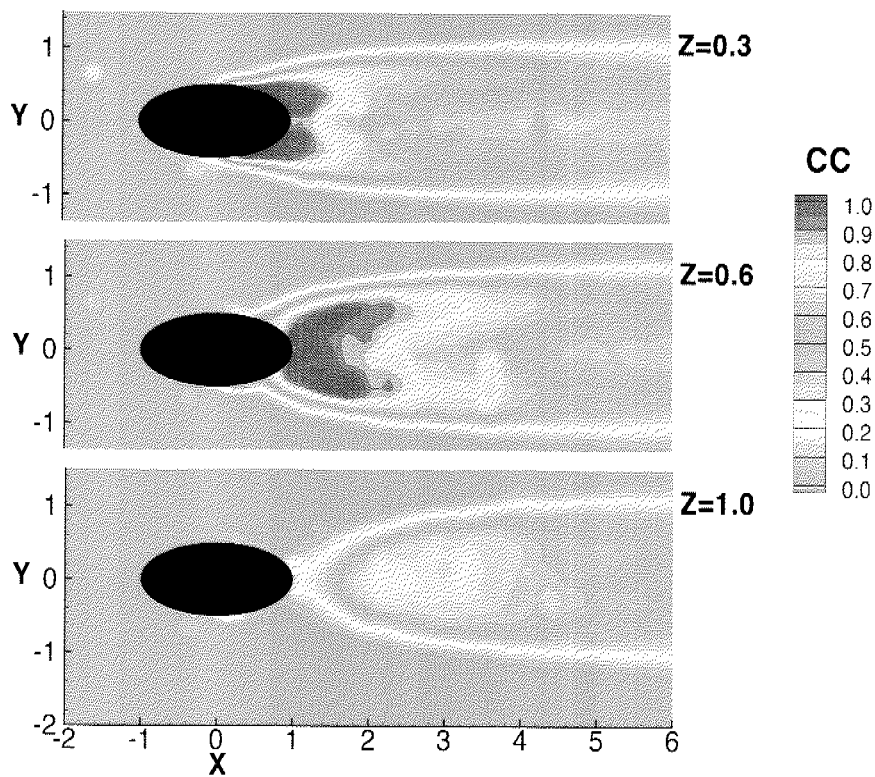

Figure 5.2: cooling concentration at different Z-planes

The case that is analysed in the following section has the number 13 in Table 4.1. The axial hole angle is $30°$, a density ratio of $DR=1.0$, a blowing ratio of $BR=2.0$, and a pulsating frequency of $f_c=1.88$ are the flow conditions present. The data pre-

sented here is the phase average of the entire data set.

It is visible that the lateral diffusion is rather slow. There is hardly any widening of the cooling jet at a low level of Z. The main concentration of the coolant spreads from just downstream of the hole to two arms at the bottom end of the kidney vortex pair. The bulk of unmixed coolant stays in the windward side of the jet at higher levels above the surface, as can be seen at $Z=0.3$ and $Z=0.6$. At these levels concentrations of 90% to 100% are observed. At an even higher level of $Z=1.0$ the concentration in that part of the jet drops to about 70%. The spreading of higher concentrations of coolant into the respective centres of the kidney vortices can be observed. Also visible is the effect of entrainment of main flow fluid into the centre of the kidney vortex pair at the lower three levels. At $Z=1.0$ this is not observed any more.

A different way to present this data is with iso-contour surfaces of CC as shown in the following two figures, Fig. 5.3 and Fig. 5.4. The jet is cut in half to gain information about the internal distribution, first along the centre line at $Y=0$ in Fig. 5.3 and then parallel to the surface at $Z=0.8$ in Fig. 5.4. This second figure first shows the cut from above and then from an angle.
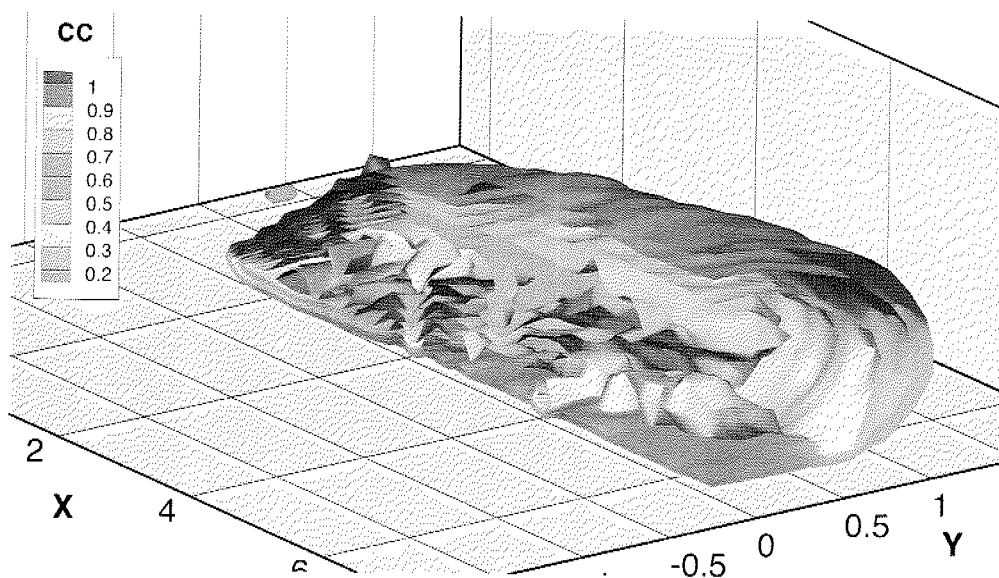

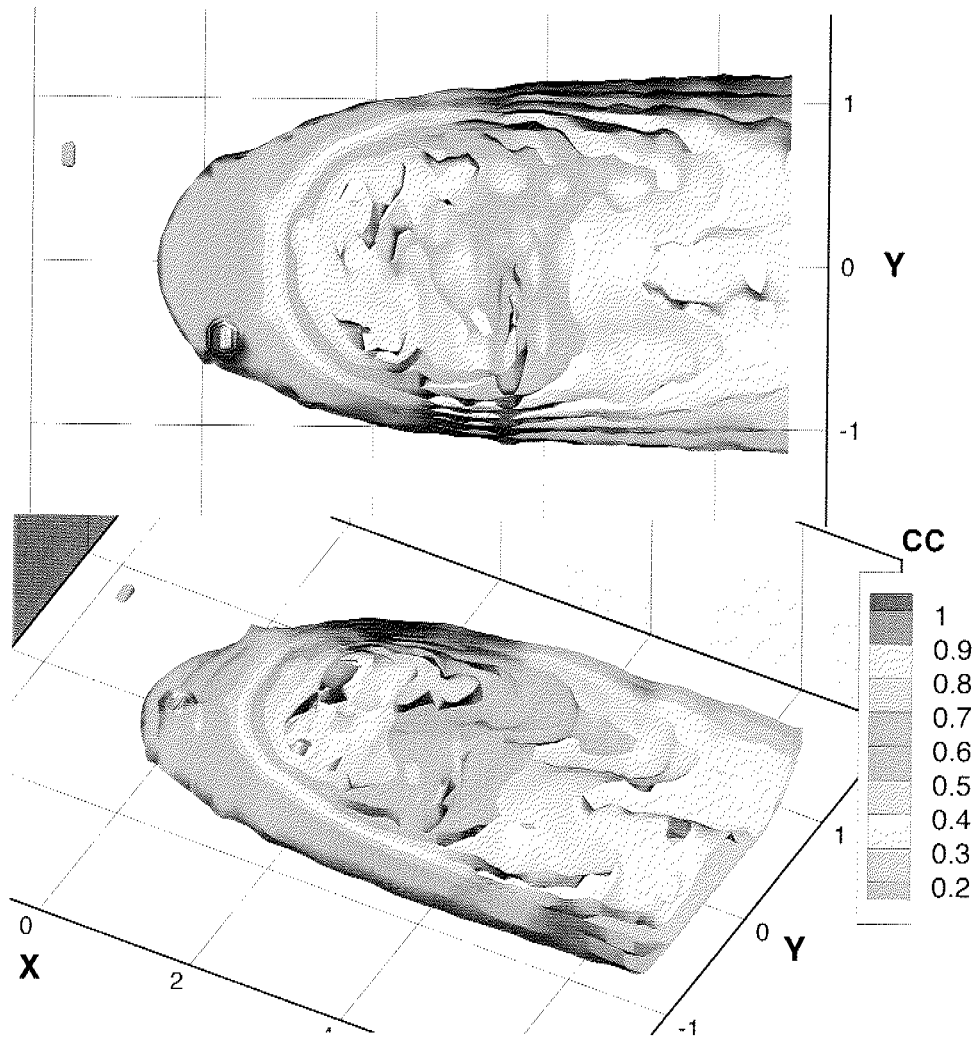**Figure 5.3:** cooling concentration as iso-contour plot, cut at $Y=0$

Figure 5.4: cooling concentration as iso-contour plots, cut at Z=0.8

Laterally the low concentration mixture of about 20% spreads to about double the width of the cooling hole in the near hole region we are looking at. The higher concentration levels above 80% disappear almost entirely after three hole diameters through mixing. Again the location of high concentration of coolant near the windward side of the jet is clearly visible.

The phase resolved structure of the cooling concentration is given in the next set of pictures in Fig. 5.5.
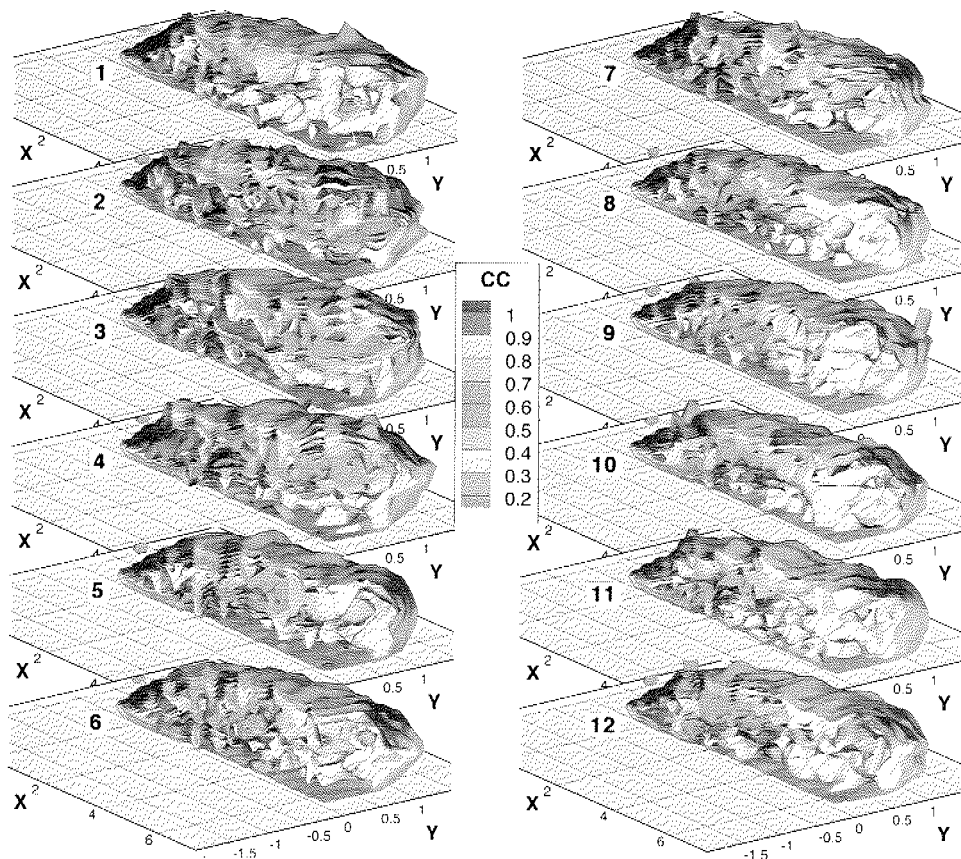
Figure 5.5: phase resolved cooling concentration of case 13

This figure indicates that there is no dramatic changes taking place over the phase. The outer contour does not change much. The biggest change is observed in the high concentration region just above and downstream of the hole. This region spreads the furthest downstream in the third part of the phase, while a minimum is observed in phase 10. These two are shown in detail in the following two illustrations Fig. 5.6 and Fig. 5.7. The observed phase of the maximum and minimum correspond to the variation of the blowing ratio (see Fig. 4.6).
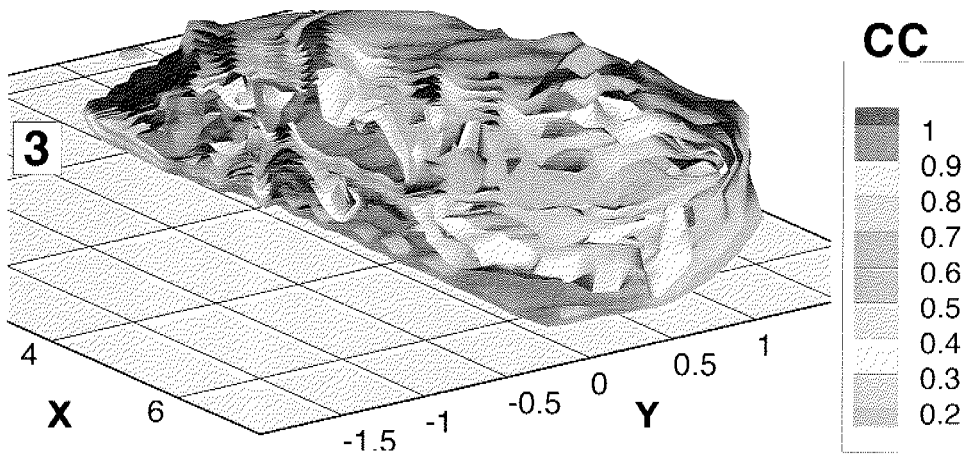
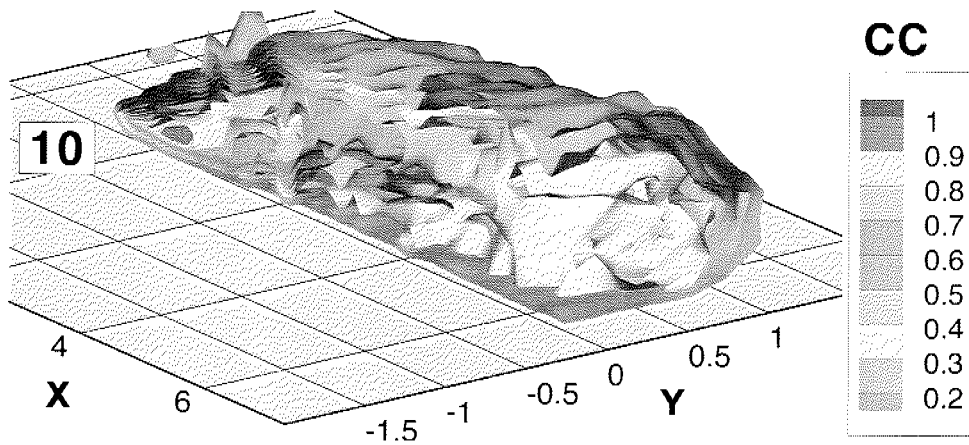**Figure 5.6:** detail of phase resolved CC, phase 3/12, case 13

Figure 5.7: detail of phase resolved CC, phase 10/12, case 13

These two detailed figures show that the elevation of the jet above the surface changes over the course of a pulsation. The lateral extent is not strongly influenced, however. The biggest variation takes place in the inner regions of the jet. A clearly pronounced region of high CC (above 90% at $Y=0$) extends to almost $X=4$ at the maximum of the cycle. The minimum of the pulsation cycle only shows concentrations above 90% just over the hole.

5.2 Rate of Mixing

Mixing involves fluxes of the variable in question due to its spatial gradients. This can be expressed as the 3D vector equation:

$$\vec{M} = -g\nabla CC$$

In this equation $\vec{M}$ is the 3D flux vector:

$$\vec{M} = i\,M_x + j\,M_y + k\,M_z$$

g is a constant 'isotropic transport coefficient' of mixing and ∇CC is $grad\,CC$, the gradient vector of the coolant concentration CC:

$$\nabla CC = i\frac{\partial CC}{\partial x} + j\frac{\partial CC}{\partial y} + k\frac{\partial CC}{\partial z}$$

The rate of mixing is expressed by calculating the magnitude of the 3D flux vector:

$$|\vec{M}| = |g|\sqrt{\left(\frac{\partial CC}{\partial X}\right)^2 + \left(\frac{\partial CC}{\partial Y}\right)^2 + \left(\frac{\partial CC}{\partial Z}\right)^2}$$

The spatial distribution of both the cooling distribution and the rate of mixing are shown in the following figures. The isotropic mixing coefficient is unknown and assumed to take the value of 1. This does not have an influence on the qualitative result but only on the magnitude. The flow conditions are $\alpha=30°$, $BR=2$, $DR=1$, $f_r=1.88$ and the phase averaged case is analysed. CC and M are shown at two axial and vertical planes, each. The mixing flux plots indicate where a strong flux should be expected, but it is not in a known direction.
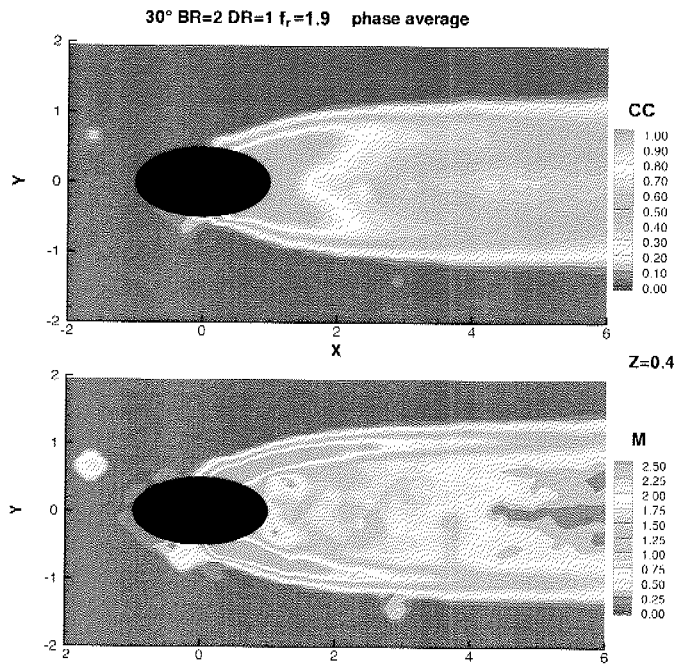
Figure 5.8: cooling concentration and rate of mixing at *Z=0.4*
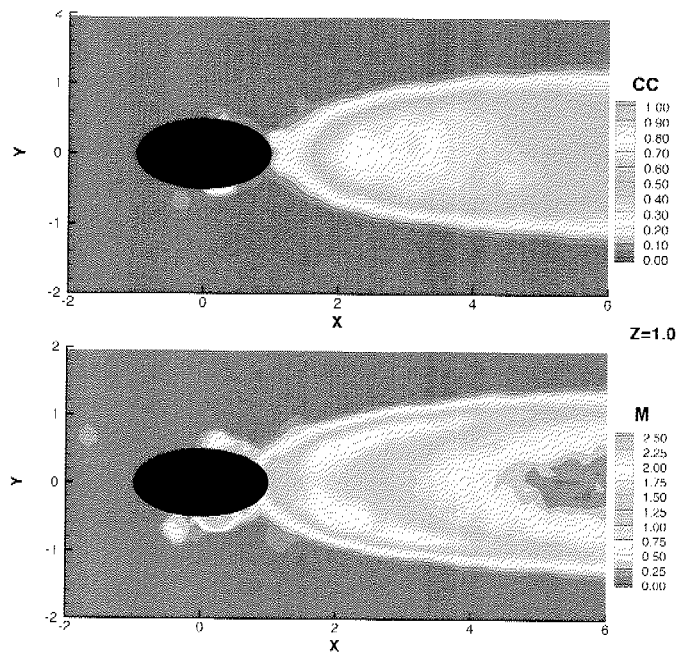
Figure 5.9: cooling concentration and rate of mixing at *Z=1.0*

The two previous figures show that a high mixing rate is present at the outer side of the cooling jet, corresponding to the outer part of the kidney vortex pair. An elevated mixing rate is present also on the windward side of the jet. The centre of the jet downstream of $X=4d$ produces a negligible mixing rate, despite the fact that the cooling concentration is in the order of 50%.
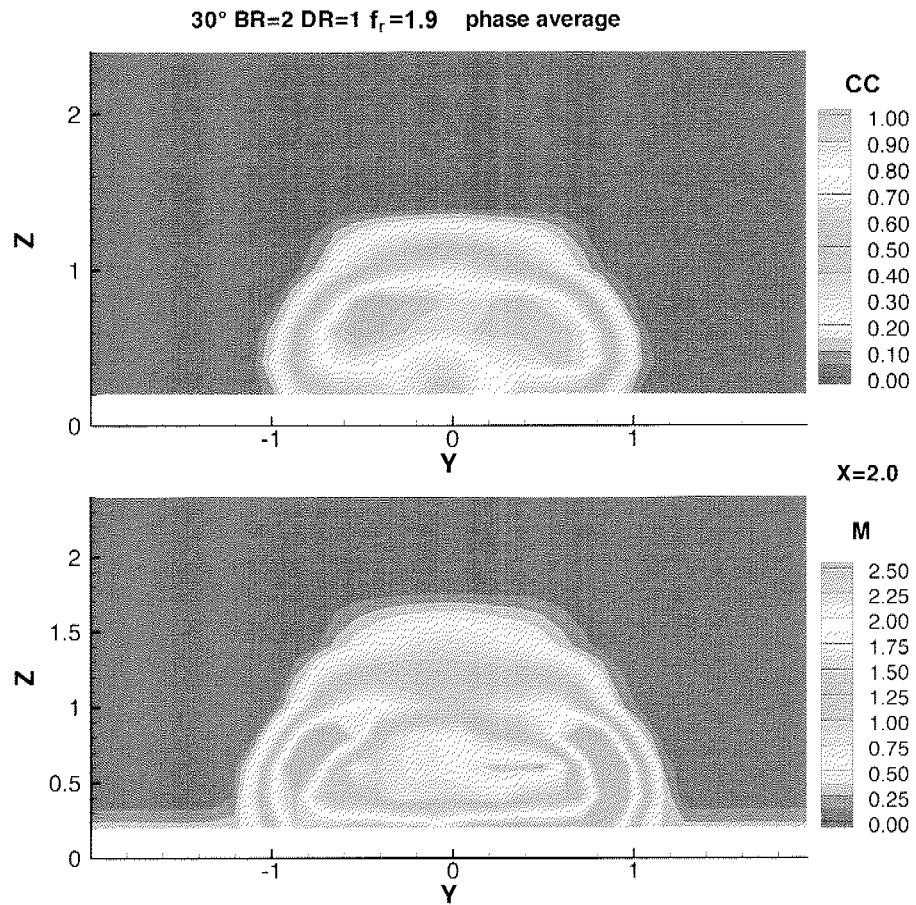
30° BR=2 DR=1 f_r=1.9   phase average

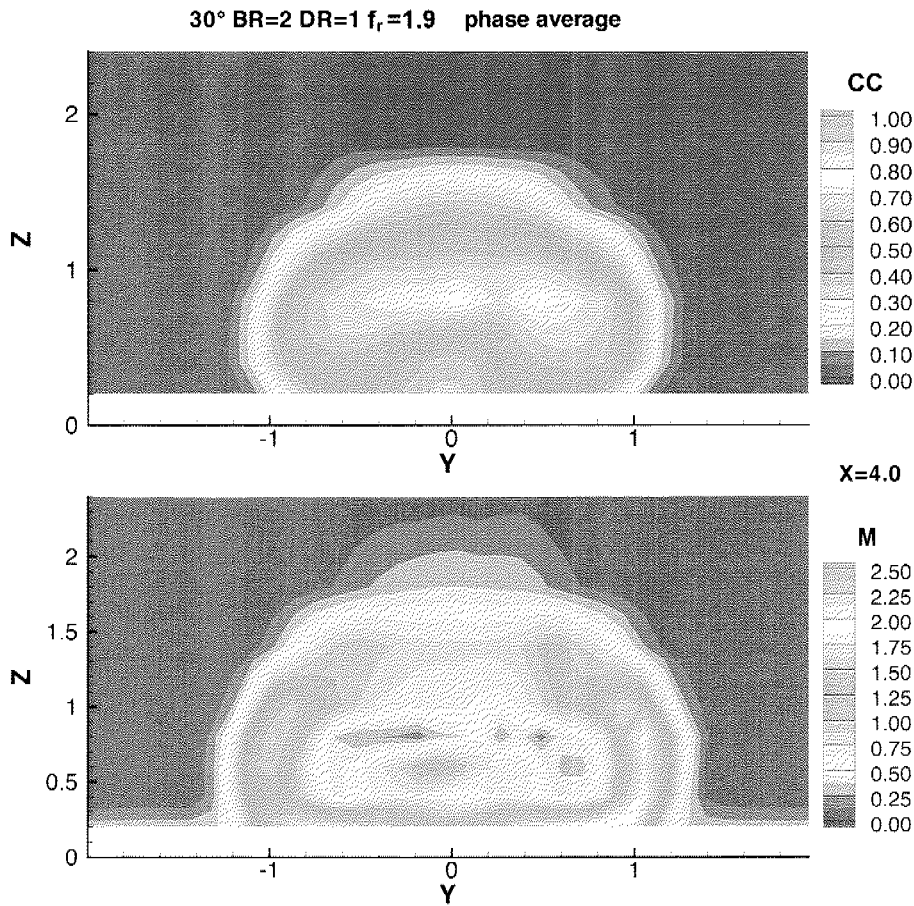Figure 5.10: cooling concentration and rate of mixing at $X=2.0$

Figure 5.11: cooling concentration and rate of mixing at $X=4.0$

The figures above again show that the rate of mixing is strongest in the outer mixing region of the jet. The windward side of the jet sees a stronger mixing rate in the region close to wall. The core of each kidney vortex and the region in-between have a rather low mixing rate. The region below the measurement plane closest to the wall at $Z=0.2$ gives artificial information, as the CC-data on the wall is set to zero. Deriving the rate of mixing carries this artifact into higher levels of Z, as can be seen in the slight gradient on both sides of the cooling jet in Fig. 5.10 and Fig. 5.11.

The rate of mixing is now averaged in axial planes to produce the variation of the rate of mixing. Assuming that the transport coefficient g is a constant the variation in the rate of mixing can be plotted.

The result for the phase averaged case with the parameters $\alpha=30°$, $B=2$, $D=1$, $f_r=1.88$ is shown in the following Fig. 5.12. The axial circulation, as introduced in Chapter 4.2.2 is included in this plot.
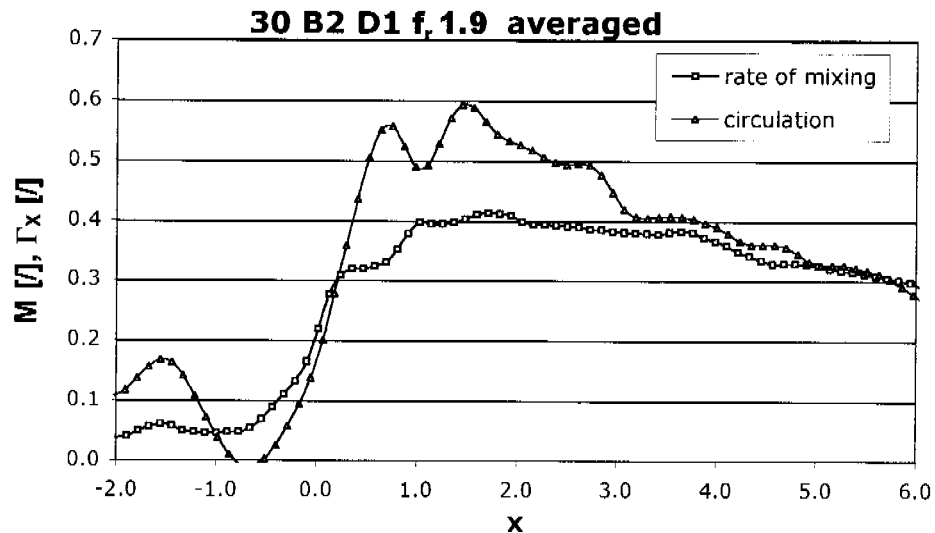

Figure 5.12: averaged rate of mixing versus axial circulation; case 13

The mixing of the coolant jet and the viscous dissipation of the associated circulation may be dominated by the same flow structure. If so one would expect similar lengthscales in the exponential decay of these features.

An appropriate function to describe the behaviour of both parameters is of the following form:

$$Y = a + b \cdot \exp\left[-\frac{X}{L}\right]$$

This function matches the measured parameters from the trailing edge of the cooling hole at $X=1$ with a standard deviation of the order of 0.01.

The coefficient L is the typical length scale to describe the dissipation of circulation and the mixing out respectively. It is visible that both typical length scales are very close in value. This indicates that mixing rate and circulation diminish at the same rate, which again indicates that a Prantl number close to unity is present. The fitting coefficients for both parameters are summarized in the following table:

143

Table 5.1: coefficients describing exponential decay

	a	*b*	*L*
rate of mixing	0.284	0.192	3.650
circulation	0.188	0.544	3.891

The approximation by this equation are shown in the following two figures Fig. 5.13 and Fig. 5.14.
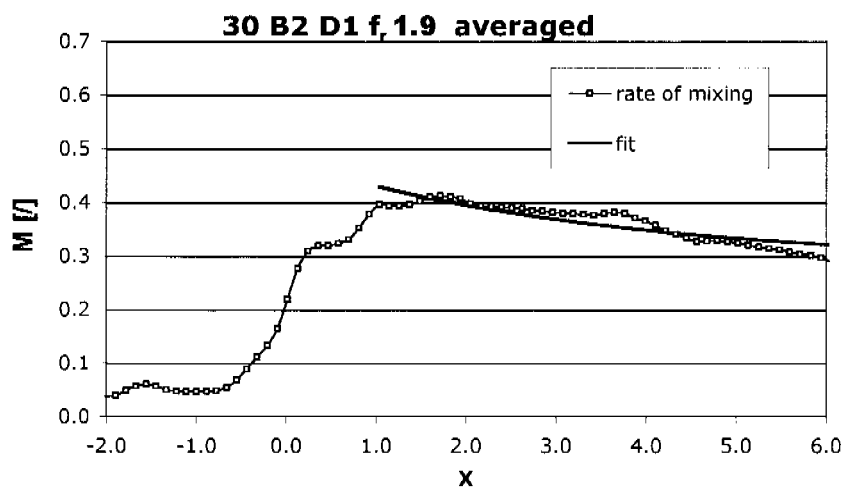

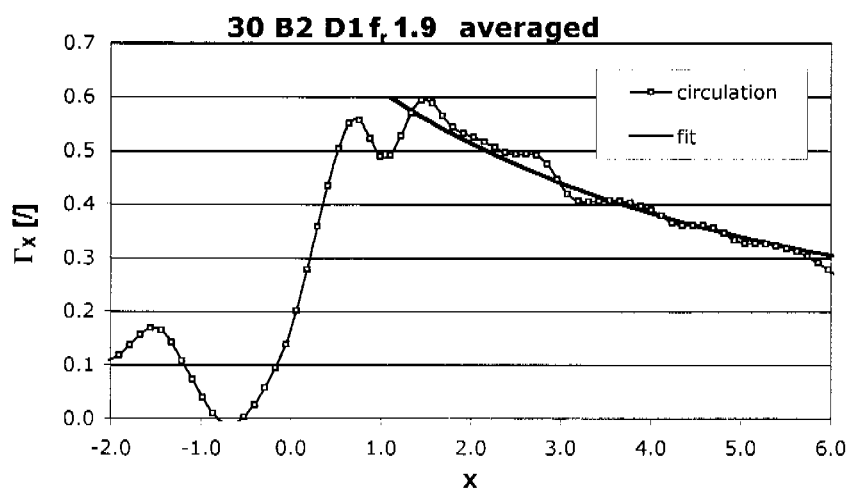**Figure 5.13:** average rate of mixing and fit with exponential function

Figure 5.14: axial circulation and fit with exponential function

It is worth noting from the above considerations, that the typical lengthscale L for both the circulation and the mixing rate are in the same order of $4d$, which is in the order of the length of the jet in the measurement domain. The only other feature of similar order in size is the boundary layer length. They both have origins at the location of coolant ejection.

The dissipation of the circulation and the rate of mixing most likely originate from different physical processes. The coolant jet diffuses all around its periphery: the process reduces the coolant concentration in the jet and increases it in the surroundings. The rate of mixing, however, will exponentially reduce to zero at infinity. The fully diffused state is a low uniform level across the whole flow.

The mixing process around the periphery of the jet has no effect on the circulation. The vorticity is diffused and will behave like the coolant concentration, but the circulation should not change. Instead the circulation is influenced by the viscous dissipation at the wall only. The coolant jet and its vorticity are concentrated near to the wall. The kidney vortices induce their strongest secondary flows under the jet against the wall. The boundary layer grows with a similar length to the jet, their origins are also similar in that the jet starts at the film hole exit, where the boundary layer is aggressively thinned due to the acceleration of the flow due to the potential field of the jet. The fully mixed out state for the circulation is zero. All the circulation is eventually destroyed by the friction at the wall. So the shear layers surrounding the jet dominate the rate of mixing and the circulation is dominated by the growth of the end wall boundary layer. The slight difference in the exponent may be related, in part to the differences in the effective origins of the two shear layers.

5.3 Conservation Equation of the Cooling Concentration

The conservation of cooling concentration derived from a control volume (as can be found in i.e. Batchelor [12]) takes the form of:

$$\frac{DCC}{Dt} = \kappa_D \nabla^2 CC$$

where $\dfrac{DCC}{Dt}$ is the substantial derivative of the cooling concentration. It expresses the rate of change of the coolant concentration on a fluid particle as it moves through the space. This term captures variation due to the unsteady nature of the

145

flow and also variation as the fluid particle convects through the spatial gradients of the coolant concentration. So the equation contains unsteadiness and convection:

$$\frac{DCC}{Dt} = \frac{\partial CC}{\partial t} + u\frac{\partial CC}{\partial x} + v\frac{\partial CC}{\partial y} + w\frac{\partial CC}{\partial z}$$

The unsteady term is neglected as the calculation of the unsteady term shows that it is more than an order of magnitude smaller than the smallest component of the convection term[1]. Furthermore, the considerations about the quasi steady behaviour support the negligence of this term for the present small amplitude of pulsation. This leaves the convective terms on the left hand side of the equation.

The constant κ_D is known as the 'coefficient of diffusion'. The group $\nabla^2 CC$ is the Laplacian operator of the coolant concentration, representing the diffusion of the coolant concentration into the control volume.

$$\nabla^2 CC = \frac{\partial^2 CC}{\partial x^2} + \frac{\partial^2 CC}{\partial y^2} + \frac{\partial^2 CC}{\partial z^2}$$

Substituting the coolant conservation equation with above relations leads to:

$$u\frac{\partial CC}{\partial x} + v\frac{\partial CC}{\partial y} + w\frac{\partial CC}{\partial z} = \kappa_D\left(\frac{\partial^2 CC}{\partial x^2} + \frac{\partial^2 CC}{\partial y^2} + \frac{\partial^2 CC}{\partial z^2}\right)$$

The resultant field of the diffusion coefficient κ_D expresses the detailed 3D resolved mixing process. The distribution of the diffusion coefficient is strongly influenced by the turbulence in the flow. The diffusion coefficient is closely related to the 'turbulent viscosity' as used in the momentum transport equations. There is a huge body of work on the modelling of turbulence and the aim is always to predict the distribution in space of the turbulent viscosity. The results should be of great interest to those who are interested in the CFD modelling of film cooling.

The separate components contributing to the partial differential equation above are analysed separately in an initial step. The convective terms that form the left hand side of the equation are illustrated at a XY plane $0.4d$ above the surface in the next figure in the left column. The corresponding velocity components are shown in the right column.

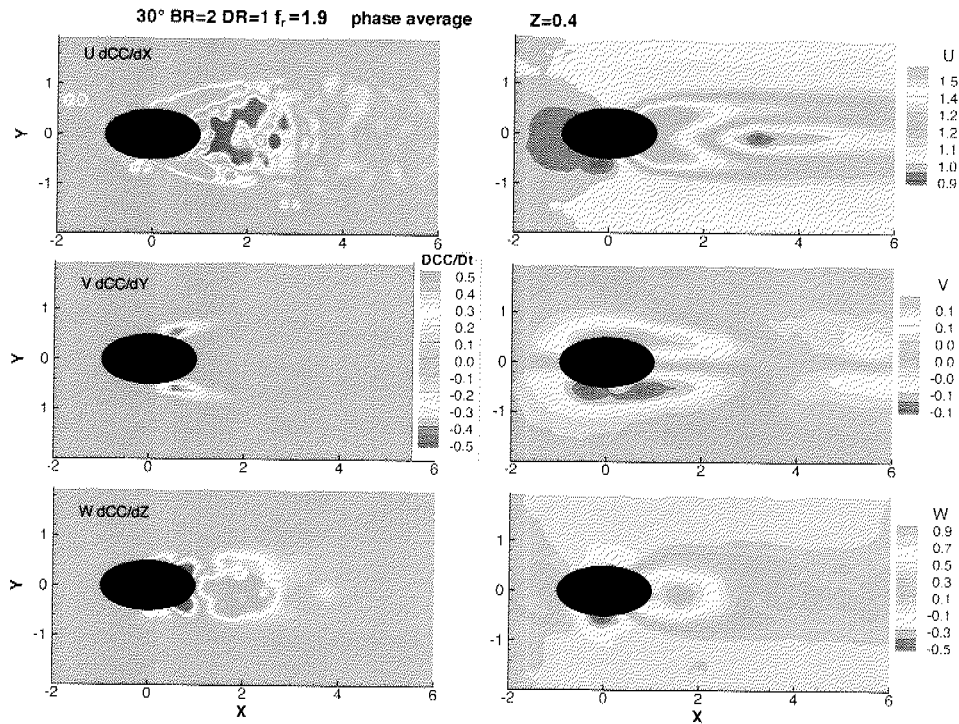
1. **order of** dCC/dt=0.01 **v's order of** v *dCC/dy=0.1

Figure 5.15: convective terms of the cooling concentration at Z=0.4

It is visible that the Y-component (in the middle plot, left) is small, originating from the comparably small lateral velocity component V (in the middle plot, right). The axial and the normal component of the convective term are much stronger, again related to the velocity components that are more than one order of magnitude greater. The extent in axial direction is small in this plane at Z=0.4.

The convective terms that form the left hand side of the equation are illustrated at a YZ plane downstream of the centre of the hole in the next 3 figures in the left column, again together with the respective velocity component in the right column. The pictures show planes at X=1.0, 2.0 and 4.0 to illustrate the decay of the convective term with axial distance from the cooling hole.
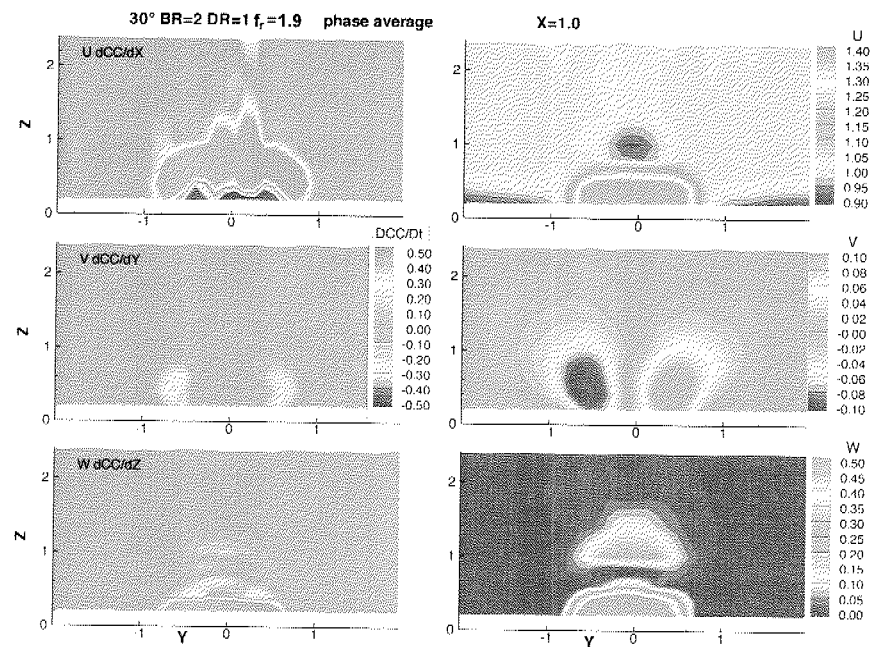
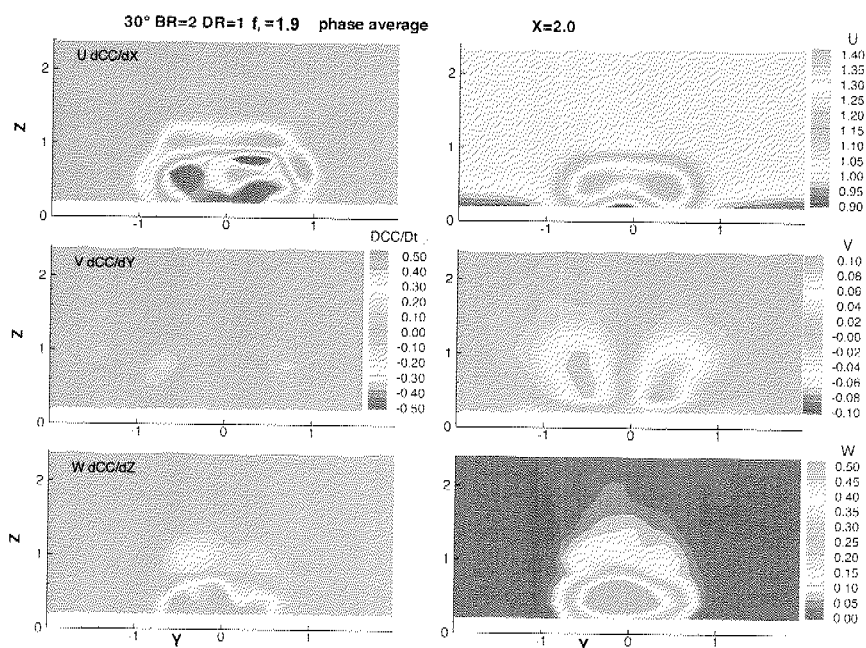**Figure 5.16:** convective terms of the cooling concentration at $X=1.0$

Figure 5.17: convective terms of the cooling concentration at $X=2.0$
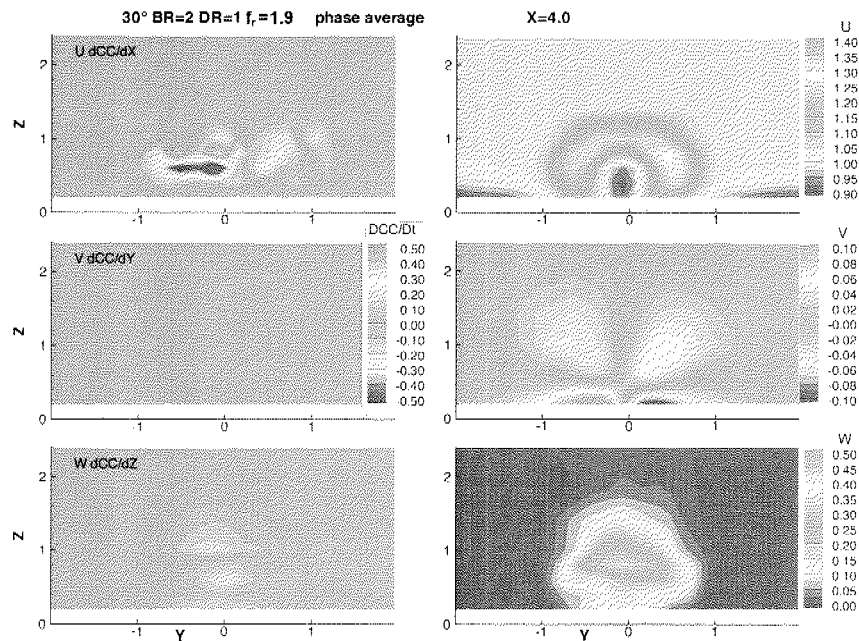
Figure 5.18: convective terms of the cooling concentration at X=4.0

The previous figures show clearly that the convective transport of cooling concentration is dominated by the axial component on the windward side of the jet. The vertical component does add to the overall level in the centre of the jet, while the lateral component is an order of magnitude smaller. The decay of the convective term happens quickly, at $X=4$ it is not of significant strength anymore.

The convective term in vertical direction is positive in the range $X=1.2$ to 2.5 i.e. convection is bringing coolant into this region. This could be the effect of the underside of the vortices bringing coolant down on the outside of the vortices and convecting upwards near the centreline. The action of the vortices entrains free-stream fluid in behind the jet and under it later on.

The same analysis of the right hand side of the partial differential equation shows a different behaviour. The diffusion terms that form the right hand side of the equation are illustrated at a XY plane $0.4d$ above the surface in Fig. 5.19.
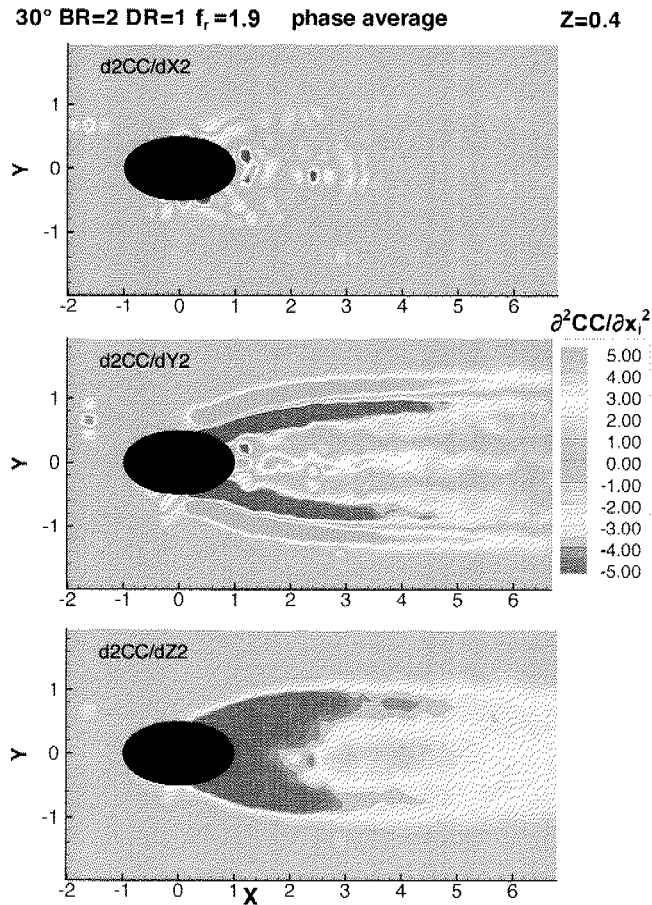
Figure 5.19: diffusion terms of the cooling concentration at Z=0.4

The above figure shows clearly that the diffusion in the axial direction is negligible. The lateral diffusion is strong at the outer mixing zone of the jet, and the vertical component is strong in the windward side of the jet.

The three diffusion terms that form the right hand side of the equation are illustrated at different YZ planes downstream of the centre of the hole in the next 3 figures. The axial distance from the centre of the hole is again $X=1.0$, 2.0 and 4.0 in the respective figures Fig. 5.20, Fig. 5.21 and Fig. 5.22. The evolution of the different terms with axial distance and the effect of diffusion is illustrated with this way of presentation. The cooling concentration is transported from blue to red regions via diffusion.

150

30° BR=2 DR=1 f$_r$=1.9   phase average   X=1.0
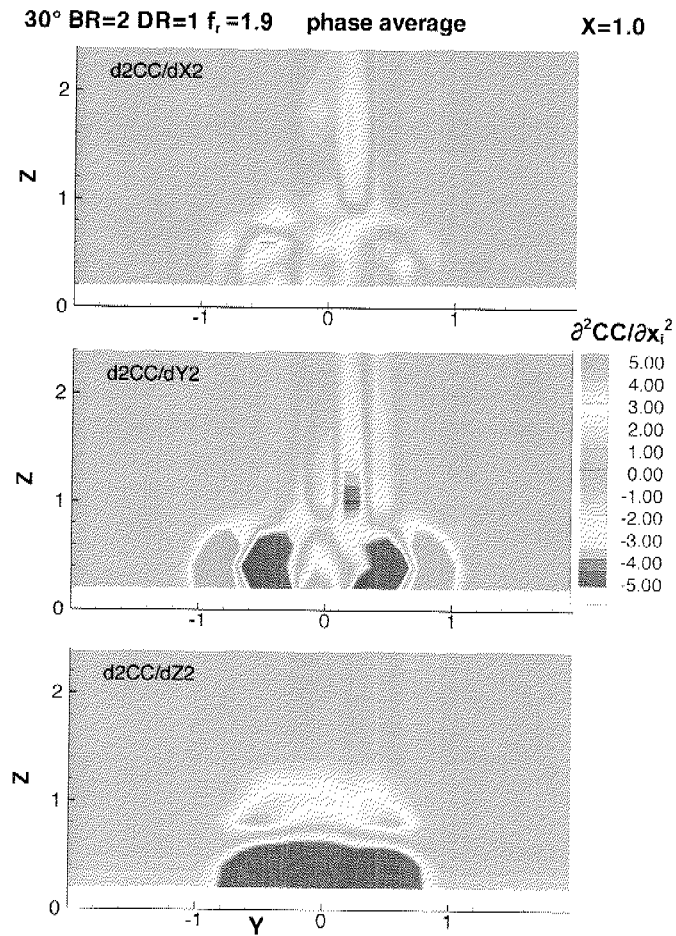
Figure 5.20: diffusion terms of the cooling concentration at *X=1.0*

The axial and the lateral components of the *CC* diffusion feature vertical lines from *Z=0.8* all the way to the top of the plot. These are artifacts introduced by reflection in the vicinity of the trailing edge of the cooling hole.
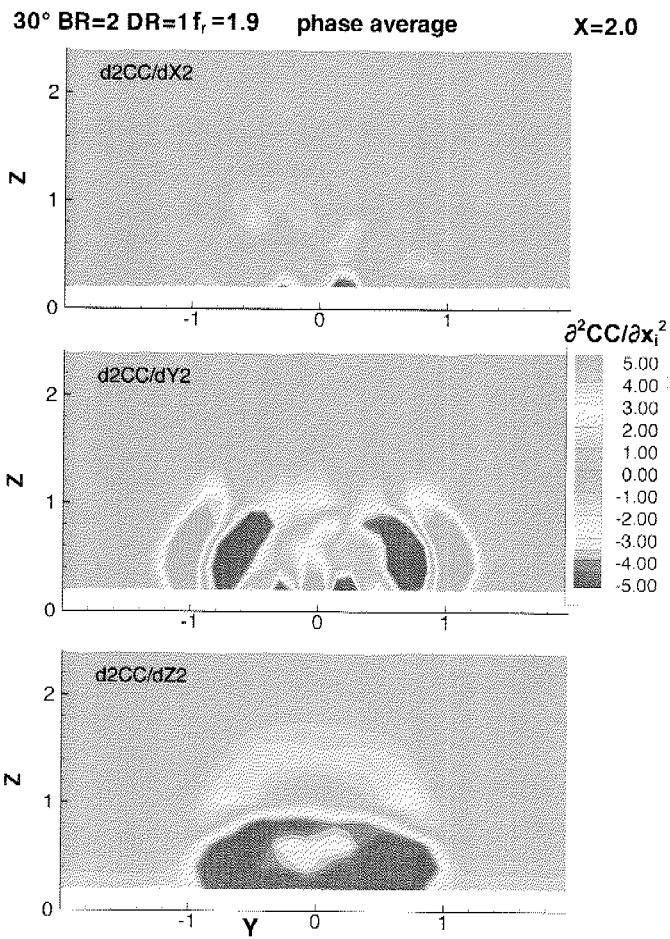
Figure 5.21: diffusion terms of the cooling concentration at X=2.0
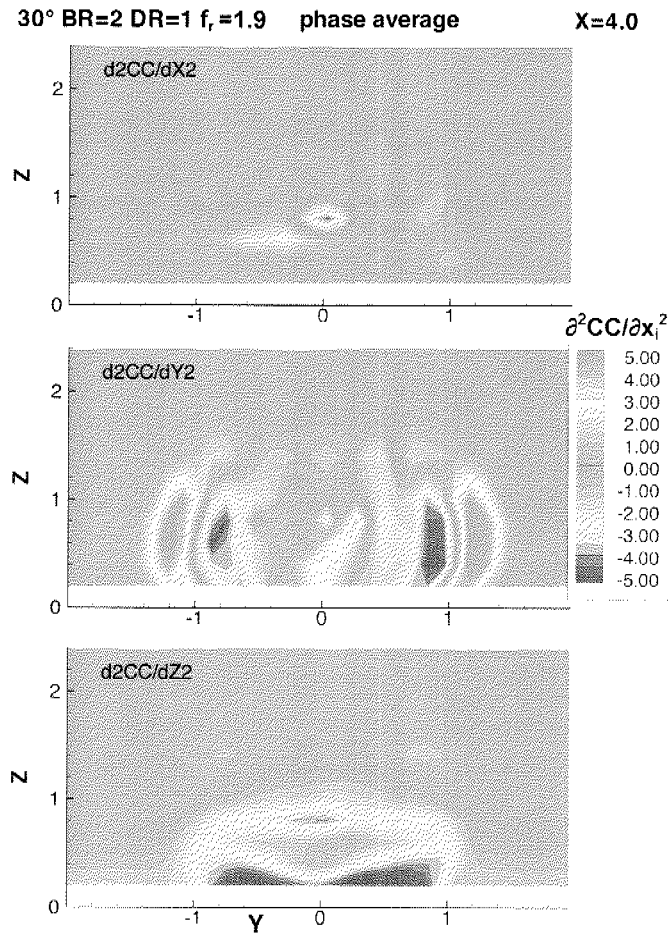
Figure 5.22: diffusion terms of the cooling concentration at X=4.0

The axial component of the flux term is small compared to the lateral and the vertical ones. The lateral term shows 4 distinct regions in the outer mixing zone of the jet, and the vertical term is dominant on the windward side.

A positive Laplacian shows where the net effect of mixing is to increase the coolant concentration. The reverse is true where it is negative.

The assumption of zero streamwise mixing is quite common in CFD e.g. early Spalding parabolic solvers. The previous plots support this as a good assumption. The d^2CC/dZ^2 variable shows that mixing is significant on the exposed windward side of the jet, the fluid is experiencing a strong inward diffusion in this area.

The previous illustrations show how the partial differential equation can be simplified by neglecting the terms that do not have a strong influence. This are the convective terms in Y and in Z direction and the net flux term in axial direction:

$$u\frac{\partial CC}{\partial x} + v\cancel{\frac{\partial CC}{\partial y}} + w\cancel{\frac{\partial CC}{\partial z}} = K_D\left(\cancel{\frac{\partial^2 CC}{\partial x^2}} + \frac{\partial^2 CC}{\partial y^2} + \frac{\partial^2 CC}{\partial z^2}\right)$$

$$\Rightarrow u\frac{\partial CC}{\partial x} = K_D\left(\frac{\partial^2 CC}{\partial y^2} + \frac{\partial^2 CC}{\partial z^2}\right)$$

It can be stated that with good approximation that the convective term in axial direction is balanced by the net flux terms in lateral and normal direction.

Adding the three components for both sides of the PDE results in the following set of figures. The left hand side, representing the total convective transport of CC is always shown on top of each figure. The bottom picture represents the diffusion term of CC. Two XY planes at $Z=0.4$ and 1.0 are shown in Fig. 5.23 and Fig. 5.24, followed by two YZ planes at $X=1.0$ and 2.0 in Fig. 5.25 and Fig. 5.26.

Figure 5.23: left- and right- hand side of the partial differential equation at $Z=0.4$

154
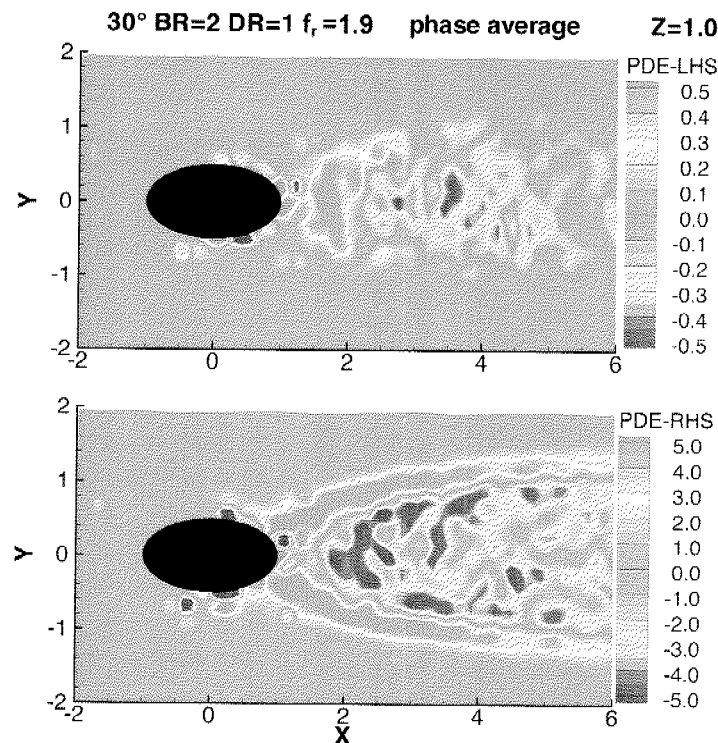
Figure 5.24: left- and right- hand side of the partial differential equation at Z=1.0

The right hand side is dominated by a strong negative CC diffusion in the core part of the 2 kidney vortices, surrounded by a narrow region of positive CC diffusion in the outer mixing region of the jet. The region in between the counter-rotating vortex pair shows a slightly positive CC diffusion.

The left hand side shows a strong positive convection of cooling concentration on the windward side of the jet followed by a small but distinct negative ring in the centreline. No clear pattern is distinguishable further downstream.

The magnitude of the CC flux is one order greater than the convective part. The diffusion coefficient is the quotient of these two sides, resulting in a value of the order of 0.1. This is very large value compared to typical viscosity values[1]. Mathematically, this poses a problem in the region where no cooling flow is present. Here all the gradients are either very close to zero or affected by reflection (i.e. the point above and upstream of the cooling hole). Furthermore, both sides change sign in the cooling flow region, which potentially results in negative diffusion coefficients.

1. $\mu_{laminar} \sim 2 \cdot 10^{-5}$ $\mu_{turbulent} \sim 2 \cdot 10^{-2}$
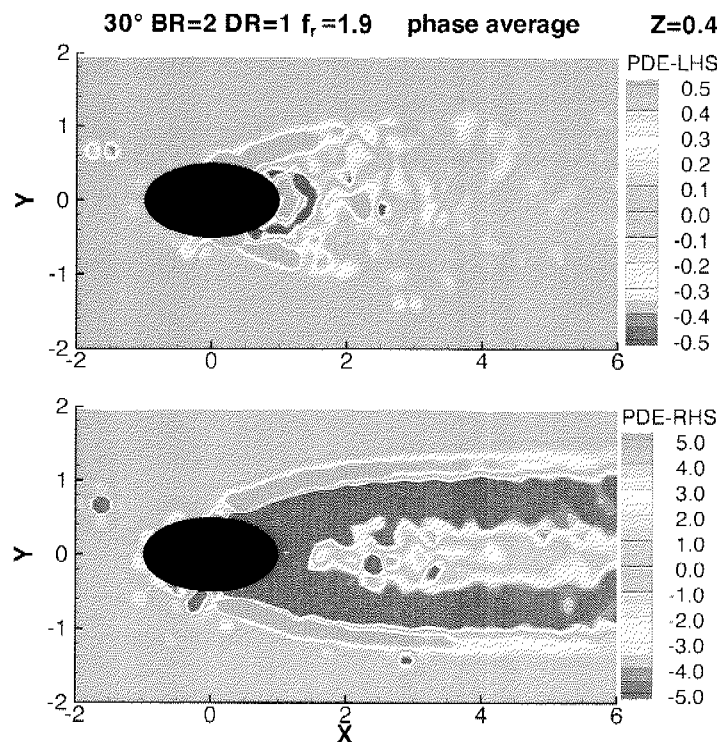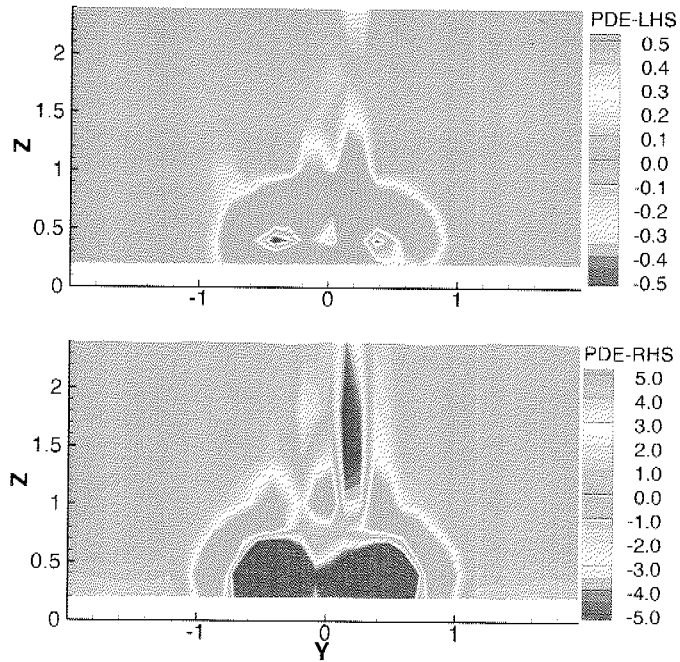
Figure 5.25: left- and right- hand side of the partial differential equation at X=1.0
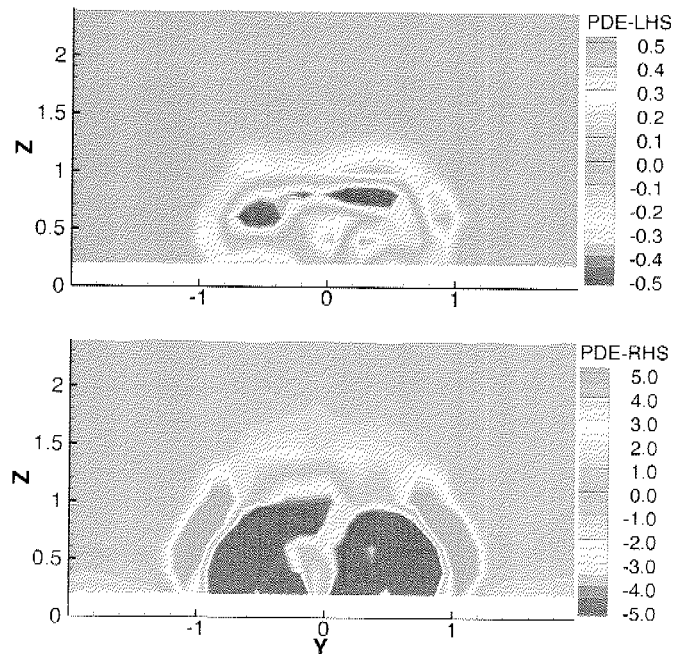
Figure 5.26: left- and right- hand side of the partial differential equation at X=2.0

156

The derived diffusion coefficient is shown in the following figures 5.27 and 5.28. The flow vectors in each plane are included in the figures to indicate the flow structure.
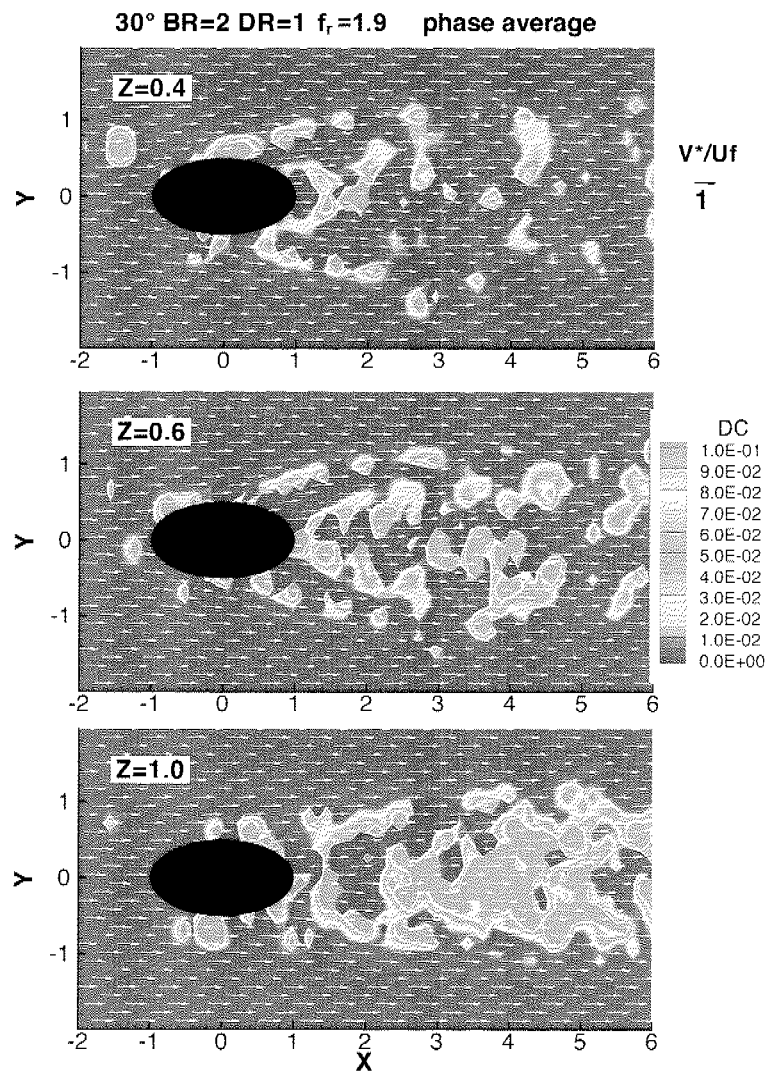
Figure 5.27: diffusion coefficient at different XY-planes
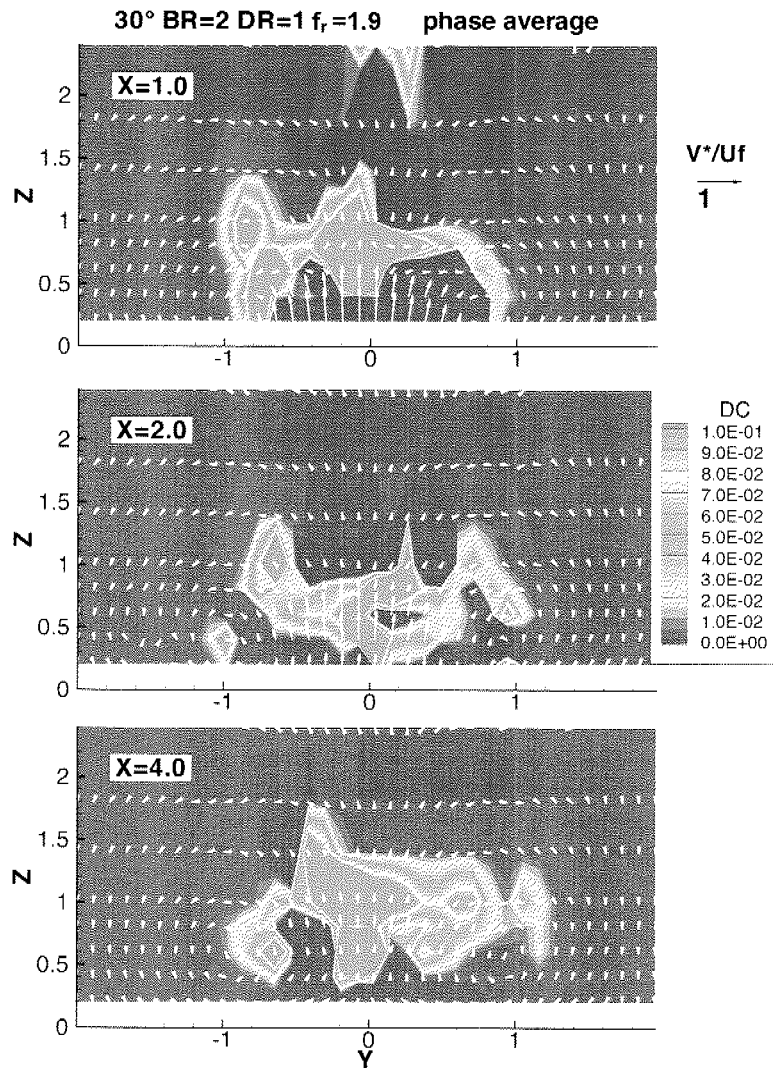
Figure 5.28: diffusion coefficient at different YZ-planes

It is obvious from the above figures that this last step of the analysis is pushing to the limits of the data quality. The spatial resolution is rough and the influence of the reflections is clearly visible. Higher sample number and higher spatial resolution in combination with appropriate filtering techniques would help lessen the problem.

On the top-side of the coolant jet X convection and net mixing in the Z direction are both causing the coolant concentration to increase. The length scale of the two

effects is quite different, however. The convection terms only extend up to about $Z=1.3$ where the net mixing flux extends as high as $Z=1.8$. The convection rate peaks at about 0.5 where the net effect of mixing peaks at around 5.0, implying a diffusion coefficient of about 0.1.

On the sides of the coolant jet convection is again causing an increase in coolant concentration. This is mostly due to convection in the X direction but the convection in the Y direction reduces this effect due to lateral spreading of the vortices at around $Z=0.8$ and weakly increases at around $Z=0.4$. In contrast to this the diffusion term d^2CC/dY^2 shows an amazingly strong result. There is strong diffusion across the shear layers around the outside of the jet and vortices. There is also diffusion on small length-scales near the centreline. It can be assumed that the red region here is a slug of freestream fluid (i.e. of low CC), which has been entrained into the middle of the vortices and is now receiving coolant as it mixes with the jet vortex fluid. In Fig. 5.10 there is a 'blob' of lower CC (green) surrounded by higher CC yellow with a short length scale. The size of this zone is considerably smaller than the main kidney vortex system forming above it.

6. CONCLUSION

A summary of the key findings within this thesis is given in the following points. The interpretation of those results suggests additional work to be done in the near future.

6.1 Facility and CFD-Modelling

It has been shown that the new facility provides high quality data of the near hole flow structure of film cooling. The test rig behaved in a reliable and predictable fashion which facilitated the recording of a large amount of velocity data. The accuracy of both the measurement system and the possibility to adjust and keep a desired flow condition was the key to establish a valuable database for calibration of a film cooling model. This model was implemented in a software code and proved successful in the numerical prediction of heavily film cooled turbine blades while requiring little additional CPU time.

6.2 Film Cooling Flow Structure and Mixing

The high resolution of the 3D PIV data allowed visualization of some detailed flow physics associated with film cooling in the near hole region. This study included a range of parameters: streamwise hole angle, blowing ratio, density ratio, momentum flux ratio and pulsation frequency. The results confirmed the classical phenomena of the formation of the kidney vortex pair and jet lift-off at higher momentum flux ratios. The detailed flow structure of near hole film cooling has revealed highly interesting phenomena.

The assumption of quasi steady flow during pulsating coolant injection has been investigated in detail. The final conclusion regarding the validity and limits of this assumption is based on results from the velocity field, the centre-line trajectory of the coolant jet and the streamwise circulation. For a low amplitude $\tilde{BR} < 0.2$ and reduced frequencies below 1.88 the pulsation of the injectant can be described as quasi steady with very good accuracy. This is valid for the investigated range between two hole diameters upstream and six diameters downstream of the cooling hole. The quasi steady postulate has limited validity for a high amplitude of pulsation $\tilde{BR} > 0.5$. The phase averaged flow phenomena correspond reasonably well to the respective steady ones. The phase resolved flow does display unsteady effects that are not captured with quasi steady modelling. This is due to periodic lift-off and re-attachment of the jet.

One of the main conclusions from this section was that the swapping of the pulsating flow regime from the main flow in a real turbine environment to the cooling flow in this research facility is valid for low pulsation amplitude $\tilde{BR} < 0.2$ as a quasi steady behaviour is present.

The 3D vortical structure as a function of different flow parameters was exposed. The vorticity reveals the expected signature of the kidney vortices and also suggests artefacts from horseshoe vortex activity for high momentum flux ratio and unsteady vortex shedding from the sides of the jet. These mechanisms will augment mixing and may reduce the film cooling effectiveness.

The peak of the streamwise circulation showed a strong dependency on the momentum flux ratio, supporting its suitability as descriptive parameter for film cooling purposes. Surprisingly the streamwise injection angle shows no influence on the peak of the streamwise circulation.

The complex behaviour of the boundary layer in the vicinity of the cooling hole was investigated and linked to the entrainment of low momentum fluid into the kidney vortex pair. The PIV data showed that the incoming flat plate boundary layer is thinned by the entrainment of the coolant jets, starting at the leading edge of the hole. This effect gets stronger as the momentum flux ratio is increased. This is expected to increase the mean heat transfer coefficient in this region.

The cooling concentration was introduced as a new parameter to describe the mixing between coolant and main flow. This novel parameter has the potential to support the numerical prediction of the temperature field in a gas turbine.

The spatially resolved rate of mixing, derived from the cooling concentration,

shows the zone of highest mixing activity on the lateral- and the under-side of the jet. It was shown that the decay of the rate of mixing and the circulation are driven by the flow phenomena with a similar typical length-scale in the order of 4 hole diameters. This implies a generally slow dissipation of the jet. The shear layers surrounding the jet dominate the decay of the rate of mixing while the decay of the circulation is dominated by the growth of the end wall boundary layer.

The respective conservation equation was utilized to analyse the relevant components with impact on the alteration of the diffusion coefficient. The variation of this parameter is largely unknown but of relevance for the simulation of mixing.

Overall, it can be concluded from the different researched aspects that the momentum flux ratio is better suited to describe the film cooling structure than the blowing ratio. The vortical and the general flow structure, in particular the streamwise circulation and the jet trajectory showed systematic dependency on the momentum flux ratio.

6.3 Suggestions for Future Work

We now have a large body of experimental data characterizing film cooling to provide empirical input for film cooling modelling. To extend that data base the respective flow field associated with the variation of turbulence intensity, lateral hole angle and shape of the cooling hole other than cylindrical is suggested to be recorded.

Measurements of the far hole flow field will provide insight into the impact of near hole effects on the overall film cooling performance and establish the extent of the quasi steady behaviour.

It is further suggested to quantify the surface heat flux and heat transfer coefficient. This will lead to novel insight into the interconnection between flow, mixing and thermal phenomena. In combination with systematic investigation of hole geometry and shape this will give valuable knowledge to film cooling designers and further the understanding about which hole design is better and why.

Measurements with a strong contrast of seeding density between main and cooling flow will allow a systematic investigation of the mixing. A greater number of

samples will reduce the noise of the results and could lead to the successful determination of a 3D resolved diffusion coefficient. This again will provide very useful data for modelling and simulation of a cooled turbine stage.

One suggestion surfaces from this work regarding the design of film cooling holes. It is shown that the momentum flux ratio is driving the circulation, which again determines the vorticity. The vorticity is linked to the mixing between cooling jet and main flow, while less mixing will results in a better cooling effectiveness. The design aim is to use as little coolant as possible to achieve the desired cooling effect. Therefore it can be stated, that the aim in cooling design should be to control the momentum flux ratio to keep it as low as possible. Fanshaped cooling holes have that effect by increasing the cross-section of the cooling flow at the exit of the hole.

NOMENCLATURE

ROMAN

b	Ratio of particle size and wavelength of light
c_d	Discharge coefficient
c_p	Heat capacity
c_f	Skin friction coefficient
d	Hole diameter, distance
f	Frequency
f_r	Reduced frequency
g	Isotropic transport coefficient
h	Heat transfer coefficient
k	Thermal diffusivity
l	Length of the hole pipe
$\dot{m}$	Mass flow rate
n	Particle size range
p	Pressure
$\dot{q}$	Heat transfer rate
s	Pitch distance between two holes
t	Time
A	Area
C	Cross section
I	Laser intensity
L	Length
LI	Light intensity
M, N	Number, count
$\vec{M}$	Rate of mixing
P	Power
R	Radial Distance, Error
S	Object to image scaling factor
T	Temperature
U,V,W	Velocity components
V*	Velocity magnitude YZ-plane

X	Axial (streamwise) coordinate
Y	Lateral coordinate
Z	Vertical coordinate

GREEK

α	Streamwise injection angle
β	Lateral injection angle, diameter ratio
δ^*	Displacement thickness
ε	Expansion coefficient
ϕ	Cross correlation function
Γ	Circulation
φ	Flow angle
κ	Isentropic exponent
κ_D	Diffusion coefficient
λ	Wave length of light
μ	Dynamic viscosity
ν	Kinematic viscosity
π	Pi
θ	Momentum thickness
ρ	Density
σ	Standard deviation
τ	Shear stress
ω	Angular velocity
ω_x	Streamwise vorticity
ω_y	Lateral vorticity
ω_z	Normal vorticity
ω^*	Non-dimensional vorticity

DIMENSIONLESS NUMBERS

BR	Blowing ratio
CC	Cooling concentration
ETR	Entrainment coefficient
DR	Density ratio
H	Shape factor
IR	Momentum flux ratio
M	Mach number
Pr	Prandtl number
Re	Reynolds number
St	Strouhal number
Tu	Turbulence intensity

INDICES

a	Adiabatic condition
c	Coolant fluid
f	Free stream fluid, free stream condition
max	Maximum
min	Minimum
p	Particle
r	Recovery condition, radial component
s	Static condition
t	Tangential component
x	Axial component / direction
y	Lateral component / direction
z	Vertical component / direction
0	Total condition
~	Unsteady, pulsating
−	Mean, average

ABBREVIATIONS

A/D	Analoge-digital
BSM	Beugungsspektrometer
CCD	Charged coupled device
CFD	Computerized fluid dynamics
DEHS	Dioctylsebacat
DLT	Direct linear transformation
DAT	Dot area tolerance
FFT	Fast Fourier transformation
FRAP	Fast response aerodynamic probe
FSO	Full scale output
LHS	Left hand side
LSM	Labor für Strömungsmaschinen
PC	Personal computer
PIV	Particle image velocimetry
RHS	Right hand side
TFG	Thin film gauge

166

REFERENCES

[1] Abhari, R. S., (1996) "Impact of Rotor-Stator Interaction on Turbine Blade Film Cooling." ASME Journal of Turbomachinery, 118:123-133.

[2] Abhari, R.S., and Epstein, A.H., (1994) "An experimental Study of Film Cooling in a rotating Transonic Turbine." ASME Journal of Turbomachinery, 116:63-70.

[3] Abhari, R. S., Guenette, G. R., Epstein, A. H., and Giles, M. B., (1992) "Comparison of Time-Resolved Turbine Rotor Blade Heat Transfer Measurements and Numerical Calculations." Journal of Turbomachinery, 114:818-827.

[4] Abramovich, G.N., (1963) "The Theory of turbulent Jets." Cambridge, MA: The MIT Press.

[5] Adamczyk, J.J., (1985) "Model equation for simulating flows in multistage turbomachinery." ASME paper 85-GT-220.

[6] Adrian, R.J., (1991) "Particle-imaging techniques for experimental fluid mechanics." Annual Review of Fluid Mechanics, 23:261-304.

[7] Andreopoulus, J., Durst, J., Zaric, L., Jovanovic, J., (1984) "Influence of Reynolds Number on Characteristics of Turbulent Wall Boundary Layers." Experiments in Fluids, 2: 7-16.

[8] Ardey, S., Wolff, S., Fottner, L., (2000) "Turbulence Structures of Leading Edge Film Cooling Jets." Proceedings of the ASME Turbo Expo 2000, 2000-GT-255, Munich, Germany.

[9] Arts, T., Camci, C., (1985) "Short Duration Measurements and Numerical Simulation of Heat Transfer along the Suction Side of a Film-Cooled Gas Turbine Blade." Proceedings of the ASME Turbo Expo 1985, 85-GT-111.

[10] Barlow, D.N., Kim, Y.W., (1995) "Effects of Surface Roughness on Local Heat Transfer and Film Cooling Effectiveness." Proceedings of the ASME Turbo Expo 1995, 95-GT-14, Houston, Texas.

[11] Basset, A., (1910) "On the descent of a sphere in a viscous fluid." Q. J. Pure and Appl. Math. 41: 369–381.

[12] Batchelor, G.K., (1967) " An Introduction to Fluid Dynamics." Cambridge University Press, Cambridge, UK.

[13] Bell, C.M., et al., (1999) "Film cooling subject to bulk flow pulsations:

effects of blowing ratio, freestream velocity, and pulsation frequency." International Journal of Heat and Mass Transfer, 42(23): 4333-4344.

[14] Bernsdorf, B., Rose, M.G., Abhari, R.S., (2005) "Modelling of Film Cooling - Part I: Experimental Study of Flow Structure." Proceedings of the ASME Turbo Expo 2005. GT2005-68783, Reno, Nevada, USA.

[15] Bons, J.P., Rivir, R.B., MacArthur, C.D., Prestian, D.J., (1995) "The Effect of Unsteadiness on Film Cooling Effectiveness." AIAA proceedings of the 33rd Aerospace Sciences Meeting, paper 95-0306.

[16] Bons, J. P., MacArthur, C. D., Rivir, R. B., (1996) "The effect of high freestream turbulence on film cooling effectiveness." Journal of Turbomachinery-Transactions of the ASME, 118(4): 814-825.

[17] Brandt, H., Ganzert, W., Fottner, L., (2000) "A presentation of detailed Experimenatl Data of a Suction Side Film Cooled Turbine Cascade." Proceedings of the ASME Turbo Expo 2000, 2000-GT-296, Munich, Germany.

[18] Burdet, A., Abhari, R. S., (2005) "The Modelling of Film Cooling - Part II: Model for use in 3D CFD." Proceedings of the ASME Turbo Expo 2005, GT2005-68780, Reno, Nevada, USA.

[19] Burdet, A., (2005) "A Computationally Efficient Feature-Based Jet Model for Prediction of Film-Cooling Flows." PhD-Thesis 16163, ETH Zurich.

[20] Camci, C., (1989) "An Experimental and Numerical Investigation of Near Cooling Hole Heat Fluxes on a Film-Cooled Turbine Blade." Journal of Turbomachinery-Transactions of the ASME, 111: 63-70.

[21] Cebeci, T., Bradshaw, P., (1984) "Physical and Computational Aspects of Convective Heat Transfer." Springer-Verlag, New York.

[22] Cho, H.H. Goldstein, R.J., (1995) "Heat (Mass) Transfer and Film-Cooling Effectiveness with Injection through Discrete Holes within Holes and on the Back Surface." Journal of Turbomachinery-Transactions of the ASME, 1995. 117(3): 440-450.

[23] Cho, H. H., Goldstein, R. J., (1995) "Heat (Mass) Transfer and Film-Cooling Effectiveness with Injection through Discrete Holes on the Exposed Surface." Journal of Turbomachinery-Transactions of the ASME, 117(3): 451-460.

[24] Dantec Dynamics, (2002) "Flow Manager Software and Introduction to PIV Instrumentation." Dantec Dynamics A/S.

[25] Dring, R.P., Blair, M.F., Joslyn, H.D., (1980) "An Experimental Investigation of Film Cooling on a Turbine Rotor Blade." Journal of Engineering for Power, 102:81-87.

[26] Du, H., Han, J.C., Ekkad, S.V., (1998) "Effect of Unsteady Wake on Detailed Heat Transfer Coefficients and Film Effectiveness Distributions for a Gas Turbine Blade." ASME Journal of Turbomachinery, 120: 808-817.

[27] Duncan, W.J., Thom, A.S., Young, A.D., (1970) "Mechanics of Fluids." Edward Arnold Ltd., London.

[28] Dunn, M. G., (1990) "Phase and Time Resolved Measurements of Unsteady

Heat Transfer and Pressure in a Full-Stage Rotating Turbine." Journal of Turbomachinery, 112, 531-538.

[29] Dunn, M. G., Hause, A., (1982) "Measurement of Heat Flux and Pressure in a Turbine Stage." Journal of Engineering for Power, 104, 215-223.

[30] Dunn, M.G., Seymour, P.J., Woodward, S.H., George, W.K., Chupp, R.E., (1989) "Phase resolved Heat-Flux Measurements on the Blade of a full Scale rotating Turbine.", Journal of Turbomachinery, 111: 8-19.

[31] Eads, T. A., (1992) "Shock Tube Study of the Effects of Large Density Differences and Blowing Ratio on Heat Transfer to a Film-Cooled Flat Plate." MSc, Wright-Patterson AFB, Ohio School of Engineering.

[32] Eckert, E.R.G., (1984) "Analysis of Film Cooling and Full Coverage Film Cooling of Gas-Turbine Blades." Journal of Engineering for Gas Turbines and Power-Transactions of the ASME, 106(1): 206-213.

[33] Ekkad, S. V., Zapata, D., Han, J. C., (1997) "Heat transfer coefficients over a flat surface with air and CO2 injection through compound angle holes using a transient liquid crystal image method." Journal of Turbomachinery-Transactions of the ASME, 119(3): 580-586.

[34] Ekkad, S.V., Zapata, D., Han, J.C., (1997) "Film effectiveness over a flat surface with air and CO2 injection through compound angle holes using a transient liquid crystal image method." Journal of Turbomachinery-Transactions of the ASME, 119(3): 587-593.

[35] Epstein, A. H., Guenette, G. R., Norton, R. J. G., Yuzhang, C. (1986) "High frequency response heat flux gauge." Review of Scientific Instruments, Vol. 75, No. 4: 81-87.

[36] Eriksen, V.L., Goldstein, R.J., (1974) "Heat-Transfer and Film Cooling Following Normal Injection through a Round Hole." Journal of Engineering for Power-Transactions of the ASME, 96(4): 329-334.

[37] Ethridge, M.I., Cutbirth, J.M., Bogard, D.G., (2000) "Scaling of Performance for Varying Density Ratio Coolants on an Airfoil with Strong Curvature and pressure Gradient Effects." Proceedings of the ASME Turbo Expo 2000, 2000-GT-239, Munich, Germany.

[38] Forth, C. J. P., Loftus, P. J., Jones, T. V., (1985) "Effect of Density Ratio on the Film-Cooling of a Flat Plate." AGARD, CP 390.

[39] Foster, N.W., Lampard, D., (1980) "The Flow and Film Cooling Effectiveness Following Injection through a Row of Holes." Journal of Engineering for Power-Transactions of the ASME, 102(3): 584-588.

[40] Ganzert, W., Hildebrandt, T., Fottner, L., (2000) "Systematic Experimental and numerical Investigantion on the Aerothermodynamics of a film cooled turbine cascade with variations of the cooling hole shape; Part I: Experimental Approach." Proceedings of the ASME Turbo Expo 2000, 2000-GT-295, Munich, Germany.

[41] Giang, T. T. L., (1999) "Effects of Unsteady Cooling Flow on Heat Transfer to a Film-Cooled Flat Plate." MSc, The Ohio State University, Columbus.

169

[42] Gogineni, S., Goss, L., Pestian, D., Rivir, R., (1998) "Two-colour digital PIV employing a single CCD camera." Experiments in Fluids, 25(4), 320-328.

[43] Goldstein, R. J., Cho, H. H., (1995) "A Review of Mass-Transfer Measurements Using Naphthalene Sublimation." Experimental Thermal and Fluid Science, 10(4): 416-434.

[44] Goldstein, R. J., Eckert, E. R. G., Burggraf, F., (1974) "Effects of Hole Geometry and Density on 3-Dimensional Film Cooling." International Journal of Heat and Mass Transfer, 17(5), 595-607.

[45] Goldstein, R. J., Jin, P., (2000) "Film Cooling Downstream of a Row of Discrete Holes with Compound Angle." Proceedings of the ASME Turbo Expo 2000, 1-10.

[46] Goldstein, R.J., Jin, P., Olson, R.L., (1999) "Film cooling effectiveness and mass heat transfer coefficient downstream of one row of discrete holes." Journal of Turbomachinery-Transactions of the ASME, 121(2): 225-232.

[47] Greitzer, E.M., Tan, C.S., Graf, M.B., (2004) "Internal Flow." Cambridge University Press, Cambridge, UK.

[48] Gritsch, M., Schulz, A., Wittig, S., (1998) "Adiabatic Wall Effectiveness Measurements of Film Cooling Holes with Expanded Exits." ASME Journal of Turbomachinery, 120: 549-556.

[49] Gritsch, M., Schulz, A., Wittig, S., (1998) "Heat Transfer Coefficient Measurements of Film Cooling Holes with Expanded Exits." ASME paper No. GT98-GT-28.

[50] Guenette, G. R., Epstein, A. H., Giles, M. B., Haimes, R., (1989) "Fully scale Transonic Turbine Rotor Heat Transfer Measurements." ASME Journal of Turbomachinery, 111, 1-7.

[51] Haven, B.A., Yamagata, D.K., Kurosaka, M., Yamawaki, S., Maya, M., (1997) "Anti-Kidney pair of Vortices in Shaped Holes and their Influence on Film Cooling Effectiveness." Proceedings of the ASME Turbo Expo 1997, 97-GT-45, Orlando, Florida, USA.

[52] Hawthorne, W.R., (1974) "Secondary Vorticity in Stratified Compressible Fluids in Rotating Systems." Cambridge University Engineering Department, CUED/A-Turbo/TR 63.

[53] Hay, Y., Lampard, D., (1995) "The Discharge Coefficient of Flared Flim Cooling Holes." Proceedings of the ASME Turbo Expo 1995, 95-GT-15, Houston, Texas.

[54] Heidmann, J.D., Lucci, B.L., Reshotko, E., (1997) "An Experimental Study of the Effect of Wake Passing on Turbine Blade Film Cooling." Proceedings of the ASME Turbo Expo 1997, Orlando, Florida, USA.

[55] Hildebrandt, T., Ganzert, W., Fottner, L., (2000) "Systematic Experimental and numerical Investigantion on the Aerothermodynamics of a film cooled turbine cascade with variations of the cooling hole shape; Part II: Numerical Approach." Proceedings of the ASME Turbo Expo 2000, 2000-GT-298, Munich, Germany.

170

[56] Hinze, J. O., (1959) "Turbulence." McGraw-Hill Book C. Inc., New York.

[57] Hoffs, A., Drost, U., Bölcs, A., (1997) "An Investigation of Effectiveness and Heat Transfer on a Showerhead-Cooled Cylinder." Proceedings of the ASME Turbo Expo 1997, 97-GT-69, Orlando, Florida.

[58] Honami, S., Shizawa, T., Uchiyama, A., (1994) "Behaviour of the Laterally Injected Jet in Film-Cooling - Measurements of Surface-Temperature and Velocity / Temperature Field within the Jet." Journal of Turbomachinery-Transactions of the ASME, 116(1), 106-112.

[59] Høst-Madsen, A., McCluskey, D.R., (1994) "On the Accuracy and Reliability of PIVmeasurements." Proceedings of the Seventh International Symposium on Applicationsof Laser Techniques to Flow Measurements, Lissbon, 1994.

[60] Hütte - Grundlagen der Ingenieurwissenschaften, 29th edition, 1989, Springer Verlag.

[61] Jung, I.S., Lee, J.S., Ligrani, P.M., (2001) "Effects of Bulk Flow Pulsation on Film Cooling With Compound Angle Holes: Heat Transfer Coefficient Ratio and Heat Flux Ratio." Proceedings of the ASME Turbo Expo 2001,2001-GT-0129, New Orleans, Louisiana, USA.

[62] Jung, I.S., Lee, J.S., (1998) "Effect of Bulk Flow Pulsations on Film Cooling from spanwise oriented Holes." Proceedings of the ASME Turbo Expo 1998, 98-GT-211, Stockholm, Sweden.

[63] Keane, R.D., Adrian, R.J., (1991) "Theory of Cross-Correlation Analysis of PIV Images." Applied Scientific Research, vol. 49:191–215.

[64] Kercher, D.M., (1998) "A Film-Cooling CFD Bibliography: 1971-1996." International Journal of Rotating Machinery, vol. 4: 61-72.

[65] Kerrebrock, J.L., (1992) "Aircraft Engines and Gas Turbines." The MIT Press, Cambridge, Massachusetts.

[66] Lee, J.S., Jung, I.S., (2002) "Effect of Bulk Flow Pulsations on Film Cooling with Compound Angle Holes." International Journal of Heat and Mass Transfer, 45(2002):113-123.

[67] Le Grivèe, E., (1978) "Mixing Process Induced by the Vorticity Associated with the Penetration of a Jet into a Cross Flow." Journal of Engineering for Power, 100.

[68] Ligrani, P. M., Bell, C. M., (2001) "Film Cooling Subject to Bulk Flow Pulsations: Effects of Density Ratio, Hole Length-to-Diameter Ratio, and Pulsation Frequency." International Journal of Heat and Mass Transfer, 44(10), 2005-2009.

[69] Ligrani, P. M., Saumweber, C., Schulz, S., Wittig, S., (2001) "Shock wave - Film Cooling Interactions in Transonic Flows." Journal of Turbomachinery-Transactions of the ASME, 123(4), 788-797.

[70] Ligrani, P.M., Subramanian, C.S., Coumes, T.M., Greco, F.J., Koth, H., longest, J.M., (1992) "Study of the Imposition of Bulk Flow Pulsations on Plane Channel Flow at Moderate Stokes Numbers." Experimental Thermal and Fluid Science, 5:145-161.

[71] Ligrani, P.M., Gong, R., Cuthrell, J.M., (1997) "Bulk Flow Pulsations and Film Cooling: Flow Structure Just Downstream of the Holes." Journal of Turbomachinery-Transactions of the ASME,119(3): 568-573.

[72] Ligrani, P.M., et al., (1996) "Bulk Flow Pulsations and Film Cooling 1. Injectant Behavior." International Journal of Heat and Mass Transfer, 39(11): 2271-2282.

[73] Ligrani, P.M., et al., (1996) "Bulk Flow Pulsations and Film Cooling 2. Flow Structure and Film Effectiveness." International Journal of Heat and Mass Transfer, 39(11): 2283-2292.

[74] Ligrani, P.M., et al., (1997) "Effects of Bulk Flow Pulsations on Film-Cooled Boundary Layer Structure." Journal of Fluids Engineering-Transactions of the ASME, 1997. 119(1): p. 56-66.

[75] Ligrani, P.M., Cirieloo, S., Bishop, D.T., (1991) "Heat Transfer, Adiabatic Effectiveness and Injectant Distributions Downstream of a Single Row and Two Staggered Rows of Compound Angle Film-Cooling Holes." Heat Transfer in Gas Turbine Engines-Transactions of the ASME, 188: 37-51.

[76] Ligrani, P.M., Subramanian, C.S., Craig, D.W., Kaisuwan, P., (1991) " Effects of Vortices with different Circulations on Heat Transfer and Injectant Downstream of a single Film-Cooling Hole in a Turbulent Boundary Layer." Journal of Turbomachinery-Transactions of the ASME, 113:433-441.

[77] Ligrani, P.M., Subramanian, C.S., Craig, D.W., Kaisuwan, P., (1991) " Effects of Vortices with different Circulations on Heat Transfer and Injectant Downstream of a Row of Film-Cooling Hole in a Turbulent Boundary Layer." Journal of Turbomachinery-Transactions of the ASME, 113:79-90.

[78] Ligrani, P.M., Mitchell, S.W., (1992) "Interactions between embedded Vortices and Injectant from Film Cooling Holes with Compound angle orientations in a turbulent Boundary Layer." Proceedings of the ASME Turbo Expo 1992, 92-GT-199, Cologne, Germany.

[79] Ligrani, P.M., Joseph, S.L., Ortiz, A., Evans, D.L., (1988) "Heat Transfer in Film-Cooled Turbulent Boundary Layers at different Blowing Ratios as affected by Longitudinal Vorticies." Experimental Thermal and Fluid Sciene 1988; 1: 347-362.

[80] Ligrani, P.M., Ortiz, A., Joseph, S.L., Evans, D.L., (1989) "Effects of Embedded Vortices on Film-Cooled Turbulent Boundary Layers." Journal of Turbomachinery-Transactions of the ASME, 111: 71-77.

[81] Makki, Y.H., Jakubowski, G.S., (1986) "An experimental Study of Film Cooling from Diffused Trapezoidal Shaped Holes." Proceedings of the AIAA/ASME 4th Joint Thermophysics and Heat Transfer Conference 1986, AIAA-86-1326, Boston, Massachusetts.

[82] Märklin, B., (2002) "Design, Manufacturing and Commissioning of a Pulsator." Semesterwork SS02, LSM, IET, ETHZ.

[83] Martiny, M., Schulz, A., Wittig, S., Dilzer, M., (1997) "Influence of a mixing -Jet on Film Cooling." Proceedings of the ASME Turbo Expo 1997, 97-GT-

247, Orlando, Florida, USA.

[84] Mehendale, A.B., Han, J.C., Ou, S., Lee, C.P., (1994) "Unsteady Wake over a Linear Turbine Blade Cascade with Air and CO2 Film Injection: Part I: Effect on Film Effectiveness and Heat Transfer Distributions." ASME Journal of Turbomachinery, 116: 730-737.

[85] Melling, A. (1997) "Tracer particles and seeding for particle image velocimetry" Meas. Sci. Technol., Vol. 8:1406-1416.

[86] Melling, A., Durst, F., Whitelaw, J. H. (1981) "Principles and Practise of Laser-Doppler Anemometry." 2nd edition, Academic Press.

[87] Nikuradse, J., (1932) "Gesetzmässigkeit der turbulenten Strömung in glatten Rohren." Forsch. Arb. Ing.-Wes. Heft 356.

[88] Ou, S., Han, J.C., Mehendale, A.B., Lee, C.P., (1994) "Unsteady Wake over a Linear Turbine Blade Cascade with Air and CO2 Film Injection: Part I: Effect on Heat Transfer Coefficients." ASME Journal of Turbomachinery, 116: 721-729.

[89] Pedersen, D.R., Eckert, E.R.G., Goldstein, R.J., (1977) "Film Cooling with Large Density Differences between Mainstream and Secondary Fluid Measured by Heat-Mass Transfer Analogy." Journal of Heat Transfer-Transactions of the ASME, 99(4): 620-627.

[90] Pietrzyk, J. R., Bogard, B. G., Crawford, M. E., (1989) "Experimental Study of the Interaction of Dense Jets with a Crossflow for Gas Turbine Applications." technical report 89-1, Turbulence and Turbine Cooling Research Laboratory, Mechanical Engineering Department, The University of Texas at Austin, Austin Texas.

[91] Popp, O., Smith, D. E., Bubb, J. V., Grabowski, H. C., Diller, T. E., Schetz, J. A., and Ng, W. F. (2000) "An Investigation of Heat Transfer in a Film Cooled Transonic Turbine Cascade, Part I: Steady Heat Transfer." Proceedings of the ASME Turbo Expo 2000, Munich, 8.

[92] Prandtl, L., (1935) "The mechanics of Viscous Fluids." in Durand, W.F. "Aerodynamic Theory III." p. 34-208, Springer, Berlin.

[93] Raffel, M., Willert, C. E., Kompenhans, J. "Particle Image Velocimetry - A Practical Guide." Springer-Verlag.

[94] Reynolds, O., (1876) "On the Resistance Encountered by Vortex Rings, and the Relation between the Vortex Rings and the Streamlines of a Disc." Nature 14, 477.

[95] Rigby, M.J., Johnson, A.B., Oldfield, M.L.G., (1984) "Gas Turbine Rotor Blade Film cooling with and without Simulated NGV Shock Waves and Wakes." ASME paper 90-GT-78.

[96] Rockwell, R. K. (1989). "Transient Heat Transfer Measurements on a Flat Plate in Turbulent Flow using an Electrical Analog." MSc, Air Force Institute of Technology, Wright-Patterson AF Base, Ohio.

[97] Rowbury, D.A., Oldfield, M.L.G., Lock, G.D., (2000) "Large Scale Testing to Validate the Influence of External Crossflow on the Discharge Coefficients

of Film Cooling Holes." Proceedings of the ASME Turbo Expo 2000, 2000-GT-0293, Munich, Germany.

[98] Rowbury, D.A., Oldfield, M.L.G., Lock, G.D., (2000) "A Method for Correlating the Influence of External Crossflow on the Discharge Coefficients of Film-Cooling Holes." Proceedings of the ASME Turbo Expo 2000, 2000-GT-0294, Munich, Germany.

[99] Shandorov, G. S., (1957) "Flow from a Channel into Stationary and Moving Media." Zh. Tekhn. Fiz., 37,1.

[100] Smith, D. E., Bubb, J. V., Popp, O., Grabowski, H. C., Diller, T. E., Schetz, J. A., Ng, W. F., (2000) "An Investigation of Heat Transfer in a Film Cooled Transonic Turbine Cascade, Part II: Unsteady Heat Transfer." Proceedings of the ASME Turbo Expo 2000, Munich, 8.

[101] Sung Jung, I., Ligrani, P.M., Lee, J.S., (2001) "Effects of Bulk Flow Pulsations on Phase-averaged and Time-averaged Film-cooled Boundary Layer Flow Structure." Journal of Fluids Engineering-Transactions of the ASME, 123(3): 559-566.

[102] Takeishi, K., Aoki, S., Sato, T., Tsukagoshi, K., (1992) "Film Cooling on a Gas Turbine Rotor Blade." ASME Journal of Turbomachinery, 114: 828-834.

[103] Teekaram, A. J. H., Forth, C. J. P., and Jones, T. V., (1989) "The Use of Foreign Gas to Simulate the Effects of Density Ratios in Film Cooling." Journal of Turbomachinery-Transactions of the ASME, 111(1):57-62.

[104] Teekaram, A.J.H., Forth, C.J.P., Jones, T.V., (1991) "Film Cooling in the Presence of Mainstream Pressure-Gradients." Journal of Turbomachinery-Transactions of the ASME, 113(3): p. 484-492.

[105] Teng, S., Han, J.C., Poinsatte, P.E., (2001) "Effect of Film Hole Shape on Turbine Blade Heat Transfer Coefficient Distribution." AIAA Journal of Thermophysics and Heat Transfer, 15(3):249-256.

[106] Teng, S., Han, J.C., Poinsatte, P.E., (2001) "Effect of Film Hole Shape on Turbine Blade Film Cooling Performance." AIAA Journal of Thermophysics and Heat Transfer, 15(3):257-265.

[107] VDI-Norm 2040 in DIN Taschenbuch 229, "Durchflussmessungen von Fluiden in geschlossenen Leitungen und Drosselgeräten: Blenden, Düsen, Venturirohre." 2nd edition, Beuth Verlag, Berlin.

[108] Wieghardt, K., (1944) "On the Blowing of Warm Air for De-Icing Devices." F.B. 1900, Reports and Translations No. 315.

[109] Wilfert, G., Fottner, L., (1994) "The Aerodynamic Mixing Effect of Discrete Cooling Jets with Mainstream Flow on a highly loaded Turbine Blade." Proceedings of the ASME Turbo Expo 1994, 94-GT-235, The Hague, Netherlands.

[110] Willert, C.E., Gharib, M., (1991) "Digital Particle Image Velocimetry." Experiments in Fluids, Vol. 10, pp 181-193.

[111] Yuen, C.H.N, Martinez-Bothas, R.F., (2003) "Film Cooling Characteristics of a Single Round Hole at Various Streamwise Angles in a Crossflow: Part I

Effectiveness." International Journal of Heat and Mass Transfer, 46: 221-235.

[112] Yuen, C.H.N, Martinez-Bothas, R.F., (2003) "Film Cooling Characteristics of a Single Round Hole at Various Streamwise Angles in a Crossflow: Part II Heat Transfer Coefficient." International Journal of Heat and Mass Transfer, 46: 237-249.

CURRICULUM VITAE

Stefan Bernsdorf
born the 25.5.1972 in Erlangen, Germany

Education

1978 - 1982	Primary school in Moehrendorf
1982 - 1991	Gymnasium in Erlangen, graduation with the Abitur
1991 - 1994	Undergraduate studies in mechanical engineering at the University of Bremen
1994 - 1997	Graduate studies in mechanical engineering at the Swiss Federal Institute of Technology ETH, graduation as Dipl. Ing. ETH
1998 - 2000	Postgraduate studies in mechanical engineering at the University of Cape Town, graduation as MSc UCT
2000 - 2005	Postgraduate studies in mechanical engineering at the Swiss Federal Institute of Technology ETH

Work Experience

Jul. - Aug. 1991	FAG Kugelfischer AG, Ebern
Feb. - Mär. 1992	Siemens AG, Erlangen
Oct. 1995 - Mar. 1996	ABB Turbo Systems AG, Baden
Oct. - Dez. 1997	R&D engineering, ABB Turbo Systems AG, Baden
Feb. - Dez. 1999	Consulting work for Foskor SA Ltd.
Jan. 1999 - Apr. 2000	Teaching Assistant at the ASPECT program of UCT
since Apr. 2000	Turbomachinery Laboratory LSM, ETH Zürich